Imaging cerebral small vessel disease at 7 Tesla MRI

Mandy M. A. Conijn

Imaging cerebral small vessel disease at 7 Tesla MRI

Beeldvorming van microvasculaire schade in de hersenen met 7 Tesla MRI

(met een samenvatting in het Nederlands)

Proefschrift

ter verkrijging van de graad van doctor aan de Universiteit Utrecht
op gezag van rector magnificus, prof.dr. G.J. van der Zwaan,
ingevolge het besluit van het college voor promoties
in het openbaar te verdedigen op
donderdag 28 april 2011 des middags te 12.45 uur

door

Mandy Martine Ariane Conijn

geboren op 16 juni 1983 te Lisse

Imaging cerebral small vessel disease at 7 Tesla MRI

Thesis | Utrecht University

ISBN 978-94-6108-154-4

Lay-out and cover design | André Koppen
Print | Gildeprint Drukkerijen B.V. • Enschede • the Netherlands

Promotoren	Prof. dr. P.R. Luijten
	Prof. dr. W.P.Th.M. Mali
Co-promotoren	Dr. M.I. Geerlings
	Dr. J. Hendrikse

Voor mijn ouders

The financial support by the Netherlands Heart Foundation and the Röntgen Stichting Utrecht for the publication of this thesis is gratefully acknowledged.

Financial support for the publication of this thesis was also generously provided by Philips Healthcare and Alzheimer Nederland (Bunnik).

Manuscripts based on the studies presented in this thesis

Chapter 2 Cerebral small vessel disease and the risk of death, ischemic stroke and cardiac complications in patients with atherosclerotic disease - The SMART-MR study
Mandy M.A. Conijn, Raoul P. Kloppenborg, Willem P.Th.M. Mali, L. Jaap Kappelle, Koen L. Vincken, Yolanda van der Graaf, Mirjam I. Geerlings; for the SMART Study Group, submitted

Chapter 3 Perforating arteries originating from the posterior communicating artery: a 7.0 Tesla MRI study
Mandy M.A. Conijn, Jeroen Hendrikse, Jaco J.M. Zwanenburg, Taro Takahara, Mirjam I. Geerlings, Willem P.Th.M. Mali, Peter R. Luijten. Eur Radiol 2009;19:2986-2992.

Chapter 4 Visualization of cerebral microbleeds with dual echo T2*-weighted MR imaging at 7.0 Tesla
Mandy M.A. Conijn, Mirjam I. Geerlings, Peter R. Luijten, Jaco J.M. Zwanenburg, Fredy Visser, Geert-Jan Biessels, Jeroen Hendrikse. J Magn Reson Imaging 2010;32:52-59

Chapter 5 Cerebral microbleeds on MRI: comparison between 1.5 and 7 Tesla
Mandy M.A. Conijn, Mirjam I. Geerlings, Geert-Jan Biessels, Taro Takahara, Theo D. Witkamp, Jaco J.M. Zwanenburg, Peter R. Luijten, Jeroen Hendrikse, in press AJNR

Chapter 6 Iron deposition in basal ganglia at 7T: determinants and relation with cerebral small vessel disease
Mandy M.A. Conijn, Jeroen Hendrikse, Daniël Polders, Hendrik de Leeuw, Raoul P. Kloppenborg, Willem P.Th.M. Mali, Peter R. Luijten, Mirjam I. Geerlings, submitted

Chapter 7 Microbleeds, lacunar infarcts, white matter lesions and cerebrovascular reactivity - a 7T study
Mandy M.A. Conijn, Johannes M. Hoogduin, Yolanda van der Graaf, Jeroen Hendrikse, Peter R. Luijten, Mirjam I.Geerlings, submitted

Contents

CHAPTER 01

Introduction

Chapter 01 Introduction

Introduction

Cerebral small vessel disease

Cerebral small vessel disease is a term often used to refer to lacunar infarcts and white matter lesions; ischemic lesions that are thought to be caused by changes in the small vessels of the brain. Lacunar infarcts and white matter lesions are commonly found on magnetic resonance imaging (MRI) scans. Almost a quarter of the people of 65 years and older have lacunar infarcts, of which almost 90% are asymptomatic.[1] White matter lesions are even more common, more than 90% of the people above the age of 60 has some degree of white matter lesions, with the severity of the lesions increasing with age.[2] Although the term cerebral small vessel disease is currently directly related with the occurrence of ischemic lesions, patients with cerebral small vessel disease also have an increased risk of hemorrhage.[3] Recently, microhemorrhages or microbleeds are increasingly recognized as another manifestation of cerebral small vessel disease.[4,5] Microbleeds are also commonly observed on MRI. Although prevalence estimates differ between studies, prevalences up to 24% are found in the general elderly population.[6] Lacunar infarcts, white matter lesions and microbleeds may be small and often asymptomatic, but their clinical relevance should not be underestimated.[7] Previous studies have shown that lacunar infarcts and white matter lesions predict the risk of stroke, dementia and mortality.[8-10] In addition, microbleeds are associated with cognitive impairment, functional dependence and death.[4,11,12] Although still under debate, the presence of microbleeds could be of importance in patients with ischemic stroke receiving anticoagulation, as it might indicate a higher risk of future intracerebral haemorrhage.[13-15]

The pathophysiology of cerebral small vessel disease is largely unknown. Cerebral small vessel disease is hypothesized to be caused by changes in the small, perforating arteries in the brain.[18-20] These perforating arteries can only be assessed post-mortem or in vivo with conventional clinical imaging techniques via intra-arterial digital subtraction angiography or rotational angiography.[21-23] In the 1950s pathology studies showed changes in the arterial vessel wall of the perforating arteries in patients with lacunar infarcts. These specific changes have been called lipohyalinosis and are sometimes referred to as arteriolosclerosis.[18,19] One of the problems of studying the underlying pathology of cerebral small vessel disease in post-mortem studies is that only very few patients die from these lesions. This makes autopsy material relatively scant and difficult to interpret, as death may occur long after occurrence of the lesions.[16] Recently, evidence has increased that endothelial dysfunction plays a role in the pathophysiology of cerebral small vessel disease.[24-26] The problems with in vivo visualization of the perforating arteries, however, are the invasiveness and radiation dose of angiography. Therefore, conventional angiography cannot be used in studies with a relatively large number of patients.

MRI is a promising technique to study cerebral small vessel disease in larger studies, because it is not invasive and does not use radiation. However, current imaging techniques using 1.5 and 3T MRI platforms are not sensitive enough to visualize the small vessels in the brain. As a result, lacunar infarcts, white matter lesions and microbleeds are adopted as marker of cerebral small vessel disease, and cerebral small vessel disease has become a synonym of brain parenchyma lesions.[3] On MRI, lacunar infarcts are defined as hypointense foci on T1-weighted sequences with a maximum diameter of 15 or 20 mm. Lacunar infarcts are typically located in the deep white matter, basal ganglia, internal capsule, thalamus, and pons.[3,16] White matter lesions are bilaterally and symmetrically located, patchy or diffuse areas of hyperintensities on T2-weighted and fluid-attenuated inversion recovery images on MR imaging.[3,17] Microbleeds appear as black or hypointense lesions surrounded by brain parenchyma on MRI sequences that are particularly sensitive to susceptibility effects, such as T2*-weighted gradient-recalled echo MRI or susceptibility weighted imaging.[4] Because lacunar infarcts, white matter lesions and microbleeds are all manifestations of ischemic or hemorrhagic damage of the brain tissue, imaging techniques need to be improved to identify biomarkers of cerebral small vessel disease at an earlier stage of the disease. Earlier detection can be important to improve the knowledge about cerebral small vessel disease and to study possible treatment options.

7 Tesla MRI

Recently, clinical MRI systems with a field strength of 7 Tesla have become available for clinical research in a small number of academic institutions. The use of this ultra-high field strength has several advantages that may help identifying earlier stages of cerebral small vessel disease and more direct biomarkers of the underlying pathophysiology of lacunar infarcts, white matter lesions and microbleeds. First, the contrast in MRI is based on tissue-characteristics referred to as relaxation-times. The T1 relaxation-times increase with increasing field strength,[27] generating new possibilities for contrast at 7T. Longer T1 relaxation times at 7T improve background suppression in MR angiography, resulting in increased contrast between the arteries and the background.[12] Furthermore, with increasing field strength the signal-to-noise ratio increases.[28] This increase in signal-to-noise ratio can be used to scan at a high spatial resolution. This results in a high resolution scan with good contrast between arteries and background tissue. Time-of-flight MR angiography at 7T shows clear delineation of the perforating (or lenticulostriate) branches from the anterior and medial cerebral artery.[29,30] These perforating arteries can be a more direct biomarker for cerebral small vessel disease.

A second advantage of ultra-high field MRI is that the susceptibility effect increases with increasing field strength. The magnetic susceptibility is the extent to which a substance becomes magnetized when placed within a magnetic field. Specific MRI-sequences, such as T2*-weighted sequences, are very sensitive to this susceptibility effect and therefore to structures with a high susceptibility. As the effect scales with the magnetic field, the detection of substances with a high susceptibility, such as haemosiderin, ferritin and deoxyhemoglobin, is substantially improved at ultra-high field strengths. As microbleeds are haemosiderin deposits, which have a high magnetic susceptibility, imaging at 7T can be beneficial for the visualization of microbleeds.[31]

Besides the visualization of microbleeds, the increased susceptibility effect also improves the detection of ferritin deposition in the brain. Lacunar infarcts, white matter lesions and microbleeds are associated with endothelial dysfunction and increased permeability of blood-brain barrier,[24-26] and increased permeability of the blood-brain barrier is also associated with iron deposition in the brain. Therefore the increased blood-brain barrier permeability in cerebral small vessel disease could also result in increased iron deposition in the basal ganglia as a secondary consequence.[32] This makes iron deposition in the basal ganglia an interesting possibility for a new imaging biomarker of cerebral small vessel disease. The dramatic increase in susceptibility contrast, sensitivity and resolution at 7T[33] could be very useful to detect subtle changes in iron concentration.

Deoxyhemoglobin is paramagnetic and will contribute to magnetic susceptibility contrast as well. Since blood oxygenation level-dependent functional MRI (BOLD-fMRI) is based on the magnetic effect of deoxyhemoglobin, it benefits from the increased susceptibility effect at 7T.[34] BOLD-fMRI can be used as a measure for reactivity of the brain vasculature.[35] As lacunar infarcts, white matter lesions and microbleeds are thought to result from changes in the small vessels of the brain, these changes may lead to changes in cerebrovascular reactivity. Cerebrovascular reactivity could therefore also be a potentially interesting imaging biomarker for cerebral small vessel disease.

Aim and outline of this thesis

The overall aim of this thesis is to explore imaging biomarkers of early stages of cerebral small vessel disease with 7 Tesla MRI.

First, in *chapter 2* we investigate the clinical relevance of cerebral small vessel disease in patients with atherosclerotic disease. We assess whether the presence of lacunar infarcts and white matter lesions increases the risk of vascular and non-vascular death and future vascular events. *Chapter 3* focuses on the ability of MR angiography at 7T to show perforating branches from the posterior communicating artery and to investigate the presence of visible perforating branches in relation to the size of the feeding posterior communicating artery. In *chapter 4* we describe the use of dual echo T2*-weighted imaging at 7T for the visualization of microbleeds, with the advantages of two echo times. Whether this dual echo T2*-weighted technique at 7T also improves the detection of microbleeds compared to the commonly used single echo T2*-weighted technique at 1.5T, is investigated in *chapter 5*. In *chapter 6* we focus on determinants of iron deposition in the basal ganglia, with use of T2* measurements, and compare iron deposition between patients with lacunar infarcts, white matter lesions or microbleeds and patients without these lesions. In *chapter 7* the relation between cerebrovascular reactivity and the presence of lacunar infarcts, white matter lesions and microbleeds is studied. The findings of the different studies described in this thesis are discussed in *chapter 8* and summarized in *chapter 9*.

Study population

The research described in this thesis is performed within the Second Manifestations of ARTerial disease (SMART) study.[36] In the SMART study patients with symptomatic vascular disease or vascular risk factors are screened for additional risk factors and severity of vascular disease. Since cerebral small vessel disease is common in patients with vascular disease,[37] the SMART cohort can be a useful population to explore imaging biomarkers of early stages of cerebral small vessel disease.

References

1 Longstreth WT, Jr., Bernick C, Manolio TA, Bryan N, Jungreis CA, Price TR. Lacunar infarcts defined by magnetic resonance imaging of 3660 elderly people: the Cardiovascular Health Study. *Arch Neurol* 1998;55:1217-1225.

2 De Leeuw FE, De Groot JC, Achten E, Oudkerk M, Ramos LM, Heijboer R, Hofman A, Jolles J, van Gijn J, Breteler MM. Prevalence of cerebral white matter lesions in elderly people: a population based magnetic resonance imaging study. The Rotterdam Scan Study. *J Neurol Neurosurg Psychiatry* 2001;70:9-14.

3 Pantoni L. Cerebral small vessel disease: from pathogenesis and clinical characteristics to therapeutic challenges. *Lancet Neurol* 2010;9:689-701.

4 Greenberg SM, Vernooij MW, Cordonnier C, Viswanathan A, Al-Shahi SR, Warach S, Launer LJ, Van Buchem MA, Breteler MM. Cerebral microbleeds: a guide to detection and interpretation. *Lancet Neurol* 2009;8:165-174.

5 Wardlaw JM, Lewis SC, Keir SL, Dennis MS, Shenkin S. Cerebral microbleeds are associated with lacunar stroke defined clinically and radiologically, independently of white matter lesions. *Stroke* 2006;37:2633-2636.

6 Vernooij MW, van der Lugt A, Ikram MA, Wielopolski PA, Niessen WJ, Hofman A, Krestin GP, Breteler MM. Prevalence and risk factors of cerebral microbleeds: the Rotterdam Scan Study. *Neurology* 2008;70:1208-1214.

7 Greenberg SM. Small vessels, big problems. *N Engl J Med* 2006;354:1451-1453.

8 de Jong G, Kessels F, Lodder J. Two types of lacunar infarcts: further arguments from a study on prognosis. *Stroke* 2002;33:2072-1076.

9 Debette S, Markus HS. The clinical importance of white matter hyperintensities on brain magnetic resonance imaging: systematic review and meta-analysis. *BMJ* 2010;341:c3666.

10 Vermeer SE, Longstreth WT, Jr., Koudstaal PJ. Silent brain infarcts: a systematic review. *Lancet Neurol* 2007;6:611-619.

11 Henneman WJ, Sluimer JD, Cordonnier C, Baak MM, Scheltens P, Barkhof F, van der Flier WM. MRI biomarkers of vascular damage and atrophy predicting mortality in a memory clinic population. *Stroke* 2009;40:492-498.

12 Werring DJ, Frazer DW, Coward LJ, Losseff NA, Watt H, Cipolotti L, Brown MM, Jager HR. Cognitive dysfunction in patients with cerebral microbleeds on T2*-weighted gradient-echo MRI. *Brain* 2004;127:2265-2275.

13 Fiehler J, Albers GW, Boulanger JM, Derex L, Gass A, Hjort N, Kim JS, Liebeskind DS, Neumann-Haefelin T, Pedraza S, Rother J, Rothwell P, Rovira A, Schellinger PD, Trenkler J. Bleeding risk analysis in stroke imaging before thromboLysis (BRASIL): pooled analysis of T2*-weighted magnetic resonance imaging data from 570 patients. *Stroke* 2007;38:2738-2744.

14 Gregoire SM, Jager HR, Yousry TA, Kallis C, Brown MM, Werring DJ. Brain microbleeds as a potential risk factor for antiplatelet-related intracerebral haemorrhage: hospital-based, case-control study. *J Neurol Neurosurg Psychiatry* 2010;81:679-684.

15 Thijs V, Lemmens R, Schoofs C, Gorner A, Van Damme P, Schrooten M, Demaerel P. Microbleeds and the Risk of Recurrent Stroke. *Stroke* 2010.

16 Wardlaw JM. What causes lacunar stroke? *J Neurol Neurosurg Psychiatry* 2005;76:617-619.

17 Inzitari D. Leukoaraiosis: an independent risk factor for stroke? *Stroke* 2003;34:2067-2071.

18 Fisher CM. The arterial lesions underlying lacunes. *Acta Neuropathol* 1968;12:1-15.

19 Fisher CM. Lacunes: small, deep cerebral infarcts. 1965. *Neurology* 1998;50:841.

20 Lammie GA, Brannan F, Slattery J, Warlow C. Nonhypertensive cerebral small-vessel disease. An autopsy study. *Stroke* 1997;28:2222-2229.

21 Anxionnat R, Bracard S, Ducrocq X, Trousset Y, Launay L, Kerrien E, Braun M, Vaillant R, Scomazzoni F, Lebedinsky A, Picard L. Intracranial aneurysms: clinical value of 3D digital subtraction angiography in the therapeutic decision and endovascular treatment. *Radiology* 2001;218:799-808.

22 Kang HS, Han MH, Kwon BJ, Kwon OK, Kim SH, Chang KH. Evaluation of the lenticulostriate arteries with rotational angiography and 3D reconstruction. *AJNR Am J Neuroradiol* 2005;26:306-312.

23 Shimizu S, Suzuki H, Maki H, Maeda M, Miya F, Benali K, Trousset Y, Taki W. A novel image fusion visualizes the angioarchitecture of the perforating arteries in the brain. *AJNR Am J Neuroradiol* 2003;24:2011-2014.

24 Hassan A, Hunt BJ, O'Sullivan M, Parmar K, Bamford JM, Briley D, Brown MM, Thomas DJ, Markus HS. Markers of endothelial dysfunction in lacunar infarction and ischaemic leukoaraiosis. *Brain* 2003;126:424-432.

25 Wardlaw JM, Sandercock PA, Dennis MS, Starr J. Is breakdown of the blood-brain barrier responsible for lacunar stroke, leukoaraiosis, and dementia? *Stroke* 2003;34:806-812.

26 Wardlaw JM, Doubal F, Armitage P, Chappell F, Carpenter T, Munoz MS, Farrall A, Sudlow C, Dennis M, Dhillon B. Lacunar stroke is associated with diffuse blood-brain barrier dysfunction. *Ann Neurol* 2009;65:194-202.

27 Rooney WD, Johnson G, Li X, Cohen ER, Kim SG, Ugurbil K, Springer CS, Jr. Magnetic field and tissue dependencies of human brain longitudinal 1H2O relaxation in vivo. *Magn Reson Med* 2007;57:308-318.

28 Vaughan JT, Garwood M, Collins CM, Liu W, DelaBarre L, Adriany G, Andersen P, Merkle H, Goebel R, Smith MB, Ugurbil K. 7T vs. 4T: RF power, homogeneity, and signal-to-noise comparison in head images. *Magn Reson Med* 2001;46:24-30.

29 Hendrikse J, Zwanenburg JJ, Visser F, Takahara T, Luijten P. Noninvasive depiction of the lenticulostriate arteries with time-of-flight MR angiography at 7.0 T. *Cerebrovasc Dis* 2008;26:624-629.

30 Kang CK, Park CW, Han JY, Kim SH, Park CA, Kim KN, Hong SM, Kim YB, Lee KH, Cho ZH. Imaging and analysis of lenticulostriate arteries using 7.0-Tesla magnetic resonance angiography. *Magn Reson Med* 2009;61:136-144.

31 Biessels GJ, Zwanenburg JJ, Visser F, Frijns CJ, Luijten PR. Hypertensive cerebral hemorrhage: imaging the leak with 7-T MRI. *Neurology* 2010;75:572-573.

32 Ke Y, Qian ZM. Brain iron metabolism: neurobiology and neurochemistry. *Prog Neurobiol* 2007;83:149-173.

33 Yao B, Li TQ, Gelderen P, Shmueli K, de Zwart JA, Duyn JH. Susceptibility contrast in high field MRI of human brain as a function of tissue iron content. *Neuroimage* 2009;44:1259-1266.

34 Yacoub E, Shmuel A, Pfeuffer J, Van De Moortele PF, Adriany G, Andersen P, Vaughan JT, Merkle H, Ugurbil K, Hu X. Imaging brain function in humans at 7 Tesla. *Magn Reson Med* 2001;45:588-594.

35 Rostrup E, Law I, Blinkenberg M, Larsson HB, Born AP, Holm S, Paulson OB. Regional differences in the CBF and BOLD responses to hypercapnia: a combined PET and fMRI study. *Neuroimage* 2000;11:87-97.

36 Simons PC, Algra A, van de Laak MF, Grobbee DE, van der Graaf Y. Second manifestations of ARTerial disease (SMART) study: rationale and design. *Eur J Epidemiol* 1999;15:773-781.

37 Geerlings MI, Appelman AP, Vincken KL, Algra A, Witkamp TD, Mali WP, van der Graaf Y. Brain volumes and cerebrovascular lesions on MRI in patients with atherosclerotic disease. The SMART-MR study. Atherosclerosis 2009.

CHAPTER 02

Cerebral small vessel disease and the risk of death, ischemic stroke and cardiac complications in patients with atherosclerotic disease. The SMART-MR study

Mandy M.A. Conijn
Raoul P. Kloppenborg
Willem P.Th.M. Mali
L. Jaap Kappelle
Koen L. Vincken
Yolanda van der Graaf
Mirjam I. Geerlings

Abstract

Background and Purpose

Cerebral small vessel disease may be related to both vascular and non-vascular pathology. We assessed whether lacunar infarcts and white matter lesions (WML) on MRI increased the risk of vascular and non-vascular death and future vascular events in patients with atherosclerotic disease.

Methods

Brain MRI was performed in 1309 patients with atherosclerotic disease from the Second Manifestations of ARTerial disease-Magnetic Resonance (SMART-MR) study. Infarcts were scored visually and volumetric assessment of WML was performed. Patients were followed for a median duration of 4.5 years (range 0.2-7.1 years) for death, ischemic stroke and ischemic cardiac complications.

Results

Cox regression models showed that presence of lacunar infarcts (n=223) was associated with increased risk of vascular death (HR 2.6, 95% CI 1.4-4.9) and non-vascular death (HR 2.7, 95% CI 1.3-5.3), after adjusting for age, sex, vascular risk factors, non-lacunar infarcts and WML. These risks were similar for patients with silent lacunar infarcts. WML-volume (relative to total intracranial volume) increased the risk of vascular death (HR per ml increase 1.03, 95% CI 1.01-1.05) and patients in the upper quintile of WML showed an increased risk of ischemic stroke as compared to patients in the four lower quintiles (HR 2.6, 95% CI 1.3-4.9).

Conclusion

This study shows that cerebral small vessel disease, with or without a history of stroke, is associated with an increased risk of death and ischemic stroke in patients with atherosclerotic disease.

Chapter 02 Cerebral small vessel disease and the risk of death, ischemic stroke and cardiac complications in patients with atherosclerotic disease. The SMART-MR study

Introduction

In cerebral small vessel disease, ischemic lesions are located in the supplying areas of the small perforating arteries in the basal ganglia or in the deep white matter of the brain. Both macrovascular disease, such as atherosclerosis and hypertension, and microvascular disease, such as endothelial dysfunction and leakage of the blood brain barrier, have been associated with cerebral small vessel disease.[1-4] On MRI, markers of cerebral small vessel disease are visible as white matter lesions (WML) and lacunar infarcts. They increase the risk of stroke, cognitive decline, dementia and death, both in the general population and in stroke patients.[5-8] Patients with atherosclerosis have a high risk of vascular events. It is not known whether the presence of lacunar infarcts or WML imposes an additional risk of death or vascular events on top of preexistent vascular disease. The clinical relevance of lacunar infarcts and WML in patients with atherosclerosis is important, as atherosclerosis is still an increasing problem in the world[9] and WML and silent infarcts are common in patients with atherosclerosis.[10] The only study that investigated WML in patients with established atherosclerotic disease showed that WML increased the risk of ischemic stroke and myocardial infarction.[11] There are no studies concerning adverse outcomes in patients with atherosclerotic disease in relation to lacunar infarcts.

In population-based studies cerebral small vessel disease has also been associated with retinopathy and nephropathy.[12,13] It is assumed that underlying generalized small vessel disease is responsible for this association, which is supported by the observation that similar pathological changes (e.g. hyaline arteriolosclerosis) are found in kidneys of patients with hypertensive nephropathy and in brains of patients with cerebral small vessel disease.[14,15] Nephropathy itself is associated with increased all cause mortality,[16] and as WML are associated with non-vascular pathology such as pneumonia,[17] it can be hypothesized that patients with lacunar infarcts or WML are at risk for both vascular and non-vascular events.

We investigated whether WML and lacunar infarcts were associated with increased risk of death, including vascular and non-vascular death, and risk of future vascular events in a large cohort of patients with symptomatic atherosclerotic disease.

Methods

SMART-MR Study

Data were used from the Second Manifestations of ARTerial disease-Magnetic Resonance (SMART-MR) study, a prospective cohort study aimed to investigate brain changes on MRI in 1309 patients with symptomatic atherosclerotic disease. Details of the design and patients have been described elsewhere.[10] In brief, between May 2001 and December 2005, all patients newly referred to the University Medical Center Utrecht with manifest coronary artery disease, cerebrovascular disease, peripheral arterial disease or an abdominal aortic aneurysm, and without MR contraindications were invited to participate. During a 1-day visit to our medical center, a MRI of the brain was performed, in addition to a physical examination, ultrasonography of the carotid arteries, and blood and urine sampling. Risk factors, medical history, and functioning were assessed with questionnaires that the patients completed before their visit to the medical center. The SMART-MR study was approved by the ethics committee of our institution and written informed consent was obtained from all patients.

Magnetic Resonance Imaging Protocol

The MR investigations were performed on an 1.5-Tesla whole-body system (Gyroscan ACS-NT, Philips Medical Systems, Best, the Netherlands). The protocol consisted of transversal T1-weighted (TR/TE: 235/2 ms), T2-weighted (TR/TE: 2200/11 ms and 2200/100 ms), fluid-attenuating inversion recovery (FLAIR) (TR/TE/inversion time (TI): 6000/100/2000 ms) and inversion recovery (IR) (TR/TE/TI: 2900/22/410 ms) sequences. Field of view was 230x230 mm, matrix size 180x256, slice thickness 4.0 mm, no gap, 38 slices.

Brain segmentation and white matter lesions

We used the T1-weighted, IR and FLAIR sequence for the probabilistic segmentation technique that has been described elsewhere.[18,19] The segmentation program distinguishes cortical gray matter, white matter, cerebrospinal fluid (CSF), and lesions. The results of the segmentation analysis were visually checked for the presence of infarcts and adapted if necessary to make a distinction between WML and infarct volumes. Total brain volume was calculated by summing the volumes of gray and white matter and, if present, the volumes of WML and infarcts. All volumes cranial to the foramen magnum were included. As a result, the total brain volume includes the cerebrum, brainstem and cerebellum. Total intracranial volume (ICV) was calculated by summing the total brain volume and the volume of the CSF. Volumes of WML were normalized for ICV by dividing WML volume by ICV and multiplying this value by the mean ICV of the study population.

In 188 patients the IR and T1-weighted sequence were missing due to a temporary change in MRI protocol, and the brain segmentation was based on the FLAIR sequence. Intraclass correlation coefficients between the segmentation using all 3 sequences and FLAIR only based on a subset of 740 patients were 0.995, 0.996, 0.961, 0.996, 0.996, and 0.985 for ICV, total brain volume, CSF, ventricular volume, gray and white matter volume, and white matter lesion volume, respectively.

Infarcts

The whole brain was visually searched for infarcts by a trained investigator and a neuroradiologist. Raters were blinded for the history and diagnosis of the patient. Discrepancies in rating were re-evaluated in a consensus meeting. Infarcts were defined as focal hyperintensities on T2-weighted images of at least 3 mm in diameter. Hyperintensities located in the white matter had to be hypointense on T1-weighted and FLAIR images in order to distinguish them from WML. Dilated perivascular spaces were distinguished from infarcts on the basis of their location, form, and the absence of gliosis. Brain infarcts were categorized as lacunar and non-lacunar (cortical infarcts, large subcortical infarcts, infratentorial infarcts). We defined lacunar infarcts as infarcts sized 3 to 15 mm in diameter in plane and located in the subcortical white matter, thalamus or basal ganglia.

Vascular risk factors

During the patient's visit to the medical center, an overnight fasting venous blood sample was taken to determine glucose and lipid levels. Height and weight were measured and the body mass index (BMI) was calculated (kg/m^2). Blood pressure was measured twice with a sphygmomanometer and the average of the two measures was calculated. Hypertension was defined as mean systolic blood pressure ≥160 mm Hg or mean diastolic blood pressure ≥95 mm Hg or self reported use of antihypertensive drugs. Diabetes mellitus was defined as a history of diabetes mellitus, glucose ≥7.0 mmol/L or self reported use of oral antidiabetic drugs or insulin. Hyperlipidemia was defined as total cholesterol >5.0 mmol/L, low-density lipoprotein cholesterol >3.2 mmol/L or self reported use of lipid lowering drugs. Smoking habits and alcohol intake were assessed with questionnaires. Packyears of smoking were calculated. Alcohol intake was categorized as never, former, or current. Patients who had quit drinking during the past year were assigned to the category current alcohol intake.

Study sample

In total, 1309 patients participated in the SMART-MR study. Of these, MR data were irretrievable for 19 patients and 14 had no FLAIR sequence; these were excluded from the study sample. In 44 patients brain volume data were missing due to motion or artefacts. Of the remaining 1232 patients, follow-up data were missing in four patients. Consequently, the analyses were performed in 1228 patients.

Follow-up

The occurrence of new vascular events was continuously monitored by sending the patients a questionnaire every 6 months to provide information on hospitalization and outpatient clinic visits. If a cardiovascular event was reported, original source documents were retrieved and reviewed to determine the occurrence of cardiovascular disease. All possible events were audited independently by three physicians of the Endpoint Committee. Patients were followed until death or refusal of further participation. The main outcomes of interest for this study were death, ischemic stroke and ischemic cardiac complications. Definitions of outcomes are given in table 1.

Table 1 Definition of Outcomes

All cause death	Death of a vascular or non-vascular cause
Death of a vascular cause	Death caused by myocardial infarction, stroke, sudden death (unexpected cardiac death occurring within 1 hour after onset of symptoms, or within 24 hours given convincing circumstantial evidence), congestive heart failure, rupture of abdominal aortic aneurysm or death from another vascular cause.
Death of a non-vascular cause	Death caused by infection, cancer, unnatural death, or death from another non-vascular cause.
Ischemic stroke	Relevant clinical features that caused an increase in impairment of at least one grade on the modified Rankin scale, with or without a new relevant ischemic lesion at brain imaging.
Ischemic cardiac complications	Myocardial infarction, sudden death or fatal congestive heart failure.

Statistical Analysis

The time between date of MRI-scan until death, loss to follow-up or end of follow-up in March 2009, whichever came first, was calculated to establish the follow-up time. To determine the relation between the presence of lacunar infarcts and the occurrence of death, ischemic stroke or ischemic cardiac complications Cox proportional hazards regression analysis was done with resulting hazard ratios and corresponding 95% confidence intervals.

In the first model adjustments were made for age and sex, in the second model we additionally adjusted for hypertension, diabetes mellitus, BMI, smoking, alcohol consumption and hyperlipidemia. In the third model we additionally adjusted for presence of non-lacunar infarcts on MRI or a clinical history of stroke. Clinical history of stroke was defined as self-reported stroke or carotid-operation in the clinical history or inclusion in the study with stroke or TIA as diagnosis. We repeated the analyses for the presence of silent lacunar infarcts, defined as patients with lacunar infarcts on the MRI scan but without a clinical history of stroke, compared with patients without a clinical history of stroke and no silent lacunar infarcts. In this case model three was not adjusted for clinical history of stroke.

The same models were used to analyse the relation between the volume of WML and the occurrence of death, ischemic stroke or cardiac complications. The volume of WML was analysed as a continuous variable per mL relative to ICV. To investigate the risk in patients with the largest volume of WML, the analysis was also done for severe WML (upper quintile) compared to the four lower quintiles combined. The same adjustments were made as in the models for lacunar infarcts, except for model 3 where we adjusted for all infarcts or clinical history of stroke.

As final step, all the above described analyses were additionally adjusted for the diagnosis of atherosclerotic disease at inclusion, and stratified analysis according to atherosclerotic diagnosis at inclusion were done. SPSS version 15.0 (Chicago, IL, USA) was used to analyse the data.

Results

Baseline characteristics of the 1228 patients are shown in table 2. There were 101 patients with lacunar infarcts who had no clinical history of stroke, and 845 patients without lacunar infarcts and no clinical history of stroke. Patients in the upper quintile of WML had a median WML-volume of 7.7 mL (10^{th}-90^{th} percentile: 4.6-22.5 mL). In total, 106 patients died during a median follow-up of 5.3 years (range 0.2-8.1 years).

Table 2 **Baseline Characteristics of the Patients in SMART-MR study**

	All patients (n=1228)
Male sex (%)	79.6
Age (years)	58.6 ± 10.1
Hypertension (%)	51.5
Diabetes mellitus (%)	20.1
Packyears of smoking	28.9 (0-50.4)
Body mass index (kg/m^2)	26.8 ± 3.8
Alcohol consumption	
- Never (%)	15.9
- Former (%)	9.1
- Current/recently quit (%)	75.0
Hyperlipidemia (%)	77.7
Clinical history of stroke (%)	23.0
One or more lacunar infarcts (%)	18.2
White matter lesion volume relative to total intracranial volume (mL)	1.58 (0.49-7.73)

Age and BMI are expressed as means with standard deviations. Packyears of smoking and white matter lesions volume are expressed as median with 10^{th} and 90^{th} percentile.

All cause death

The presence of one or more lacunar infarcts increased the risk of all cause death after adjusting for age and sex (HR 3.0, 95% CI 2.0-4.4, p<0.001). This association remained after additional adjustment for vascular risk factors and presence of non-lacunar infarcts, WML and history of stroke (table 3). In patients without clinical history of stroke (n=946), silent lacunar infarcts also increased the risk of all cause death after adjusting for age and sex (HR 3.6, 95% CI 2.2-6.0, p<0.001), and also after additional adjustment for vascular risk factors, non-lacunar infarcts and WML (HR 3.2, 95% CI 1.8-5.5, p<0.001).

The HR of all cause death per mL increase in WML volume was 1.02 (95% CI 1.01-1.04, p<0.001) after adjustment for age, sex, vascular risk factors, and infarcts on MRI or history of stroke. Compared with patients with less WML, patients in the upper quintile of WML (> 4.2 ml) also had an increased risk of all cause death (HR 1.7, 95% CI 1.1-2.7, p=0.001) (table 3).

Table 3 **Relationship between the Presence of Lacunar Infarcts and White Matter Lesions and *Death***

	No. of deaths	No. per 1000 person years	Hazard Ratio (95% CI) Model 1	Model 2	Model 3
All cause death					
Lacunar infarcts					
Absent (n=1005)	56	10.4	1 [reference]	1 [reference]	1 [reference]
Present (n=223)	50	42.4	3.0 (2.0-4.4)**	2.6 (1.7-3.9)**	2.5 (1.6-4.0)**
White matter lesions					
Per ml (n=1228)	106	16.1	1.03 (1.02-1.05)**	1.03 (1.01-1.05)**	1.02 (1.01-1.04)**
Upper quintile (n=246)	48	38.3	2.1 (1.4-3.2)**	2.0 (1.3-3.0)**	1.7 (1.1-2.7)*
Vascular death					
Lacunar infarcts					
Absent (n=1005)	27	5.0	1 [reference]	1 [reference]	1 [reference]
Present (n=223)	30	25.5	3.6 (2.1-6.2)**	3.2 (1.8-5.6)**	2.6 (1.4-4.9)**
White matter lesions					
Per ml (n=1228)	57	8.7	1.04 (1.02-1.06)**	1.04 (1.02-1.06)**	1.03 (1.01-1.05)**
Upper quintile (n=246)	30	23.9	2.9 (1.6-5.1)**	2.8 (1.6-5.0)**	2.4 (1.3-4.2)**
Non-vascular death					
Lacunar infarcts					
Absent (n=1005)	28	5.2	1 [reference]	1 [reference]	1 [reference]
Present (n=223)	20	17.0	2.5 (1.4-4.4)**	2.3 (1.2-4.2)**	2.7 (1.3-5.3)**
White matter lesions					
Per ml (n=1228)	48	7.3	1.02 (0.99-1.05)	1.02 (0.99-1.05)	1.02 (0.98-1.05)
Upper quintile (n=246)	17	13.6	1.4 (0.7-2.6)	1.2 (0.6-2.4)	1.1 (0.6-2.2)

Model 1: *adjusted for age and sex*
Model 2: *additionally adjusted for hypertension, diabetes mellitus, body mass index, smoking (packyears), alcohol consumption and hyperlipidemia*
Model 3: *Lacunar infarcts: additionally adjusted for non-lacunar infarcts on MRI or clinical history of stroke, and white matter lesions*
White matter lesions: additionally adjusted for all other infarcts on MRI or clinical history of stroke
* $p < 0.05$
** $p < 0.01$

Vascular death

In 57 patients (53.8%) the cause of death was vascular. The cause of death was in 18 patients sudden death, in 10 patients stroke, in 7 patients congestive heart failure, in 4 patients myocardial infarction, in 4 patients rupture of a abdominal aortic aneurysm and in 14 patients other vascular causes. The HR of vascular death was 3.6 (95% CI 2.1-6.2, p<0.001) for patients with lacunar infarcts after adjustment for age and sex, and was attenuated to 2.6 (95% CI 1.4-4.9, p<0.001) after additional adjustment for vascular risk factors, presence of non-lacunar infarcts, WML and history of stroke. For the presence of silent lacunar infarcts the risk of vascular death was even more increased (HR 4.1, 95% CI 1.9-8.7, p<0.001), adjusted for all covariates.

For every mL increase in WML the HR of vascular death increased with 4% (HR 1.04, 95% CI 1.02-1.06, p<0.001) after adjustment for age and sex, and remained similar after additional adjustment for vascular risk factors, infarcts on MRI and history of stroke (table 3). The HR for vascular death in patients with severe WML compared to patients with less WML was 2.4 (95% CI 1.3-4.2, p<0.001), adjusted for all co-variates.

Non-vascular death

The risk of non-vascular death was significantly increased for patients with lacunar infarcts (HR 2.7, 95% CI 1.3-5.3, p=0.009), after adjusting for all covariates (table 3). Silent lacunar infarcts also increased the risk of non-vascular death after adjusting for all covariates (HR 2.6, 95% CI 1.1-6.0, p=0.028). WML were not associated with non-vascular death (table 3).

Ischemic stroke

Presence of symptomatic lacunar infarcts as well as silent lacunar infarcts significantly increased the risk of ischemic stroke; however, after adjustment for non-lacunar infarcts, WML and history of stroke, this risk decreased and was no longer statistically significant (table 4). Analysis of WML per mL gave similar results, with a HR that was attenuated and no longer significant after adjustment for infarcts on MRI or history of stroke (table 4). However, severe WML significantly increased the risk of ischemic stroke, even after adjustment for all covariates (HR 2.6, 95% CI 1.3-4.9, p<0.001).

Ischemic cardiac complications

Symptomatic as well as silent lacunar infarcts, and WML were not significantly associated with risk of ischemic cardiac complications (table 4).

Diagnosis of atherosclerotic disease at inclusion

Additional adjustment for the diagnosis of atherosclerotic disease at inclusion in all the above described analyses resulted in similar effect estimates and did not change the significance levels (data not shown). Stratification according to the atherosclerotic disease at inclusion showed similar trends, however the number of events were too low to be able to perform all analyses for every atherosclerotic condition (data not shown).

Table 4 **Relationship between the Presence of Lacunar Infarcts and White Matter Lesions and *Ischemic Stroke and Ischemic Cardiac Complication***

	No. of vascular events	No. per 1000 person years	Hazard Ratio (95% CI) Model 1	Model 2	Model 3
Ischemic stroke					
Lacunar infarcts					
Absent (n=1005)	25	4.7	1 [reference]	1 [reference]	1 [reference]
Present (n=223)	21	18.6	3.7 (2.0-6.7)**	3.2 (1.7-5.8)**	1.5 (0.8-3.0)
White matter lesions					
Per ml (n=1228)	46	7.1	1.04 (1.01-1.07)**	1.04 (1.01-1.06)**	1.02 (0.99-1.05)
Upper quintile (n=246)	22	18.3	3.9 (2.1-7.6)**	3.6 (1.9-6.9)**	2.6 (1.3-4.9)**
Ischemic cardiac complication					
Lacunar infarcts					
Absent (n=1005)	52	9.9	1 [reference]	1 [reference]	1 [reference]
Present (n=223)	20	17.4	1.4 (0.8-2.4)	1.5 (0.8-2.5)	1.7 (0.9-3.2)
White matter lesions					
Per ml (n=1228)	72	10.9	1.01 (0.98-1.04)	1.01 (0.98-1.04)	1.01 (0.98-1.04)
Upper quintile (n=246)	25	20.5	1.7 (1.01-2.9)*	1.5 (0.9-2.7)	1.5 (0.9-2.6)

Model 1: *adjusted for age and sex*
Model 2: *additionally adjusted for hypertension, diabetes mellitus, body mass index, smoking (packyears), alcohol consumption and hyperlipidemia*
Model 3: *Lacunar infarcts: additionally adjusted for non-lacunar infarcts on MRI or clinical history of stroke, and white matter lesions*
White matter lesions: additionally adjusted for all other infarcts on MRI or clinical history of stroke
** p < 0.05*
*** p < 0.01*

Secondary analyses

Although the study was performed in a population of atherosclerotic patients, some of them had symptomatic lacunar infarcts as a single diagnosis at inclusion. In total 22 patients were included with symptomatic lacunar infarcts without concomitant coronary artery disease, peripheral artery disease, abdominal aortic aneurysm, or carotid artery stenosis of >50%. Exclusion of these patients did not change the results of our study (data not shown). Likewise, non-lacunar infarcts can be caused by either atherosclerosis or cardioembolism and are therefore not necessarily a manifestation of atherosclerosis. Only 37 patients had non-lacunar infarcts without other manifestations of atherosclerotic disease. Exclusion of these patients did also not change the results (data not shown).

Discussion

We found that the presence of one or more lacunar infarcts on MRI, irrespective whether they were symptomatic or asymptomatic, increased the risk of vascular as well as non-vascular death in patients with symptomatic atherosclerotic disease. Lacunar infarcts also increased the risk of future ischemic stroke, but this could be explained by concomitant infarcts on MRI and a clinical history of stroke. Greater WML-volume increased the risk of vascular, but not non-vascular death or ischemic cardiac complications. Severe WML load increased risk of ischemic stroke, irrespective of concomitant cerebrovascular disease.

Our finding that WML and lacunar infarcts lead to an increased risk of all-cause death is consistent with other studies in different study populations.[5,8,17] Even more interesting was that lacunar infarcts were not only associated with vascular death, but also with non-vascular death. Of course, this finding is dependent on the definition of non-vascular death; in our cohort the majority of the non-vascular deaths were due to fatal malignancy (72.5%). As was previously shown for nephropathy,[16] these results show that the presence of lacunar infarcts is associated with increased morbidity and mortality which is not exclusively due to vascular events. In this light, lacunar infarcts may be a marker of an overall increased vulnerability to adverse outcomes. This indicates the clinical relevance to detect lacunar infarcts in patients with manifestations of atherosclerotic disease outside the brain, as the presence of lacunar infarcts is relevant for the prognosis of these patients. Furthermore, our results show that silent lacunar infarcts, which are in general not treated, are actually important for the prognosis of patients. Previous studies have shown that treatment with statins can improve vascular function in patients with symptomatic lacunar infarcts and WML.[20] However, further research is needed to investigate whether this treatment also improves the clinical outcome and prognosis of patients with asymptomatic lacunar infarcts and WML.

For lacunar infarcts the increased risk of ischemic stroke was explained by other infarcts on MRI and a clinical history of stroke. Patients with severe WML load did have an increased risk of ischemic stroke after adjusting for other infarcts and history of stroke. This is in line with two other studies in older populations that found a relation between WML and risk of ischemic stroke, although those were not adjusted for other infarcts.[11, 21] Interesting are the differential associations of lacunar infarcts and WML with non-vascular death and ischemic stroke. Although it is thought that lacunar infarcts and WML are both caused by changes in the small vessels in the brain, our findings suggest that the prognosis may be different and we tentatively hypothesize that lacunar infarcts and WML may actually be two separate forms of cerebral small vessel disease. Further studies of lacunar infarcts and WML within one study population and in population-based studies are needed to investigate this hypothesis.

Strengths of our study are the large number of patients included, the virtually complete follow-up, the rigorous assessment of clinical outcomes, the analyses within patients without clinical history of stroke, the automated brain segmentation, and the adjustment of confounders. Besides that, the large number of patients enabled us to do the analysis in patients with silent lacunar infarcts. Although most silent infarcts are lacunar infarcts, also non-lacunar infarcts can be silent. Previously published studies investigated silent infarcts in general and did not look specifically at lacunar infarcts.[7] Furthermore, our study is the first to specifically investigate non-vascular death. A limitation of our study may be that it is difficult to verify if silent infarcts are really clinically asymptomatic. We tried to minimize misclassification by excluding patients who had TIA or stroke at inclusion or reported a TIA or stroke in the past.

In conclusion, lacunar infarcts and white matter lesions on MRI are risk factors for adverse outcomes in patients with atherosclerotic diseases. Further research is needed to investigate whether the presence of lacunar infarcts or white matter lesions have added value in models to predict prognosis in patients with atherosclerotic disease.

Chapter 02 Cerebral small vessel disease and the risk of death, ischemic stroke and cardiac complications in patients with atherosclerotic disease. The SMART-MR study

References

1 Bots ML, van Swieten JC, Breteler MM, de Jong PT, van Gijn J, Hofman A, Grobbee DE. Cerebral white matter lesions and atherosclerosis in the Rotterdam Study. *Lancet* 1993;341:1232-1237.

2 Breteler MM, van Swieten JC, Bots ML, Grobbee DE, Claus JJ, van den Hout JH, Van Harskamp F, Tanghe HL, de Jong PT, van Gijn J. Cerebral white matter lesions, vascular risk factors, and cognitive function in a population-based study: the Rotterdam Study. *Neurology* 1994;44:1246-1252.

3 Wardlaw JM, Doubal F, Armitage P, Chappell F, Carpenter T, Munoz MS, Farrall A, Sudlow C, Dennis M, Dhillon B. Lacunar stroke is associated with diffuse blood-brain barrier dysfunction. *Ann Neurol* 2009;65:194-202.

4 Wardlaw JM, Sandercock PA, Dennis MS, Starr J. Is breakdown of the blood-brain barrier responsible for lacunar stroke, leukoaraiosis, and dementia? *Stroke* 2003;34:806-812.

5 de Jong G, Kessels F, Lodder J. Two types of lacunar infarcts: further arguments from a study on prognosis. *Stroke* 2002;33:2072-2076.

6 Debette S, Beiser A, DeCarli C, Au R, Himali JJ, Kelly-Hayes M, Romero JR, Kase CS, Wolf PA, Seshadri S. Association of MRI markers of vascular brain injury with incident stroke, mild cognitive impairment, dementia, and mortality: the Framingham Offspring Study. *Stroke* 2010;41:600-606.

7 Vermeer SE, Longstreth WT, Jr., Koudstaal PJ. Silent brain infarcts: a systematic review. *Lancet Neurol* 2007;6:611-619.

8 Ikram MA, Vernooij MW, Vrooman HA, Hofman A, Breteler MM. Brain tissue volumes and small vessel disease in relation to the risk of mortality. *Neurobiol Aging* 2010;30:450-456.

9 Mathers CD, Loncar D. Projections of global mortality and burden of disease from 2002 to 2030. *PLoS Med* 2006;3:e442.

10 Geerlings MI, Appelman AP, Vincken KL, Algra A, Witkamp TD, Mali WP, van der Graaf Y. Brain volumes and cerebrovascular lesions on MRI in patients with atherosclerotic disease. The SMART-MR study. *Atherosclerosis* 2010;210:130-136.

11 Gerdes VE, Kwa VI, ten Cate H, Brandjes DP, Buller HR, Stam J. Cerebral white matter lesions predict both ischemic strokes and myocardial infarctions in patients with established atherosclerotic disease. *Atherosclerosis* 2006;186:166-172.

12 Ikram MA, Vernooij MW, Hofman A, Niessen WJ, van der Lugt A, Breteler MM. Kidney function is related to cerebral small vessel disease. *Stroke* 2008;39:55-61.

13 Kwa VI, van der Sande JJ, Stam J, Tijmes N, Vrooland JL. Retinal arterial changes correlate with cerebral small-vessel disease. *Neurology* 2002;59:1536-1540.

14 Gamble CN. The pathogenesis of hyaline arteriolosclerosis. *Am J Pathol* 1986;122:410-420.

15 van Swieten JC, van den Hout JH, van Ketel BA, Hijdra A, Wokke JH, van Gijn J. Periventricular lesions in the white matter on magnetic resonance imaging in the elderly. A morphometric correlation with arteriolosclerosis and dilated perivascular spaces. *Brain* 1991;114:761-774.

16 Rifkin DE, Katz R, Chonchol M, Fried LF, Cao J, de Boer I, Siscovick DS, Shlipak MG, Sarnak MJ. Albuminuria, impaired kidney function and cardiovascular outcomes or mortality in the elderly. *Nephrol Dial Transplant* 2010;25:1560-1567.

17 Briley DP, Haroon S, Sergent SM, Thomas S. Does leukoaraiosis predict morbidity and mortality? *Neurology* 2000;54:90-94.

18 Anbeek P, Vincken KL, van Osch MJ, Bisschops RH, van der Grond J. Automatic segmentation of different-sized white matter lesions by voxel probability estimation. *Med Image Anal* 2004;8:205-215.

19 Anbeek P, Vincken KL, van Osch MJ, Bisschops RH, van der Grond J. Probabilistic segmentation of white matter lesions in MR imaging. *Neuroimage* 2004 ;21:1037-1044.

20 Sterzer P, Meintzschel F, Rosler A, Lanfermann H, Steinmetz H, Sitzer M. Pravastatin improves cerebral vasomotor reactivity in patients with subcortical small-vessel disease. *Stroke* 2001;32:2817-2820.

21 Vermeer SE, Hollander M, Van Dijk EJ, Hofman A, Koudstaal PJ, Breteler MM. Silent brain infarcts and white matter lesions increase stroke risk in the general population: the Rotterdam Scan Study. *Stroke* 2003;34:1126-1129.

CHAPTER 03

Perforating arteries originating from the posterior communicating artery: a 7 Tesla MRI study

Mandy M.A. Conijn
Jeroen Hendrikse
Jaco J.M. Zwanenburg
Taro Takahara
Mirjam I. Geerlings
Willem P.Th.M. Mali
Peter R. Luijten

Abstract

Background and Purpose

The aim of this study was to investigate the ability of time-of-flight (TOF) magnetic resonance (MR) angiography at 7 Tesla to show the perforating branches of the posterior communicating artery (PCoA), and to investigate the presence of such visible perforating branches in relation to the size of the feeding PCoA. The secondary aim was to visualise and describe the anterior choroidal artery and the perforating branches of the P1-segment of posterior cerebral artery (P1).

Methods

Forty-six healthy volunteers underwent TOF MR angiography at 7 Tesla MRI. Presence of a PCoA and anterior choroidal artery and presence of perforating arteries of the PCoA and P1 were analysed. The diameter of the P1-segment of the posterior cerebral artery (P1), PCoA and perforating artery were measured by taking the full-width-at-half-maximum of the intensity profiles.

Results

With 7 Tesla imaging, we visualised for the first time perforating arteries originating from the PCoA in vivo, without the use of contrast agents. A perforating artery from the PCoA was found in a large proportion of the PCoAs (64%). The presence was associated with a larger diameter of the underlying PCoA (1.23 mm versus 1.06 mm, p = 0.03). The anterior choroidal artery was visible bilaterally in all participants. In 83% of all P1's one or two perforating branches were visible.

Conclusion

Non-invasive assessment of the perforating arteries of the PCoA together with the anterior choroidal artery and the perforating arteries of the P1 at 7 Tesla may increase our understanding of infarcts in the deep brain structures supplied by these arteries.

Introduction

The posterior communicating artery (PCoA) is an important component of the circle of Willis. A large variability exists in the configuration of the PCoA, which can be large, hypoplastic or even absent in some cases. In addition, two configurations of the posterior part of the circle of Willis can be distinguished: a non-foetal configuration, when the diameter of the PCoA is smaller than the diameter of the ipsilateral P1 segment of the posterior cerebral artery (P1), and a foetal configuration, when the diameter of the PCoA is larger than the diameter of the ipsilateral P1.

A small or absent PCoA appears to be a risk factor for ischaemic lesions of the brain. Ischaemic cerebral infarctions are more often found in patients with a small or absent PCoA than in patients with a large PCoA, independent of the presence of internal carotid artery occlusion.[1,2] A foetal variant of the PCoA has been found to be less common in patients with occipital lobe infarctions than in healthy controls.[3] Besides ischaemic cerebral infarctions, the PCoA also seems to be an important determinant in the aetiology of white matter lesions. A study among patients with clinical manifestations of atherosclerotic disease demonstrated a decreased deep white matter lesion load in patients with a foetal configuration of the circle of Willis,[4] although these results were not confirmed in a different population.[5]

Lacunar infarctions are thought to result from occlusion of deep perforating arteries, also called the thalamoperforating arteries.[6,7] A potential protective effect of a large PCoA against ischaemic brain lesions may be explained by the perforating arteries branching from the PCoA, which feed the deep brain structures and deep white matter.[1-4] Thus far, these perforating arteries could only be assessed post-mortem or via intra-arterial digital subtraction angiography (iaDSA) [8,9] or rotational angiography.[10] Therefore, limited studies have investigated the perforating arteries and little is known about the perforating arteries branching from the PCoA. Recently, MR angiography at the field strength of 7 Tesla was introduced as a non-invasive alternative to depict the perforating branches of the circle of Willis.[11] This ultra-high field strength makes it possible to visualise submillimeter vessels for the first time in vivo without the use of any contrast agents.

The primary aim of the present study is to assess the ability of time-of-flight MR angiography at 7 Tesla to show the perforating branches of the posterior communicating artery, and to investigate the presence of such perforating branches in relation to the size of the feeding posterior communicating artery and the configuration of the posterior part of the circle of Willis. The secondary aim is to assess the ability to visualise the perforating branches of the P1, and to describe these branches and to describe the anterior choroidal artery.

Methods

Participants

Forty-six healthy volunteers (25 men and 21 women, mean age of 30 (±12.6) years) from the local university were included. None of them reported a history of neurological or vascular disease.

The study was approved by the medical ethics committee of the Medical Center in Utrecht and written informed consent was obtained from all participants.

MR Imaging

MR imaging was performed with a 7 Tesla whole-body system (Philips Healthcare, Cleveland, OH, USA), using a volume transmit and a 16-channel receive-only head coil (Nova Medical, Wilmington, MA, USA). Time-of-flight (TOF) MR angiography was performed in each participant using a turbo field echo sequence, with a presaturation slab positioned superior to the imaging volume to suppress the venous blood and applied once per 230 ms to avoid specific absorption rate (SAR) constraints. Two variants of the TOF angiography were used, with a slightly different resolution. In the first variant the acquired voxel size was 0.6 x 0.6 x 0.6 mm^3, for the second variant this was 0.4 x 0.5 x 1.0 mm^3. The other imaging parameters were: field of view (FOV) 200 x 181 x 68 mm; acquired matrix of 332 x 294 for the variant with 0.6 x 0.6 mm in-plane resolution and 500 x 354 for the variant with 0.4 x 0.5 mm in-plane resolution; repetition time (TR) 23 ms and echo time (TE) 2.3 - 2.6 ms, depending on the resolution and angulation. Excitation pulses consisted of tilt-optimised non-saturated excitation (TONE) pulses with nominal flip angle variation of 16°-24° in the feet–head direction over the slab. The slab was acquired in a series of 4 thinner chunks (17.5 mm each) to increase the inflow effect. Sensitivity encoding (SENSE) was applied in the RL direction with an acceleration factor of 3. The images were reconstructed to 0.3 mm isotropic voxels, and the built-in phase correction and partial-echo filter of the scanner was applied during reconstruction. The imaging duration was approximately 9 minutes and 30 seconds.

Post-processing

All images were exported to an offline workstation, equipped with the same viewing software as the 7 Tesla MR system. The post-processing of the angiographic data was performed on the standard console. Maximum intensity projections (MIPs) were reconstructed for transversal slabs (thickness 3 mm, 2 mm overlap, 30 slices) and for sagittal slabs (thickness 3 mm, 2 mm overlap, 50 slices and thickness 0.3 mm, no overlap, 250 slices), and a coronal reconstruction (thickness 0.3 mm, no overlap, 150 slices) was made from the axial source dataset of the TOF MR angiograms.

On the transversal slab MIP intensity profiles for both the left and right P1 were obtained, as illustrated in figure 1 (a, b). The software programme Matlab (v. 7.6, MathWorks, Natick, MA) was used to calculate the full width at half maximum (FWHM) of the profiles. We took the FWHM as an estimate of the diameter of the P1.

The thin 0.3-mm sagittal slab MIP was used to investigate whether the PCoA was visible on the left and the right sides and, when a PCoA was found, to identify perforating arteries branching from the PCoA. If no perforating branches were visible, an intensity profile was made at one point of the PCoA and the FWHM was calculated to estimate the diameter. If an image did show a perforating artery branching from the PCoA, intensity profiles were

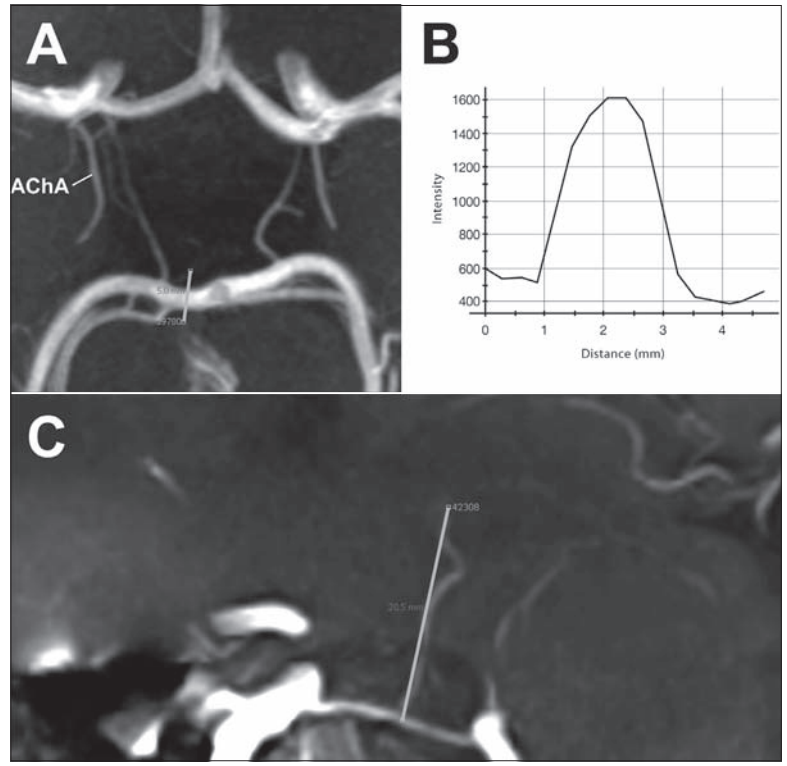

Figure 1 | [**A**] *Time-of-flight angiography image of the circle of Willis and the anterior choroidal artery (AChA) on 7 Tesla MRI, transversal slab maximum intensity projection (thickness 7mm). A line was set perpendicular to the left P1 and the corresponding intensity profile* [**B**] *is shown.* [**C**] *This image shows the posterior communicating artery with a perforating branch on a sagittal slab maximum intensity projection (thickness 7mm). A line was set from the origin of the perforator to the last point at which the perforator was visible to obtain a rough estimate of the length of the perforator*

obtained both anterior to the branch and posterior to the branch. For the overall diameter of the PCoA, the mean of the diameter anterior and posterior of the branch was calculated. To estimate the diameter of the branch itself, an additional intensity profile was obtained for which the FWHM was calculated.

To obtain a rough estimate of the length of the perforating branches, measurements were performed by drawing a line from the most distal part, where the branch was still visible, back to the origin of the branch at the level of the PCoA on the sagittal 7-mm slab MIP reconstructions (figure 1c). Although this method does not take the curvature of the vessel into account and is measured on a slab MIP projection, this measurement was only used to get an indication of the length over which the perforators are visible on 7 Tesla MR angiography.

The 3-mm sagittal slab MIP was used to obtain intensity profiles of the left and right anterior choroidal artery to calculate the FWHM. Because of the variation in diameter of the anterior choroidal artery, three intensity profiles were obtained per artery between the origin of the artery at the internal carotid artery and the point were the anterior choroidal artery diverges from the PCoA. Of these three measurements, the mean was taken as the diameter of the anterior choroidal artery.

The presence of perforating branches from the P1 was investigated on the thin 0.3-mm coronal reconstruction, and the branches from the left and right P1 were counted. Because of the relatively low contrast between the arteries and the background and their rather tortuous course it was not possible to obtain a diameter or length measurement of these arteries.

Statistical analysis

In participants in whom a PCoA was found, we used the unpaired t-test to test for differences in PCoA diameter between PCoAs with and without a perforating branch. The sides on which no PCoA was found were left out of the analysis. The two configurations of the posterior part of the circle of Willis, the non-foetal configuration (diameter PCoA < diameter P1) and the foetal configuration (diameter PCoA > diameter P1), were analysed. The presence of a perforating PCoA branch was compared in these two configurations with use of the chi-squared test.

For all measurements together and for the left and the right hemispheres separately, the correlation between the diameter of the P1 and the diameter of the ipsilateral PCoA were evaluated. The correlation between the left and right hemispheres was analysed for the diameter of the P1, the diameter of the PCoA and the diameter of the P1 divided by the diameter of the PCoA (P1/PCoA ratio). A p value < 0.05 was considered significant.

Results

Figure 2 shows a typical example of a perforating artery branching from the PCoA in a sagittal slab MIP.

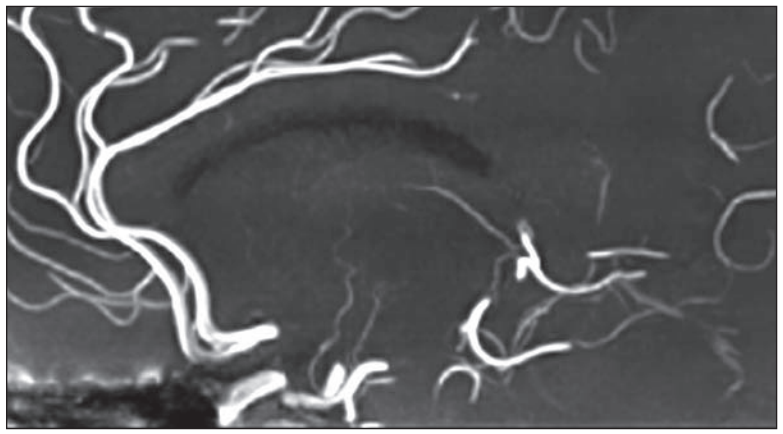

Figure 2 | *Time-of-flight angiography image of the posterior communicating artery with a perforating branch on 7 Tesla MRI, sagittal slab maximum intensity projection (thickness 7 mm)*

There was bilateral absence of a visible PCoA in 2 of the 46 participants (4.4%), unilateral absence was found in 7 (15.2%), and in 37 participants (80.4%) the PCoA was visible bilaterally (table 1). Taking the left and right hemispheres together, a PCoA was visible in 81 of the 92 hemispheres (88.1%), of which 52 (64.2%) had a visible perforating artery and 29 (35.8%) had no perforating artery.

Table 1 **Unilateral and bilateral absence and presence of a visible PCoA**

PCoA	Participants/hemispheres (%)
Bilateral absent	2/4 (4.3%)
Unilateral absent	7/14 (15.2%)
Bilateral present	37/74 (80.4%)
Total	46/92 (100%)

Within the left hemisphere 39 (84.8%) of the 46 participants had a visible PCoA, of whom 23 (59.0%) showed a perforator and 16 (41.0%) did not show a perforator. In the right hemisphere a PCoA was found in 42 out of 46 participants (91.3%), 29 (69.0%) with a perforator and 13 (31.0%) without a perforator. Two visible perforators branching from one PCoA were found for two PCoAs, both in the right hemisphere (figure 3).

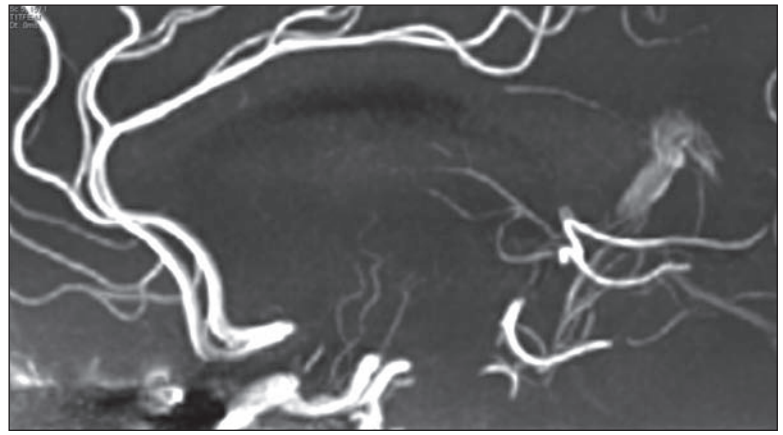

Figure 3 | *Time-of-flight angiography image of the posterior communicating artery with two perforating branches, sagittal slab maximum intensity projection (thickness 10 mm)*

The mean diameter of the perforating arteries was 0.72 mm (SD 0.15). With the method we used to indicate the length, the mean length of the perforating arteries was 19.3 mm (SD 6.4), ranging from 6.1 mm to 36.0 mm.

No correlation was found between the diameter of the P1, the diameter of the PCoA or the presence of a perforating artery and age or gender.

The mean diameter of all PCoAs with a visible accompanying perforator was 1.23 mm (SD 0.35); this was 1.22 mm (SD 0.33) for the left hemisphere and 1.24 mm (SD 0.38) for the right hemisphere. For the PCoAs without a perforator present, the mean diameter was smaller, 1.06 mm (SD 0.34) for all PCoAs together; 1.05 mm (SD 0.32) for the left hemisphere and 1.07 mm (SD 0.38) for the right hemisphere. Taking the left and right hemispheres together, the overall difference in diameter is 0.18 mm (SD 0.08, p = 0.030) in favour of the PCoA with a perforator; 0.18 mm (SD 0.11, p = 0.101) for the left and 0.18 mm (SD 0.13, p = 0.172) for the right hemispheres separately.

Of all the 81 hemispheres in which a PCoA was present, there was a foetal configuration (diameter PCoA > diameter P1) in 16 hemispheres and a non-foetal configuration (diameter PCoA < diameter P1) in 65 hemispheres. Of those with a foetal configuration, 12 (75.0%) had a visible perforating branch; this was 40 (61.5%) for the participants with a non-foetal configuration (table 2). Although a perforating branch was present more often in cases of foetal configuration, this difference was not significant (p = 0.392).

Table 2 **Configuration of the posterior part of the circle of Willis and presence of a perforator**

Configuration	Hemispheres (%)	Perforator present | not present (%)	
Fetal (PCoA > P1)	16 (17.4%)	Present: 12 (75.0%)	Not present: 4 (25.0%)
Non-fetal (PCoA < P1)	65 (70.7%)	Present: 40 (61.5%)	Not present: 25 (38.5%)
Subtotal	**81 (88.1%)**	**Present 52 (64.2%)**	**Not present: 29 (35.8%)**
No PCoA	11 (11.9%)	Present: 0 (0%)	Not present: 11 (100%)
Total	92 (100%)	Present: 52 (56.5%)	Not present: 40 (43.5%)

Furthermore, we analysed the correlation between the diameter of the P1 and the diameter of the PCoA. Overall, a correlation with a correlation coefficient of -0.575 ($p < 0.001$, figure 4) was found; for the P1 and the PCoA in the left hemisphere separately the correlation coefficient was -0.598 ($p < 0.001$) and for the right hemisphere separately this was -0.663 ($p < 0.001$).

The data showed a correlation between the left and the right halves of the posterior part of the circle of Willis for the diameter of the P1 ($R = 0.457$, $p = 0.002$), the diameter of the PCoA ($R = 0.554$, $p < 0.001$) and for the P1/PCoA ratio ($R = 0.462$, $p = 0.005$).

A visible anterior choroidal artery was found bilaterally in all participants, with a mean diameter of 0.83 mm (SD 0.14).

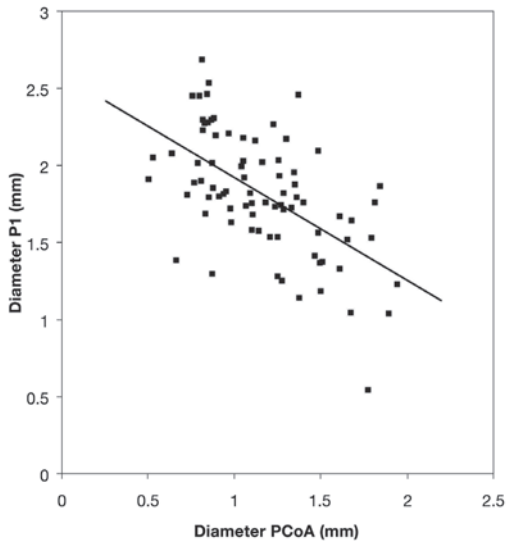

Figure 4 | *Correlation between the diameter of the P1 and the PCoA for P1 and the PCoA of the left and right sides together. Correlation coefficient -0.575 ($p < 0.001$). P1: P1 segment of the posterior cerebral artery; PCoA: posterior communicating artery*

Figure 5 shows an example of perforating arteries originating from the left and right P1. Taking the left and right P1 together, no perforators were visible in 16% of the P1's, one single perforator was visible in 63% and two visible perforators were present in 20% of the P1's. There was no significant difference in diameter between a P1 with one or two perforating arteries and a P1 without a perforating artery.

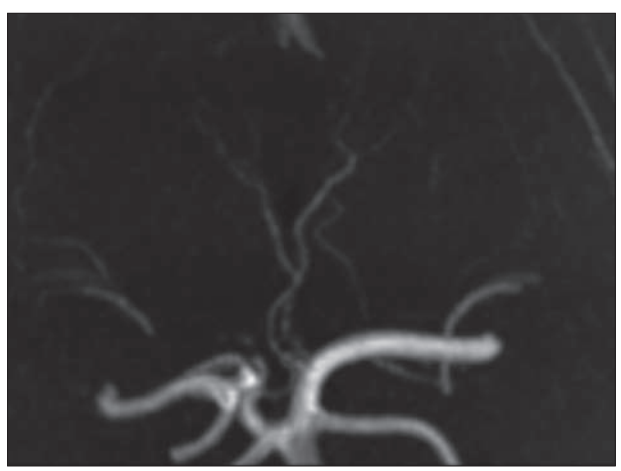

Figure 5 | *Time-of-flight angiography image of the left and right P1 segment of the posterior cerebral artery (P1) with two perforating branches, one perforating artery originates from the left P1 and one originates from the right P1. Coronal slab maximum intensity projection, thickness 10 mm.*

Discussion

Time-of-flight MR angiography at 7 Tesla showed the presence of a clearly visible perforating branch of the PCoA on 52 of the 81 sides on which a PCoA was present (64.2%). The presence of a perforating branch from the posterior perforating artery was associated with a larger diameter of the posterior communicating artery. Furthermore, a significant correlation was found between the diameter of the P1 and the diameter of the PCoA, and a significant correlation between the left and right halves of the posterior part of the circle of Willis for the diameter of the P1, the diameter of the PCoA and the P1/PCoA ratio.

In the present study with TOF MR angiography at 7 Tesla we found bilateral absence of a visible PCoA in only 4.3% and unilateral absence in 15.2%. In a previous study with TOF MR angiography at 1.5 Tesla, the absence of a visible PCoA was higher: the authors found bilateral absence of a PCoA in 11% of the participants and unilateral absence in 34% of the participants.[12] These results suggest that the number of unilateral or bilateral invisible PCoAs is lower at 7 Tesla, which shows the higher sensitivity of a smaller vasculature and a low flow at a higher field strength. According to the post-mortem examinations of the circle of Willis, the bilateral absence of a PCoA is very rare (0.25%) and the unilateral absence of a PCoA is found in 2.25-3.0%.[13] Therefore, in most of the participants in the present study without a visible PCoA this will probably be caused by low flow through the PCoA or a very small diameter. The PCoA is a unique artery that forms a connection between the anterior and posterior cerebral circulation. Thus, in the case of a balanced blood supply anteriorly and posteriorly through the circle of Willis, the blood flow through the PCoA can be very low compared with the diameter.

In our study we show the presence of a visible perforating branch originating from the PCoA in 64.2% of the sides on which a PCoA is visible. Compared with post-mortem studies the current prevalence of perforators branching from the posterior communicating artery will also be an underestimation because of very low flow velocities in smaller perforating arteries, which make these arteries invisible even on the current TOF MR angiography images at 7 Tesla. Besides that, due to intravoxel dispersion effects ('partial volume'), signal reduction occurs. As a result the signal of these very small arteries might be too low to be detectable as an artery.

The diameter measurements of the perforating branch of the posterior communicating artery reveal that we can detect perforators with a minimal size of about 0.41 mm. The ability to show these perforators over a length of up to approximately 36.0 mm in their course into the deep brain structures demonstrates the sensitivity of the current technique for these perforating arteries. Furthermore, two perforators branching from one PCoA were also detected in 2 out of 52 hemispheres with these perforators.

When measuring the diameter of a vessel on an angiogram with use of the FWHM-method, the accuracy of the FWHM-method on vessels with a diameter that is close to the voxelsize, should be considered. The smallest artery we measured in this study was the perforating artery from the PCoA. The mean diameter of this artery was 0.72 mm (SD 0.15 mm), so this measurement will be in most cases based on about 1 to 2 acquired pixels in the lumen of the vessel. According to a study of the accuracy of vessel diameter measurement in MR angiography, measurements with one to three pixel/diameter will give an error in the estimation of the diameter, which can be an overestimation, but even an underestimation.[14] This error is approximately 30% at most, so in case of a vessel of 0.41 mm, the actual diameter will lie between 0.29 mm and 0.53 mm.

An overall association was found between the presence of a perforator originating from the PCoA and a larger size of the PCoA, although this was only significant for the left and right sides combined. A possible explanation for this association could be that more flow via the PCoA is needed to supply such a branch, resulting in a larger diameter of the PCoA on flow-weight MR angiography images. However, the expected amount of blood needed to feed a perforating artery is most likely too small to cause a measurable change in diameter. Therefore, we consider that the relation between a perforator branching from the PCoA has its origin in the developmental phase of the cerebral vasculature. In its embryological development there will be a higher chance of a perforator

originating from the PCoA from a large than a perforator originating from a small PCoA. That the results are not significant for the left and right sides separately is possibly because of the relatively small number of participants in the study. We would expect this association to become significant when analysed in a larger study.

The correlation between the left and right halves of the posterior part of the circle of Willis, for the P1, the PCoA and the P1/PCoA ratio, shows us the relation between the blood supply of the left and the right hemispheres. If one side has a large diameter, the other side will probably also have a relatively large diameter. Not only the diameter of the P1 and the diameter of the PCoA show this relation, which can be caused by larger vessels in general within one person, but also the P1/PCoA ratio is related. This indicates that the blood supplies in the left and right hemispheres, originating from the circle of Willis, are associated. As with the P1/PCoA ratio itself, it is most likely that the relation between the left and right sides of the circle of Willis is also already determined in the developmental stage of the brain.

In this study we also found a significant correlation between the diameter of the P1 and the diameter of the PCoA. It shows that with a larger diameter of the P1, the diameter of the PCoA in general will be smaller. This could be expected, because when there is more blood supply via the P1, the diameter will be larger and less blood flow via the PCoA is needed, so the diameter of the PCoA will be smaller. The observation of a smaller diameter of the PCoA suggests that the overall blood supply to the posterior part of the brain might be regulated by both P1 and PCoA.

The present MR angiography technique, with a detailed depiction of perforating branches of the arteries at the level of the circle of Willis, may be helpful in increasing understanding of the variations in normal anatomy in vivo and to improve knowledge of the pathophysiology of ischaemia in the deep brain structures. The presence of a large perforating branch from the PCoA may protect the deep brain structures, such as the thalamus, from ischaemia.[2] In addition to lacunar infarcts, the presence of perforating branches may enhance our understanding of small vessel disease, resulting in leukoaraiosis. We speculate that the smaller amount of lacunar infarcts and white matter lesions observed in previous studies in patients with a larger PCoA might be explained by a protective effect of the presence of a large perforating branch from the PCoA.

Although only the PCoA has been investigated in relation with ischemic brain lesions, also the collateral bloodsupply is important in case of ischaemic lesions. The anterior choroidal artery and the perforating arteries that originate from the P1 are important arteries to provide collateral bloodsupply to the area supplied by the perforating arteries originating from the PCoA. Especially in the case of ischaemic brain lesions these vessels can play an important role in the collateral bloodsupply. The TOF MR angiography at 7 Tesla showed the bilateral presence of the anterior choroidal artery in all participants. Also the perforating branches originating from the P1 were clearly visualised in a large proportion of the P1's (83%), 63% with one visible branch and 20% with two visible branches from the P1.

In conclusion, we show the capacity of MR angiography at 7 Tesla to show the perforating branches of the PCoA and by doing so we showed the relation between the presence of these perforators and the anatomy of the PCoA. Furthermore, we found a significant correlation between the diameters of the P1 and the PCoA, and between the left and right sides of the circle of Willis. Perforating arteries originating from the P1 and the anterior choroidal artery are also clearly visualised with 7 Tesla angiography. In future studies, the detailed assessment of the perforating arteries originating from the PCoA with non-invasive MR angiography may increase our understanding of infarcts in the deep brain structures supplied by these perforating arteries.

References

1 Schomer DF, Marks MP, Steinberg GK, Johnstone IM, Boothroyd DB, Ross MR, Pelc NJ, Enzmann DR. The anatomy of the posterior communicating artery as a risk factor for ischemic cerebral infarction. *N Engl J Med* 1994 2;330:1565-1570.

2 Chuang YM, Liu CY, Pan PJ, Lin CP. Posterior communicating artery hypoplasia as a risk factor for acute ischemic stroke in the absence of carotid artery occlusion. *J Clin Neurosci* 2008;15:1376-1381.

3 Jongen JC, Franke CL, Ramos LM, Wilmink JT, van Gijn J. Direction of flow in posterior communicating artery on magnetic resonance angiography in patients with occipital lobe infarcts. *Stroke* 2004;35:104-108.

4 van der Grond J, van Raamt AF, van der Graaf Y, Mali WP, Bisschops RH. A fetal circle of Willis is associated with a decreased deep white matter lesion load. *Neurology* 2004 26;63:1452-1456.

5 Ikeda K, Kashihara H, Hosozawa KI, Shimoma M, Ichikawa Y, Igarashi O, Aoyagi J, Tamura M, Iwasaki Y. A fetal circle of Willis is associated with a decreased deep white matter lesion load. *Neurology* 2005;64:2163-2164.

6 Fisher CM. The arterial lesions underlying lacunes. *Acta Neuropathol* 1968;12:1-15.

7 Wardlaw JM, Dennis MS, Warlow CP, Sandercock PA. Imaging appearance of the symptomatic perforating artery in patients with lacunar infarction: occlusion or other vascular pathology? *Ann Neurol* 2001;50:208-215.

8 Anxionnat R, Bracard S, Ducrocq X, Trousset Y, Launay L, Kerrien E, Braun M, Vaillant R, Scomazzoni F, Lebedinsky A, Picard L. Intracranial aneurysms: clinical value of 3D digital subtraction angiography in the therapeutic decision and endovascular treatment. *Radiology* 2001;218:799-808.

9 Shimizu S, Suzuki H, Maki H, Maeda M, Miya F, Benali K, Trousset Y, Taki W. A novel image fusion visualizes the angioarchitecture of the perforating arteries in the brain. *AJNR Am J Neuroradiol* 2003;24:2011-2014.

10 Kang HS, Han MH, Kwon BJ, Kwon OK, Kim SH, Chang KH. Evaluation of the lenticulostriate arteries with rotational angiography and 3D reconstruction. *AJNR Am J Neuroradiol* 2005;26:306-312.

11 Zwanenburg JJ, Hendrikse J, Takahara T, Visser F, Luijten PR. MR angiography of the cerebral perforating arteries with magnetization prepared anatomical reference at 7 T: comparison with time-of-flight. *J Magn Reson Imaging* 2008;28:1519-1526.

12 Krabbe-Hartkamp MJ, van der Grond J, De Leeuw FE, De Groot JC, Algra A, Hillen B, Breteler MM, Mali WP. Circle of Willis: morphologic variation on three-dimensional time-of-flight MR angiograms. *Radiology* 1998;207:103-111.

13 Yasargil MG. *Microneurosurgery* 1984, I ed. Stuttgart: Georg Thieme Verlag, pp 60-135

14 Hoogeveen RM, Bakker CJ, Viergever MA. Limits to the accuracy of vessel diameter measurement in MR angiography. *J Magn Reson Imaging* 1998;8:1228-1235.

CHAPTER 04

Visualization of cerebral microbleeds with dual echo T2*-weighted MR imaging at 7 Tesla

Mandy M.A. Conijn
Mirjam I. Geerlings
Peter R. Luijten
Jaco J.M. Zwanenburg
Fredy Visser
Geert-Jan Biessels
Jeroen Hendrikse

Abstract

Background and Purpose

Increasing interest in microbleeds has led to a number of studies examining the prevalence and clinical relevance of these lesions. Prevalence estimates differ substantially between studies, due to differences in image protocols and field strengths. The aim of this study was to assess the visualization of cerebral microbleeds with dual echo T2*-weighted imaging at 7 Tesla MRI.

Methods

Ten consecutive participants (8 men, 2 women, mean age 54±12 years) with vascular disease or risk factors from the Second Manifestations of ARTerial disease (SMART) study were included. Dual echo T2*-weighted scans (echo time: 2.5/15.0ms) were made for all participants at 7 Tesla MRI. The number of visible microbleeds and the diameter of the microbleeds were recorded on minimal intensity projection images of both echoes.

Results

The first echo image shows dark microbleeds against a homogeneous, more hyperintense signal of the brain tissue without contrast for veins and basal ganglia. In 8 patients microbleeds were observed, with a total of 104 microbleeds. Of these, 88 (84.6%) were visible on the first and 102 (98.0%) on the second echo. The mean diameter of the microbleeds was 1.24mm for the first echo and 2.34mm for the second echo.

Conclusion

T2*-weighted imaging at two echo times at 7 Tesla combines the advantages of the first and second echo. Microbleeds visible on the first echo show large contrast with the surrounding tissue, even in the presence of paramagnetic ferritin. The second echo enables visualization of smaller microbleeds than the first echo.

Introduction

The interest in cerebral microbleeds is growing, as is shown by the increasing number of studies investigating the prevalence and the clinical relevance of these lesions. The studies done up till now have increased the understanding of cerebral microbleeds. They have shown that cerebral microbleeds appear to be direct markers of vascular disease, as they are associated with hypertensive vasculopathy and cerebral amyloid angiopathy, and also with white matter lesions and lacunar infarcts.[1-6] The finding of microbleeds can be of major importance in patients with ischemic stroke receiving anticoagulation, as the presence of microbleeds might indicate a higher risk of future intracerebral haemorrhage, although this is still under debate.[7-12] Furthermore, some studies have shown that microbleeds are associated with cognitive impairment, functional dependence or death.[3,13,14] However, as some of these associations are still under debate and the clinical implication of microbleeds is not completely clear, more and larger studies are needed to obtain more information about microbleeds.[3]

The number of microbleeds detected, and with that the study sensitivity, differs strongly between different image protocols and different field strengths. This can be illustrated by the varying prevalences of microbleeds found in different studies. The prevalence found in population based studies ranges from 4.7% to 23.5%.[15,16] An optimal imaging protocol for the visualization of microbleeds is hard to define, because there is no reference test available of the detection of these lesions.

Microbleeds consist of haemosiderin deposits that are paramagnetic, due to the presence of paramagnetic iron. This induces a susceptibility effect on the MRI scan, which leads to a fast decay of the local T2*-weighted MRI signal because of a local inhomogeneity of the field induced by the internal magnetization of microbleeds. T2*-weighted gradient-recalled echo (GRE) has been shown to be highly sensitive to this susceptibility effect, and is therefore very sensitive to microbleeds.[2,3,17] As the effect scales with the magnetic field, the detection of microbleeds is substantially improved at ultra-high field strengths. Moreover, increased signal to noise (SNR) can be used for higher spatial resolution and increased conspicuity of small haemosiderin deposits that may be obscured by partial volume effects at lower field strengths that operate at lower spatial resolution.[18]

Besides the field strength, also the echo time is an important parameter for the visualization of microbleeds. A longer echo time gives more time for dephasing, which enhances the susceptibility effect. This so-called blooming effect causes the microbleeds to appear as hypointense spots that are larger than the actual size. It has been shown that prolonging the echo time leads to an increase in diameter of these lesions and also detection of an increased number of microbleeds.[19] However, microbleeds can also be obscured by overlapping structures with a high susceptibility effect, like veins (deoxyhemoglobin) or the basal ganglia (ferritin deposition). With a longer echo time, these structures will also increase in size and become more dominant, making it harder to distinguish the microbleeds.

The magnetic characteristics of paramagnetic substances such as deoxyhemoglobin, ferritin and haemosiderin, depend largely on the amount of iron present. Deoxyhemoglobin in veins is less paramagnetic than ferritin depositions in the basal ganglia and haemosiderin depositions in microbleeds, which have strong paramagnetic iron-containing cores. Haemosiderin is a degradation product of ferritin, in which the iron cores are more closely packed,[20] which explains why haemosiderin was shown to have a stronger T2 shortening effect than ferritin.[21-23] As the magnetic characteristics of deoxyhemoglobin, ferritin and haemosiderin are different, the blooming effect as a function of echo time will also be different.

With use of a shorter echo time, it may be possible to better distinguish the haemosiderin containing microbleeds from other structures with a high susceptibility like veins and ferritin containing basal ganglia. Therefore, a trade-off needs to be found between a long echo time that visualises more and larger microbleeds and a short echo time that suppresses overlap from other structures with a high susceptibility and gives more SNR.

Recently, a method was introduced which uses T2*-weighted imaging using two echo times. This method was designed for simultaneous angiography and venography.[24] However, the use of two echo times may also be useful for the visualization of microbleeds. Therefore, the purpose of this study was to evaluate the visualization of cerebral microbleeds with T2*-weighted imaging using two echo times at 7 Tesla MR.

Methods

Participants

For this study we included 10 consecutive participants from the Second Manifestations of ARTerial disease (SMART) study. In the SMART study all eligible patients, aged 18 to 79 years, newly referred to our hospital with symptomatic atherosclerotic disease or risk factors for atherosclerosis, are included. The objectives of the SMART study are to determine the prevalence of vascular risk factors and concomitant arterial disease and to study the incidence of future cardiovascular events and its predictors in these high-risk patients.[25] The SMART study and the 7 Tesla imaging were approved by the medical ethics committee. Written informed consent was given by all participants.

The participants were 8 men and 2 women, with a mean age of 54 years (standard deviation (SD) 12 years). Six of the ten participants were included in the SMART-study with vascular risk factors (five diabetes mellitus, one family history of vascular disease), two participants with a stroke, one participant with angina pectoris, and one participant with peripheral artery disease.

MR Imaging

MR imaging was performed with a 7 Tesla whole-body system (Philips Healthcare, Cleveland, OH, USA), using a volume transmit and 16-channel receive head coil (Nova Medical, Wilmington, MA, USA). In all participants, a dual echo T2*-weighted sequence was used with an acquired resolution of 0.35 x 0.4 x 0.6 mm^3. The dual echo sequence that we investigated for the detection of microbleeds was originally designed for simultaneous arterial and venous angiography and therefore the first echo was optimized as much as possible for angiography and the second echo for venography. The echo time for the first echo was 2.5 ms for angiography and for the echo time for the second echo was 15.0 ms for venography. These echo times were chosen to obtain a good balance between good background suppression for the angiogram and enough sensitivity (T2*-weighting) and SNR for the venogram. The other imaging parameters were: repetition time 20 ms, and acquired matrix of 508 x 399 with 167 slices. Excitation pulses consisted of non-saturated excitation pulses with nominal flip angle variation of 16 to 24 degrees in the feet–head direction over the slab. Flow compensation was applied in three directions. For the first echo a partial echo readout was used, for the second echo a full echo readout. A fly-back gradient was applied between the two readouts. Sensitivity encoding was applied in the RL direction with an acceleration factor of 2.5. The images were reconstructed to 0.35 x 0.35 x 0.3 mm^3 voxels, and the built-in phase correction, partial-echo filter and homogeneity correction of the MR system were applied during reconstruction. The imaging duration was approximately 8 minutes and 50 seconds. Because of ongoing development at 7 Tesla MR, some scans were acquired with a slightly different resolution.

Post-processing

The post-processing of the data was performed on the standard console. Minimum intensity projections (minIPs) were reconstructed for transversal slabs (thickness 3 mm, 2 mm overlap, 150 slices) of the first echo and the second echo. To visualise the arteries, a maximum intensity projection (MIP) was reconstructed for transversal slabs (thickness 20 mm, 18 mm overlap, 50 slices) of the first echo. A summation was made of the resulting MIP image with a minIP (thickness 10 mm, 8 mm overlap, 50 slices) of the first echo image, to visualise the relation between arteries and microbleeds.

Rating of microbleeds

Microbleeds were defined as round or ovoid black lesions on the first and/or the second echo of the T2*-weighted scan. Symmetrical areas of calcification in the basal ganglia, choroid plexus and pineal gland were excluded, as were signal voids caused by sulcal vessels and low-signal lesions thought to be signal averaging from adjacent bone.[3,15]

The minIP images of the first and second echo were linked and analyzed simultaneously. Presence of microbleeds was analyzed on the first and second echo image by one observer. Intensity profiles of the microbleeds on the first and/or second echo were obtained, as illustrated in figure 1. The software program Matlab (v. 7.6, MathWorks, Natick, MA) was used to calculate the full-width-at-half-minimum (FWHM) of the profiles. We took the FWHM as an estimate of the diameter of the microbleeds as they appeared in the images.

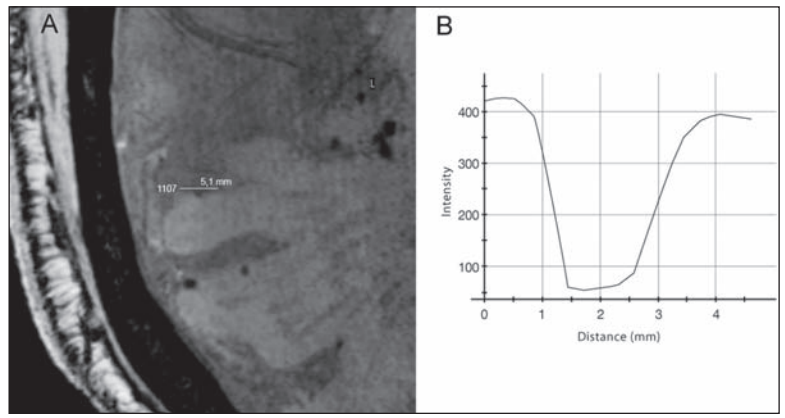

Figure 1 |
[**A**] *A horizontal line is drawn in the midline of the microbleed on a minimal intensity projection of the first echo image to obtain the intensity profile. The corresponding profile is shown in* **B**. *This profile is used to calculate the full-width-at-half-minimum as an estimate for the diameter of the microbleed.*

Statistical analysis

First, the number of microbleeds was calculated for each participant. Second, the difference in diameter between the two echoes was tested with use of the nonparametric Wilcoxon signed ranks test for all microbleeds that were visible on both echoes, as the diameters of the microbleeds were not normally distributed. The correlation between the diameter on the first and second echo was estimated with the Spearman's correlation coefficient. The analysis was performed by using the statistical software package SPSS (version 15.0 for Windows; SPSS Chicago, Ill).

Results

Figure 2 shows an example of the angiography on the MIP of the first echo (figure 2a) and the venography on the minIP of the second echo (figure 2d) with dual echo T2*-weighted imaging at 7 Tesla. A summation of the MIP of the first echo (figure 2a) with the minIP of the first echo (figure 2b) enables to visualise the relation between the arteries and the microbleeds (figure 2c). The minIP of the second echo shows the relation between veins and microbleeds (figure 2d, e).

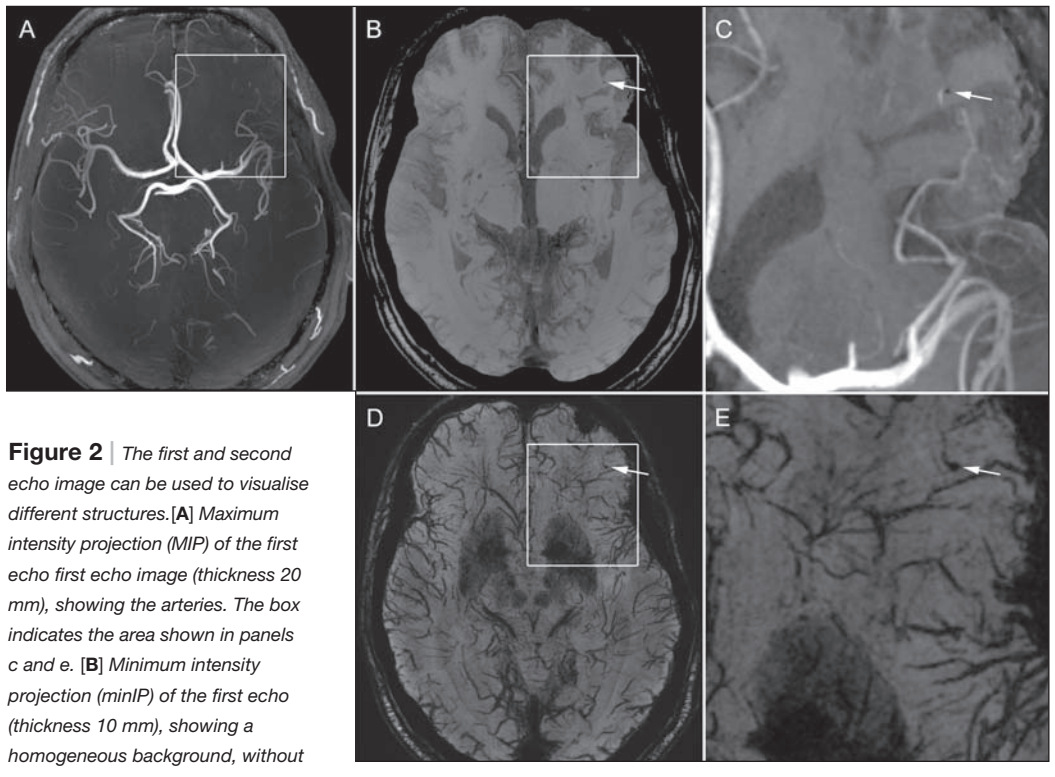

Figure 2 | *The first and second echo image can be used to visualise different structures.*[**A**] *Maximum intensity projection (MIP) of the first echo first echo image (thickness 20 mm), showing the arteries. The box indicates the area shown in panels c and e.* [**B**] *Minimum intensity projection (minIP) of the first echo (thickness 10 mm), showing a homogeneous background, without contrast for veins and basal ganglia. A small microbleed is visible as a round, black lesion (arrow).* [**C**] *A summation of the MIP (a) and the minIP (b) of the first echo enables to visualise the relation between microbleeds and the arteries.* [**D**] *MinIP of the second echo (thickness 10 mm), showing the veins and a small microbleed (arrow).* [**E**] *Magnification of the box in d, showing the relation between the microbleed (arrow) and the veins. Note the lack of signal in the globus pallidus, which makes it difficult to observe potential microbleeds in this area on the second echo.*

The distinction between veins and microbleeds can well be made with use of the minIP of the second echo. The round hypodensities that mimic microbleeds on the source data, turn out to be linear structures on the minIP of the second echo that can be identified as veins. As an example in figure 3a the small area of darkening indicated by the arrow is not a microbleed, which can be clearly seen from the minIP images (figure 3b) which show that this area corresponds with a vein.

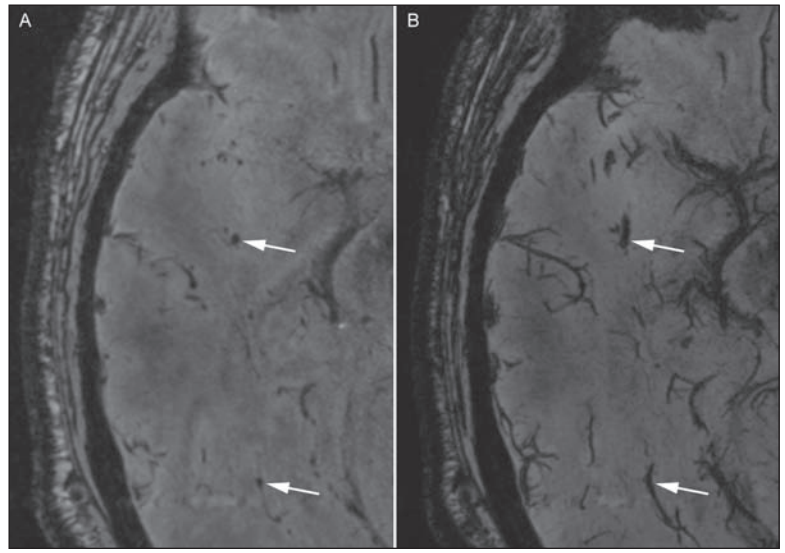

Figure 3 | [**A**] *Several round hypodensities are seen on this source image of the second echo which are suspicious for microbleeds (arrows).* [**B**] *With use of a minimal intensity projection of the second echo image (thickness 3 mm), the hypodensities that were suspicious for microbleeds turn out to be venous structures (arrows).*

Of the 10 participants, microbleeds were found on the first or second echo in 8 participants. In these 8 participants, a total of 104 microbleeds were detected on the first or second echo, with a median of 4 microbleeds (range 1-77). Of these 104 microbleeds, 88 (84.6%) were visible on the first echo. On the second echo 102 (98.0%) microbleeds were visible. Of all the microbleeds that were visible on the second echo, 16 microbleeds were not visible on the first echo (figure 4). In general, these were microbleeds with a small diameter (mean diameter 0.78 mm (SD 0.18 mm) on the second echo). Two microbleeds were only visible on the first echo image, whereas on the second echo image the microbleeds could not be distinguished from surrounding tissue or veins (figure 5). These microbleeds had a diameter of 0.89 mm and 1.48 mm on the first echo.

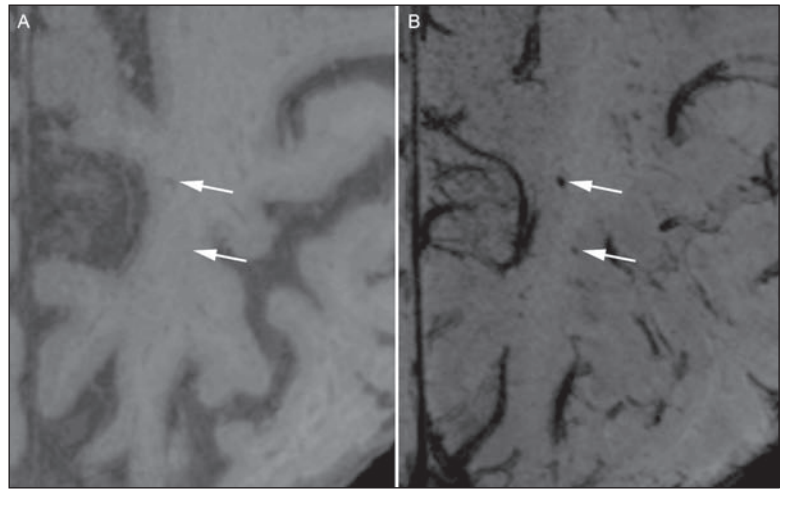

Figure 4 | [**A**] *Shows a minimal intensity projection (minIP) of the first echo image. The microbleed that is visible on the minIP of the second echo image* [**B**]*, is not visible on the first echo image (arrows).*

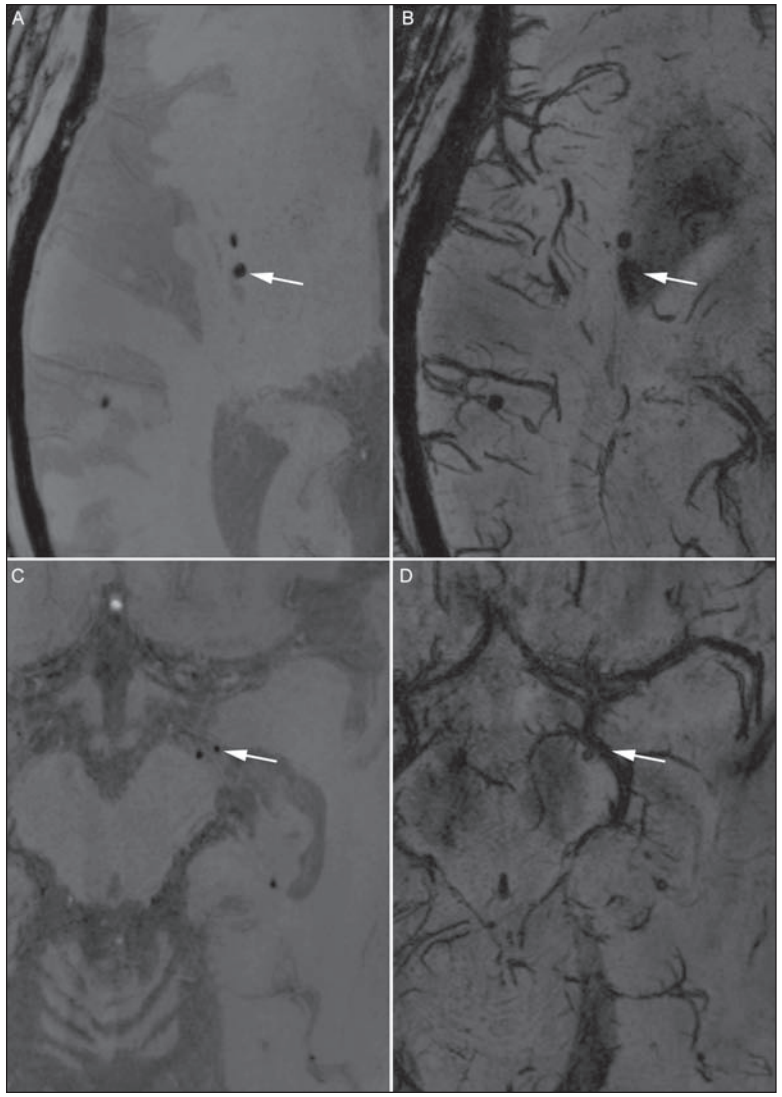

Figure 5 | [**A**] *Shows a microbleed that is clearly visible on the minimal intensity projection (minIP) of the first echo image (arrow). The same microbleed is hardly distinguishable from the ferritin containing putamen on the minIP of the second echo image* [**B, arrow**]. *In* [**C**] *there is a microbleed visible on the minIP of the first echo image, which disappears behind a venous structure on the minIP of the second echo image in* [**D**].

The 86 microbleeds that were visible on both the first and the second echo image, had a mean diameter of 1.24 mm (SD 0.56) on the first echo image and 2.34 mm (SD 1.0) on the second echo. Comparison of the diameters visible on the first and second echo image in all participants, showed that the microbleeds on the second echo were significantly larger than on the first echo image ($p<0.001$). The growth in diameter between the two echo times is illustrated in figure 6. The diameters show a strong linear correlation between the first and second echo time (correlationcoefficient 0.85, $p<0.001$).

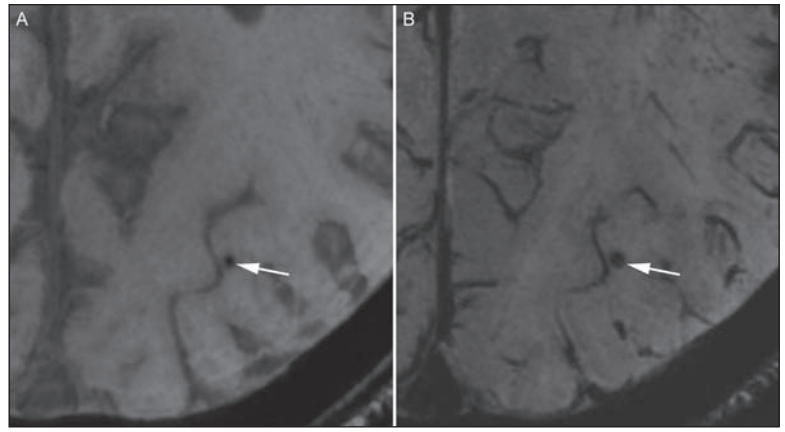

Figure 6 | [**A**] *The microbleed that is visible on minimal intensity projection (minIP) of the first echo image (arrow), appears larger on the minIP of the second echo image* [**B, arrow**].

Discussion

With this study we showed that a short echo time is beneficial to distinguish microbleeds from other structures with a high susceptibility and that with the second echo a larger number of microbleeds can be detected. The advantages of both echo times are combined in the dual echo T2*-weighted imaging at 7 Tesla.

We showed that microbleeds appear larger on the second echo than on the first echo, however, the real size of the microbleeds is not reflected in these images, due to the blooming effect. This is the case in all T2*-weighted or susceptibility weighted images, the real size of the microbleeds can only be obtained with pathology. The increase in diameter explains why many microbleeds can be seen on the second echo image, whereas they are too small to detect on the first echo image. The long echo time gives more time for dephasing, which enlarges the susceptibility effect.[3] This leads to a larger blooming effect and thus a larger diameter of the microbleeds, which is very useful for the detection of the microbleeds. From literature it is known that the observed volume of a microbleed is proportional to the echo time.[26] As the volume is proportional to the third power of the diameter, the increase in volume in our study is $(2.34/1.24)^3 = 6.7$, which corresponds reasonably to the increase in echo time of $15/2.5 = 6$. Another advantage of the second echo image is that the veins are clearly visible. This can provide information about the relation between veins and microbleeds.

However, microbleeds are often found near veins or in the basal ganglia, and, with increasing age, ferritin-bound iron accumulates in the basal ganglia. Because the susceptibility effect of haemosiderin is stronger than that of deoxyhemoglobin and ferritin,[21-23] haemosiderin can already be visualised with a short echo time, whereas deoxyhemoglobin and ferritin are hardly visible on the first echo. With a longer echo time the susceptibility effect of haemosiderin, but also of deoxyhemoglobin and ferritin increases. This helps to detect microbleeds that are located near veins or in the basal ganglia. These microbleeds can be clearly visible on the first echo, but may be obscured by veins and ferritin-containing structures, such as the basal ganglia, on the second echo. Even large microbleeds, which may be clinically relevant, can be obscured by overlapping structures on the second echo and become visible on the first echo image. Besides that, the first echo image shows the dark microbleeds against a homogeneous, more hyperintense signal of the brain tissue, making the detection of microbleeds easier, as the veins and other structures with high susceptibilities different from haemosiderin are less prominent.
Although the first echo image is helpful to distinguish microbleeds from deoxyhemoglobin in veins and ferritin in the basal ganglia, the distinction between microbleeds and calcifications remains difficult. Calcifications also appear as small hypointense foci on both the first and second echo, mimicking microbleeds. The distinction between microbleeds and calcifications can be made by the characteristic location of calcifications (symmetrical

in the basal ganglia, or in the pineal gland or choroid plexus) or by identification of calcifications with use of CT. A recent study showed an additional possibility to distinguish calcifications on MRI with use of phase images.[27] In this study we used the characteristic location of calcifications, which is in line with other studies investigating microbleeds.[3]

The summation of the MIP and the minIP of the first echo image gives an image in which both the arteries and the microbleeds can be visualised. This is useful to analyse the relation between arteries and microbleeds in vivo without use of contrast agents. This is probably a unique feature of dual echo T2*-weighted imaging at ultra-high field strength. The short echo time needed for the visualization of arteries is field strength independent, as this depends on the flow velocity in the arteries. At ultra-high field strength, the susceptibility effect is large enough to visualise microbleeds even at this short echo time. This enables the visualization of both arteries and microbleeds in one image, whereas at lower field strengths, the susceptibility effect may not be large enough to visualise the microbleeds at the first echo time. As it is not known whether the aetiology of microbleeds involves mainly the arteries or the veins of the brain, combining the information of the first echo, visualizing arteries and microbleeds, and second echo, visualizing veins and microbleeds, in one scan may provide more insight the etiologic pathway. Furthermore, the detection of microbleeds with use of the dual echo T2*-weighted scan at 7 Tesla MR can be important for future studies evaluating the prevalence and the prognostic value of microbleeds.
Nowadays, susceptibility weighted imaging (SWI) is increasingly used for the detection of microbleeds.[28-32] In SWI the magnitude and phase images of the T2*-weighted scan are combined to create enhanced contrast between tissues with different susceptibilities.[21] However, SWI depends strongly on the voxel aspect ratio, with an optimal voxel aspect ratio of 1:1:4, while we used more isotropic voxels (aspect ratio of 1:1.3:1.7).[33] The additional value of SWI will be minimal for scans with near isotropic voxels, and we therefore chose T2*-weighted imaging in stead of SWI for the detection of microbleeds in our study at 7 Tesla.

In conclusion, T2*-weighted imaging using two echo times at 7 Tesla combines the advantages of the first and second echo. The first echo utilizes the strong paramagnetic effect of haemosiderin to obtain large contrast between microbleeds and the surrounding tissue on the first echo image, even in the presence of paramagnetic ferritin. The second echo enables visualization of smaller microbleeds than the first echo, as the blooming effect enlarges the observed size of the microbleeds at the second echo image. Furthermore, additional information about the relation between both arteries and microbleeds as well as veins and microbleeds can be obtained from this scan. Visualization of microbleeds and information about their relation with arteries and veins can be useful for future studies investigating the etiology, prevalence or prognostic value of cerebral microbleeds.

References

1 Cordonnier C, van der Flier WM, Sluimer JD, Leys D, Barkhof F, Scheltens P. Prevalence and severity of microbleeds in a memory clinic setting. *Neurology* 2006;66:1356-1360.
2 Fazekas F, Kleinert R, Roob G, Kleinert G, Kapeller P, Schmidt R, Hartung HP. Histopathologic analysis of foci of signal loss on gradient-echo T2*-weighted MR images in patients with spontaneous intracerebral hemorrhage: evidence of microangiopathy-related microbleeds. *AJNR Am J Neuroradiol* 1999;20:637-642.
3 Greenberg SM, Vernooij MW, Cordonnier C, Viswanathan A, Al-Shahi SR, Warach S, Launer LJ, Van Buchem MA, Breteler MM. Cerebral microbleeds: a guide to detection and interpretation. *Lancet Neurol* 2009;8:165-174.
4 Jeong JH, Yoon SJ, Kang SJ, Choi KG, Na DL. Hypertensive pontine microhemorrhage. *Stroke* 2002;33:925-929.
5 Kinoshita T, Okudera T, Tamura H, Ogawa T, Hatazawa J. Assessment of lacunar hemorrhage associated with hypertensive stroke by echo-planar gradient-echo T2*-weighted MRI. *Stroke* 2000;31:1646-1650.
6 Wardlaw JM, Lewis SC, Keir SL, Dennis MS, Shenkin S. Cerebral microbleeds are associated with lacunar stroke defined clinically and radiologically, independently of white matter lesions. *Stroke* 2006;37:2633-2636.
7 Koennecke HC. Cerebral microbleeds on MRI: prevalence, associations, and potential clinical implications. *Neurology* 2006;66:165-171.
8 Vernooij MW, Van der Lugt A, Breteler MM. Risk of thrombolysis-related hemorrhage associated with microbleed presence. *Stroke* 2008;39:e115.
9 Vernooij MW, Heeringa J, de Jong GJ, Van der Lugt A, Breteler MM. Cerebral microbleed preceding symptomatic intracerebral hemorrhage in a stroke-free person. *Neurology* 2009;72:763-765.
10 Nighoghossian N, Hermier M, Adeleine P, Blanc-Lasserre K, Derex L, Honnorat J, Philippeau F, Dugor JF, Froment JC, Trouillas P. Old microbleeds are a potential risk factor for cerebral bleeding after ischemic stroke: a gradient-echo T2*-weighted brain MRI study. *Stroke* 2002;33:735-742.
11 Soo YO, Yang SR, Lam WW, Wong A, Fan YH, Leung HH, Chan AY, Leung C, Leung TW, Wong LK. Risk vs benefit of anti-thrombotic therapy in ischaemic stroke patients with cerebral microbleeds. *J Neurol* 2008;255:1679-1686.
12 Fiehler J, Albers GW, Boulanger JM, Derex L, Gass A, Hjort N, Kim JS, Liebeskind DS, Neumann-Haefelin T, Pedraza S, Rother J, Rothwell P, Rovira A, Schellinger PD, Trenkler J. Bleeding risk analysis in stroke imaging before thromboLysis (BRASIL): pooled analysis of T2*-weighted magnetic resonance imaging data from 570 patients. *Stroke* 2007;38:2738-2744.
13 Werring DJ, Frazer DW, Coward LJ, Losseff NA, Watt H, Cipolotti L, Brown MM, Jager HR. Cognitive dysfunction in patients with cerebral microbleeds on T2*-weighted gradient-echo MRI. *Brain* 2004;127:2265-2275.
14 Henneman WJ, Sluimer JD, Cordonnier C, Baak MM, Scheltens P, Barkhof F, van der Flier WM. MRI biomarkers of vascular damage and atrophy predicting mortality in a memory clinic population. *Stroke* 2009;40:492-298.
15 Jeerakathil T, Wolf PA, Beiser A, Hald JK, Au R, Kase CS, Massaro JM, DeCarli C. Cerebral microbleeds: prevalence and associations with cardiovascular risk factors in the Framingham Study. *Stroke* 2004;35:1831-1835.
16 Vernooij MW, Van der Lugt A, Ikram MA, Wielopolski PA, Niessen WJ, Hofman A, Krestin GP, Breteler MM. Prevalence and risk factors of cerebral microbleeds: the Rotterdam Scan Study. *Neurology* 2008;70:1208-1214.
17 Roob G, Schmidt R, Kapeller P, Lechner A, Hartung HP, Fazekas F. MRI evidence of past cerebral microbleeds in a healthy elderly population. *Neurology* 1999;52:991-994.

18 Haacke EM, Mittal S, Wu Z, Neelavalli J, Cheng YC. Susceptibility-weighted imaging: technical aspects and clinical applications, part 1. *AJNR Am J Neuroradiol* 2009;30:19-30.
19 Tatsumi S, Ayaki T, Shinohara M, Yamamoto T. Type of gradient recalled-echo sequence results in size and number change of cerebral microbleeds. *AJNR Am J Neuroradiol* 2008;29:e13.
20 Wixom RL, Prutkin L, Munro HN. Hemosiderin: nature, formation, and significance. *Int Rev Exp Pathol* 1980;22:193-225.
21 Bradley WG, Jr. MR appearance of hemorrhage in the brain. *Radiology* 1993;189:15-26.
22 Vymazal J, Urgosik D, Bulte JW. Differentiation between hemosiderin- and ferritin-bound brain iron using nuclear magnetic resonance and magnetic resonance imaging. *Cell Mol Biol (Noisy-le-grand)* 2000;46:835-842.
23 Haque TL, Miki Y, Kanagaki M, Takahashi T, Yamamoto A, Konishi J, Nozaki K, Hashimoto N, Konishi J. MR contrast of ferritin and hemosiderin in the brain: comparison among gradient-echo, conventional spin-echo and fast spin-echo sequences. *Eur J Radiol* 2003;48:230-236.
24 Du YP, Jin Z. Simultaneous acquisition of MR angiography and venography (MRAV). *Magn Reson Med* 2008;59:954-958.
25 Simons PC, Algra A, van de Laak MF, Grobbee DE, van der Graaf Y. Second manifestations of ARTerial disease (SMART) study: rationale and design. *Eur J Epidemiol* 1999;15:773-781.
26 Bos C, Viergever MA, Bakker CJ. On the artifact of a subvoxel susceptibility deviation in spoiled gradient-echo imaging. *Magn Reson Med* 2003;50:400-404.
27 Wu Z, Mittal S, Kish K, Yu Y, Hu J, Haacke EM. Identification of calcification with MRI using susceptibility-weighted imaging: a case study. *J Magn Reson Imaging* 2009;29:177-182.
28 Akter M, Hirai T, Hiai Y, Kitajima M, Komi M, Murakami R, Fukuoka H, Sasao A, Toya R, Haacke EM, Takahashi M, Hirano T, Kai Y, Morioka M, Hamasaki K, Kuratsu J, Yamashita Y. Detection of hemorrhagic hypointense foci in the brain on susceptibility-weighted imaging clinical and phantom studies. *Acad Radiol* 2007;14:1011-1019.
29 Kirsch W, McAuley G, Holshouser B, Petersen F, Ayaz M, Vinters HV, Dickson C, Haacke EM, Britt IW, Larsen J, Kim I, Mueller C, Schrag M, Kido D. Serial Susceptibility Weighted MRI Measures Brain Iron and Microbleeds in Dementia. *J Alzheimers Dis* 2009.
30 Mori N, Miki Y, Kikuta K, Fushimi Y, Okada T, Urayama S, Sawamoto N, Fukuyama H, Hashimoto N, Togashi K. Microbleeds in moyamoya disease: susceptibility-weighted imaging versus T2*-weighted imaging at 3 Tesla. *Invest Radiol* 2008;43:574-579.
31 Nandigam RN, Viswanathan A, Delgado P, Skehan ME, Smith EE, Rosand J, Greenberg SM, Dickerson BC. MR imaging detection of cerebral microbleeds: effect of susceptibility-weighted imaging, section thickness, and field strength. *AJNR Am J Neuroradiol* 2009;30:338-343.
32 Santhosh K, Kesavadas C, Thomas B, Gupta AK, Thamburaj K, Kapilamoorthy TR. Susceptibility weighted imaging: a new tool in magnetic resonance imaging of stroke. *Clin Radiol* 2009;64:74-83.
33 Xu Y, Haacke EM. The role of voxel aspect ratio in determining apparent vascular phase behavior in susceptibility weighted imaging. *Magn Reson Imaging* 2006;24:155-160.

Chapter 04 Visualization of cerebral microbleeds with dual echo T2*-weighted MR imaging at 7 Tesla

CHAPTER 05

Cerebral microbleeds on MRI: comparison between 1.5 and 7 Tesla

Mandy M.A. Conijn
Mirjam I. Geerlings
Geert-Jan Biessels
Taro Takahara
Theo D. Witkamp
Jaco J.M. Zwanenburg
Peter R. Luijten
Jeroen Hendrikse

Abstract

Background and Purpose

The detection of microbleeds differs strongly between studies, due to differences in scan protocol. This study aims to compare the visualization of microbleeds with 3D T2*-weighted imaging at 1.5T with 3D dual-echo T2*-weighted imaging at 7T.

Methods

Thirty-four patients (29 male, mean age 58 ± 12 years) with atherosclerotic disease from the Second Manifestations of ARTerial disease (SMART) study were included. 3D T2*-weighted imaging at 1.5T and dual echo T2*-weighted imaging at 7T were done in all patients. Presence and number of definite microbleeds were recorded on minimal intensity projections. Inter- and intra-observer reliability were assessed with Cohen κ test and the intraclass correlation coefficient (ICC). The difference in presence and number of microbleeds was tested with McNemar's test and Wilcoxon signed rank test.

Results

The inter-observer ICC at 7T was 0.61 and the intra-observer ICC was 0.94, whereas at 1.5T the inter-observer ICC was 0.50 and the intra-observer ICC 0.59. Microbleeds were detected in significantly more patients on 7T (50%) than on 1.5T scans (21%) (p=0.001). The number of microbleeds was also higher at 7T (median 0.5, range 0-5) than on 1.5T (median 0.0, range 0-6) (p=0.002).

Conclusion

3D dual echo T2*-weighted imaging at 7T results in better and more reliable detection of microbleeds compared to 3D T2*-weighted imaging at 1.5T.

Introduction

Recent studies show that cerebral microbleeds are commonly detected on MRI in the general population as well as in specific patient populations, such as patients with cerebral small vessel disease, moyamoya disease and other neurologic pathology.[1-8] At the same time, the evidence about the clinical relevance of microbleeds increases. Cerebral microbleeds appear to be direct markers of vascular disease, as they are associated with hypertensive vasculopathy, cerebral amyloid angiopathy, and also with white matter lesions and lacunar infarcts.[1, 8-10] Although still under debate, the presence of microbleeds could be of importance in patients with ischemic stroke receiving anticoagulation, as it might indicate a higher risk of future intracerebral haemorrhage.[11-15] Furthermore, some studies have shown that microbleeds are associated with cognitive impairment, functional dependence or death.[10,16,17]

The number of microbleeds detected differs strongly between studies, even between studies with similar study populations. In population-based studies, for example, prevalences range from 5% to 23%.[3,7] Differences in lesion prevalence are probably not only related to the characteristics of the different study populations, but also to differences in the MR protocol such as differences in scantechnique, repetition time (TR), echo time (TE), flip angle, band width, slice thickness and spatial resolution.[18,19]

Microbleeds are paramagnetic, which induces a susceptibility effect on the MRI scan. This leads to a fast decay of local T2*-weighted MRI signal because of a local inhomogeneity of the field induced by the microbleeds. This makes T2*-weighted gradient-recalled echo (GRE) very sensitive to microbleeds.[9,10,20] One of the factors in the imaging protocol that influences the visualization of microbleeds is the echo time. A longer TE gives more time for dephasing, which enhances the susceptibility effect. This so-called blooming effect causes the microbleeds to appear as hypointense spots that are larger than the actual size. It has been shown that prolonging the TE leads to an increase in diameter of these lesions and also detection of an increased number of microbleeds.[21] However, microbleeds can also be obscured by overlapping structures with a high susceptibility effect, like veins (deoxyhemoglobin) or the basal ganglia (ferritin deposition). With a longer TE, these structures will also increase in size, making it harder to distinguish the microbleeds. Therefore, both a short TE and a long TE may have benefits for the visualization of microbleeds. Besides the TE, also the spatial resolution is important for the visualization of microbleeds. With a higher resolution, partial volume effects will be minimized and smaller microbleeds can be visualized.[22] Another factor that influences the visualization of microbleeds is magnetic field strength. Up till now, most studies investigating microbleeds used a 1.5T MRI scanner. However, studies comparing 1.5T and 3T show a higher number of microbleeds at 3T.[18,23] As the susceptibility effect scales with the magnetic field, scanning at higher field strengths improves the sensitivity to microbleeds. At ultra-high field strengths, such as 7T, the susceptibility effect will further increase as will the signal to noise ratio (SNR). This increase in SNR can be used for higher spatial resolution with increased conspicuity of small haemosiderin deposits that may be obscured by partial volume effects at lower field strengths operating at lower spatial resolution.[24] Furthermore, scanning at ultra-high field strengths enables the use of dual echo T2*-weighted imaging for the visualization of microbleeds, whereas at lower field strengths this is probably not feasible as the susceptibility effect may not be large enough to visualize the microbleeds at the short echo times. The use of a dual echo sequence at 7T has been shown to combine the benefits of a short TE and a long TE for the visualisation of microbleeds in one sequence.[25] It has not been established whether the use of a dual echo sequence at 7T increases the number of detected microbleeds compared to the commonly used single echo T2*-weigthed imaging at lower field strengths. The purpose of our study was to compare the visualization of microbleeds with T2*-weighted imaging on 1.5T with dual echo T2*-weighted imaging at 7T and assess the reliability of the detection of microbleeds with the two field strengths.

Methods

Patients

Patients from the Second Manifestations of ARTerial disease (SMART) study,[26] without contraindications for 7T MRI, were consecutively included between July 2008 and December 2009. The objectives of the SMART study are to determine the prevalence of vascular risk factors and concomitant arterial disease and to study the incidence of future cardiovascular events and its predictors in patients newly referred to our hospital with atherosclerotic disease. The SMART study and the 7T imaging were approved by the medical ethics committee. Written informed consent was given by all patients. In total, 38 patients could be included in our study. The scans of three patients were used for a training session of the two observers and therefore excluded from the final analysis. In one patient more than 20 microbleeds were seen on the 7T scan. This was considerably more than in all other patients; the sum of all microbleeds in the remaining 34 patients on the 7T scan was 36. To prevent that the results depended highly on the scan of this single patient with many microbleeds, this patient was considered as an outlier and excluded from the analysis. Therefore the analysis was done on 34 patients.

MR Imaging

MR imaging was performed at a 1.5T whole-body system (Gyroscan ACS-NT, Philips Medical Systems, Best, the Netherlands) and a 7T whole-body system (Philips Healthcare, Cleveland, OH, USA). In all patients, a 3D T2*-weighted imaging scan at 1.5T MRI and a 3D dual echo T2*-weighted MRI scan at 7T MRI were performed on the same day (MR sequence parameters shown in table 1).

As the dual echo sequence at 7T was originally designed as combination of an arteriogram and a venogram, the first echo (TE1) was used to make an inflow arteriogram. To control for intra-voxel dephasing of flowing blood, the TE1 had to be short, with full flow compensation and partial Fourier encoding. The fat had to be suppressed and therefore water and fat should be out of phase. For 7T this is possible at 0.5 ms, 1.5 ms, 2.5 ms, and so on. The minimal TE depends on the resolution and the gradient power and in our case 2.5 ms is the optimum. Therefore, the TE1 was chosen at 2.5 ms.

The second echo (TE2) was designed to make a venogram. Therefore, it was important to have a full echo and a flyback gradient, so the second readout gradient had the same polarity as the first readout gradient.[27] To obtain enough sensitivity, the echo time had to be relatively long, preferably between 20 and 30 ms. A longer echo time was not useful because the SNR would become too low. For the choice of the TE2, it is important that the repetition time is short enough to obtain good background suppression on the first echo image (arteriogram). The flip angle was optimized for angiography in the first echo and for venography in the second echo. Excitation pulses consisted of tilt-optimised non-saturated excitation (TONE) pulses with nominal flip angle variation of 16°-24° in the feet–head direction. With this flip angle the repetition time had to be around 20 ms.[28] Here a balance had to be found between a long enough echo time for the venogram and a short enough repetition time for good background suppression in the arteriogram. As a compromise, the TE2 was chosen at 15 ms.

The parameters of the T2*-weighted imaging at 1.5T were chosen to be comparable to the 7T scan within the possibilities of the 1.5T MRI. Therefore a scan with a high spatial resolution was made, with an acquired voxel size of 0.8 x 0.8 x 0.8 mm. A PRESTO (principles of echo shifting with a train of observations) technique with a TE of 35 ms and a TR of 25 ms was used. During this sequence, additional field gradients shift the refocused gradient echo into the subsequent TR period, which results in a TE longer than the TR. In this sequence the flip angle is not optimized for maximum SNR with the given TR, but small flip angles are needed to attenuate the contribution of spin echoes and stimulated echoes.[29] With this technique it is possible to obtain a longer echo time with a relatively short repetition time, resulting in a shorter scan time. This makes it possible to obtain a high resolution scan with a long TE within a reasonable scan time. The use of PRESTO has been shown to result in a higher contrast-to-noise ratio compared to 3D-GRE for the visualization of microbleeds.[30]

Table 1 **MR sequence parameters**

Sequence parameter	1.5 Tesla	7 Tesla
Repetition time (msec)	25	20.0
Echo time (msec)	35	2.5 / 15.0
Flip angle (degrees)	10	16-24 (variation over slab)
Bandwidth (Hz/pixel)	100	203
Matrix size	276 x 226	508 x 399
Parallel imaging	Yes (acceleration factor = 1.8)	Yes (acceleration factor = 2.5)
Flow compensation	No	Yes
Section thickness (mm)	0.8	0.6
Gap (mm)	None	None
No. of sections	125	167
Acquired voxel size (mm)	0.8 x 0.8 x 0.8	0.35 x 0.4 x 0.6
Interpolated voxel size (mm)	0.43 x 0.43 x 0.4	0.35 x 0.35 x 0.3
Acquisition time	6 min 56 sec	8 min 50 sec

Post-processing

The post-processing of the data was performed on the console of the MRI system. Minimum intensity projections (minIPs) were reconstructed for transversal slabs (thickness 3 mm, 2 mm overlap, 100 slices) for the 1.5T scan and for the first echo and the second echo of the 7T scan (figure 1).

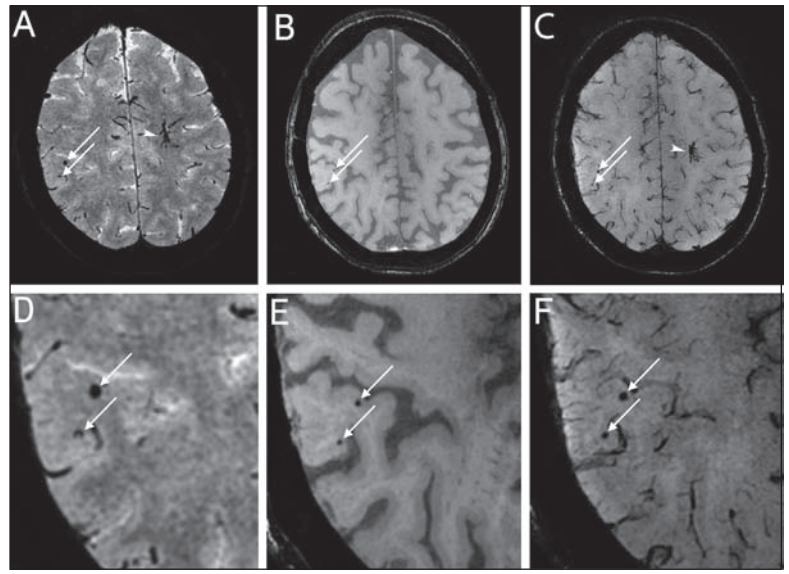

Figure 1 | [**A**] *Minimum intensity projection (minIP) of 3mm thickness of the 1.5T scan. Two microbleeds are visible (arrows).* [**B**] *Shows the minIP of 3mm of the first echo image at 7T, and of the second echo image* [**C**]. *The two microbleeds are also visible on the first and second echo image (arrows). Note the developmental venous anomaly visible on the 1.5T scan (arrowhead) and very clearly demarcated on the second echo of the 7T scan.* [**D-F**] *Magnifications of the microbleeds on the 1.5T scan, the first echo of the 7T scan and the second echo of the 7T scan, respectively.*

Rating of microbleeds

All 1.5T and 7T scans were independently scored by two observers, both experienced neuroradiologists. The observers were trained in one session where they together evaluated scans of three patients with microbleeds. These three patients were excluded from the statistical analysis. For the 7T scans, first and second echo images were both used to score the microbleeds. The observers were blinded to the scan on the other field strength and to all clinical information. The scans of 10 patients were scored twice by one of the observers with a gap of one week to assess intra-observer reliability. The scans that were scored differently by the two observers were evaluated in a consensus meeting to obtain a final score.

1.5T and 7T scans were evaluated in a random order. There was a minimal gap of one week between the evaluation of a 1.5T and 7T scan of the same patient. The rating of the microbleeds was based on the Microbleed Anatomical Rating Scale (MARS).[31] In this rating scale, microbleeds are scored as 'definite' or 'possible' microbleeds. In our study, we focused on 'definite' microbleeds, that were scored when they were visible on the first echo or on the second echo or on both echo images at 7T. Definite microbleeds are defined as small, rounded or circular, well-defined hypointense lesions within brain parenchyma with clear margins ranging from 2 to 10 mm in size on GRE T2*-weighted images in the MARS. In this study we slightly adjusted this definition by excluding the size-criterion. Due to the blooming effect, microbleeds appear larger on GRE T2*-weighted scan than the actual size of the microbleeds. The blooming effect depends among others on the field strength and the echo time, and will therefore be different for the 1.5T and 7T scan, which will result in different sizes for the same microbleeds on the two field strengths. This makes the size-criterion not appropriate for this comparison study. Symmetrical areas of calcification in the basal ganglia, choroid plexus and pineal gland were excluded, as were signal voids caused by sulcal vessels and low-signal lesions thought to be signal voids due to adjacent bone.[3,10,31] Afterwards, dissimilarities between the 1.5T and the 7T scans were assessed in a side-by-side comparison.

Statistical analysis

Inter- and intra-observer reliability for the presence and absence of microbleeds was tested with Cohen κ test. The κ-statistic was interpreted as poor (0-0.20), fair (0.21-0.40), moderate (0.41-0.60), good (0.61-0.80), or very good (0.8-1).[32] The reliability of the number of microbleeds was quantified by the intraclass correlation coefficient (ICC). The difference in prevalence of microbleeds between 1.5T and 7T scans was tested with McNemar's test. For the analysis of the difference in number of visible microbleeds between 1.5T and 7T scans the Wilcoxon signed rank test was used. This analysis was done for all patients and for a selection of patients whose scans showed microbleeds at both field strengths. The analyses were performed by using the statistical software package SPSS (version 15.0 for Windows; SPSS Chicago, Ill).

Results

Baseline characteristics of the 34 patients are shown in table 2.

Table 2 Baseline characteristics of all patients

	All patients (n = 34)
Age (years)*	58 ± 12
Male gender (%)	85
Inclusion in SMART-study with:	
Vascular risk factors (%)	50
Cerebrovascular disease (%)	26
Peripheral artery disease (%)	15
Cardiovascular disease (%)	9

**Age was expressed as mean with standard deviation*

Inter- and intra-observer reliability

Table 3 shows the number of patients with and without definite microbleeds scored by both raters on 1.5T, resulting in a fair inter-observer reliability (κ = 0.30). At 7T the inter-observer reliability for definite microbleeds was moderate (κ = 0.42) (table 4). The intra-observer reliability was moderate at 1.5T (κ = 0.52) and good at 7T (κ = 0.80). For the number of microbleeds moderate inter-observer reliability was demonstrated for the 1.5T (ICC = 0.50) and good reliability for the 7T (ICC = 0.61). The intra-observer reliability for the number of microbleeds was moderate at 1.5T (ICC = 0.59) and very good at 7T (ICC = 0.94).

Table 3 Number of patients with visible microbleeds at 1.5T for the two observers

1.5T	Observer 2		
	Microbleeds absent	Microbleeds present	Total
Observer 1			
Microbleeds absent	21	6	27
Microbleeds present	3	4	7
Total	24	10	34

Table 4 Number of patients with visible microbleeds at 7T for the two observers

7T	Observer 2		
	Microbleeds absent	Microbleeds present	Total
Observer 1			
Microbleeds absent	18	7	25
Microbleeds present	2	7	9
Total	20	14	34

Presence and Number of Microbleeds

Table 5 shows the number of patients with and without microbleeds at 1.5T and 7T after consensus. One or more microbleeds were found on 1.5T scans in 8 (23.5%) patients, and on 7T scans in 17 (50%) patients. The number of patients with microbleeds at 7T was significantly higher than at 1.5T (p = 0.002). There were no patients in whom microbleeds were scored at 1.5T that were not scored at 7T.

Table 5 Number of patients with visible microbleeds at 1.5T and 7T after consensus between the two observers

Consensus 2 observers	7T		
	Microbleeds absent	Microbleeds present	Total
1.5T			
Microbleeds absent	17	9	26
Microbleeds present	0	8	8
Total	17	17	34

In the 8 patients with microbleeds on the 1.5T scans a total of 15 microbleeds was scored (median number of microbleeds 0.0, range 0-6). Of these 15 microbleeds, 7 were located frontal, 3 parietal, 2 occipital, 1 temporal, 1 in the basal ganglia and 1 in the deep and periventricular white matter. In the 17 patients with microbleeds on the 7T scans a total of 36 microbleeds was scored (median 0.5, range 0-5), which was significantly more than at 1.5T (p = 0.003). Of the 36 microbleeds scored on the 7T, 14 were located frontal, 7 parietal, 5 occipital, 5 temporal, 2 in the basal ganglia, 2 in the cerebellum and 1 in the thalamus. In all 8 patients with microbleeds on 1.5T microbleeds were also present on the 7T scan. The median number of microbleeds in these patients with visible microbleeds at both field strengths was 1.0 (range 1-6) at 1.5T, and 2.0 (range 1-5) at 7T. However, this difference was not significant (p = 0.236).

Side-by-Side Comparison

Twenty-seven microbleeds (75%) out of the 36 microbleeds that were scored on 7T scans were not scored on 1.5T scans. Side-by-side comparison of 1.5T and 7T scans showed that 13 (48%) of the microbleeds that were scored at 7T and not on 1.5T were small microbleeds on the 7T scans, which were not visible on the 1.5T scan. Two of these microbleeds were not visible due to overlap of a venous structure. Five other microbleeds (19%) were visible at 1.5T, however, they were located in the vicinity of a venous structure and could therefore not be reliably distinguished as a microbleed. Four microbleeds (15%) were visible as hypointense lesions, but not as a typical well-defined, round shaped lesion, as illustrated in figure 2. As shown in figure 3, three microbleeds (11%) that were not scored on the 1.5T scans were in retrospect visible as very small lesions, which could hardly be distinguished from the background noise. One microbleed (4%) was missed, which was located near the hypointense basal ganglia; on the 7T scan this microbleed was only visible on the first echo image. One other microbleed (4%) was just overlooked by both observers.

Of the total of 15 microbleeds that were scored on 1.5T scans, 5 microbleeds (33%) were not scored on 7T scans. In retrospect, these microbleeds were visible as very small lesions on the 7T scans and were missed by the observers, or defined as no definite microbleed during the consensus meeting. An example of one of those microbleeds is shown in figure 4.

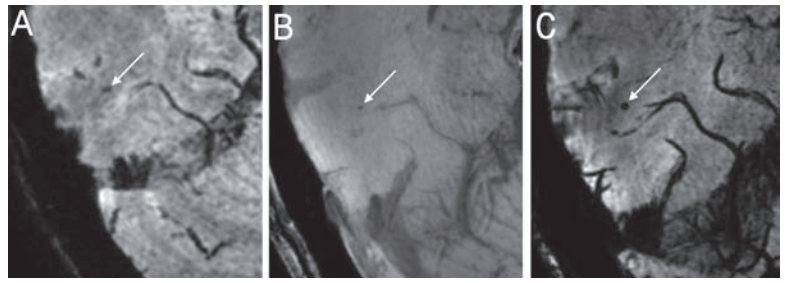

Figure 2 | [**A**] *On this 1.5T scan, a hypointense lesion (arrow) is visible which is not a typical well-defined, round shaped lesion as in the definition of a microbleed. This lesion was not scored as a microbleed on the 1.5T scan. In b and c this same lesion is visible on the 7T scan. On the first echo image* [**B**] *is it is visible as a faint round hypointensity and on the second echo* [**C**] *as a clearly visible round hypointensity (arrow). On the 7T scan both raters scored this lesion as a microbleed.*

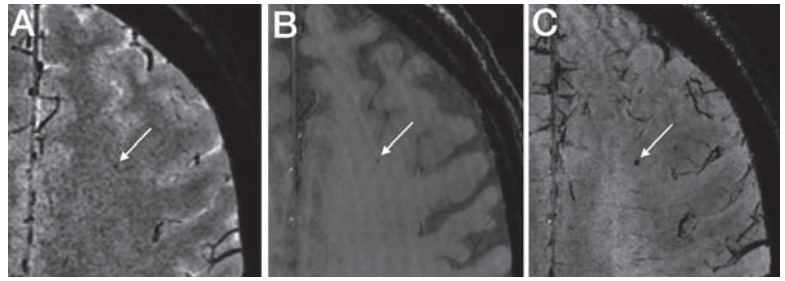

Figure 3 | [**A**] *The 1.5T scan shows a hypointense lesion (arrow) which can hardly be distinguished from noise and was not scored as a microbleed. On both the first echo image* [**B**] *and the second echo image* [**C**] *of the 7T scan this hypointense lesion is visible as a typical microbleed, showing enlargement at the second echo time due to the blooming effect. This lesion was scored as a microbleed by both observers.*

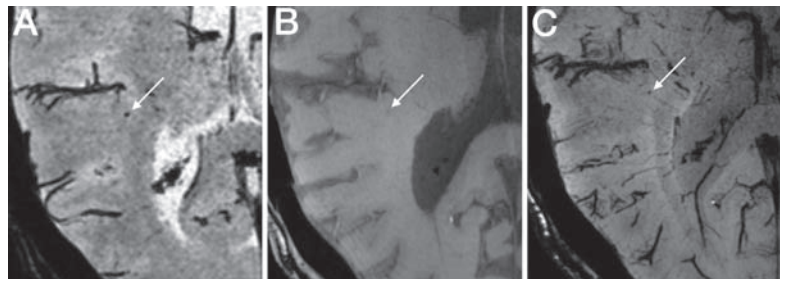

Figure 4 | [**A**] *The 1.5T scan shows a well-defined, round, hypointense lesion (arrow), which was scored as a microbleed. However, on the first echo of the 7T scan* [**B**]*, this lesion is only visible as a very faint hypointensity and on the second echo* [**C**] *it appears as a small microbleed. On the 7T scan this lesion was not scored as a microbleed.*

Discussion

In this study we found a fair to moderate inter- and intra-observer reliability for the presence of microbleeds by using 3D T2*-weighted imaging at 1.5T, and moderate to good reliability by using dual echo T2*-weighted imaging at 7T. For the number of microbleeds the reliability was better, as it was moderate at 1.5T and good to very good at 7T. Overall, we found an increased reliability for both presence and number of microbleeds at 7T compared with 1.5T. Cerebral microbleeds were detected in more patients at 7T than at 1.5T. Furthermore, the number of microbleeds detected was higher at 7T.

Besides the detection of microbleeds in more patients and a higher number of microbleeds at 7T, also the reliability of the detection improves. Compared to 1.5T both inter- and intra-observer reliability improved at 7T. This might be due to the higher resolution, increased SNR, and the use of the dual echo sequence at 7T. Recently, we showed that the first echo image provides a good contrast of the dark microbleeds against a homogenous, more hyperintense signal of the brain tissue, and that 85% of all microbleeds are visible on the first echo image.[25] If a microbleed is visible on the first echo image and also shows a blooming effect on the second echo, it is more easily classified as a definite microbleed, whereas the 1.5T scan provides only one single echo image of the microbleed. Besides that, the contrast between microbleeds and the background is less on the 1.5T scan and the resolution is slightly lower, making it more difficult to distinguish microbleeds from the background noise and from other hypointense structures compared to the 7T scan. The use of the first echo image at 7T is helpful to distinguish microbleeds from deoxyhemoglobin in veins and ferritin in the basal ganglia, whereas microbleeds can be missed by overlap of veins or the hypointense appearance of ferritin containing basal ganglia on the 1.5T scan or on the second echo of the 7T scan.[25]

Previous studies comparing the detection of microbleeds at 3T and 1.5T found significantly more microbleeds at 3T. In addition, the microbleeds conspicuity improved at 3T.[18,23] These results are in line with our results of a better detection of microbleeds at 7T, indicating that the detection of microbleeds improves with increasing field strength. The higher resolution, higher SNR and increased susceptibility effect at 7T increased the conspicuity of smaller microbleeds. This resulted in the detection of more and smaller microbleeds. However, a drawback is that very small microbleeds were hard to distinguish from background noise, and small microbleeds were easily missed by the observers.

Unexpectedly, some microbleeds were scored at 1.5T, but not at 7T. A possible reason for this is that at 7T more and smaller veins are visible, making it harder to distinguish small microbleeds from small veins. This is illustrated by figure 4, where the microbleed that was missed on the 7T scan was located near a very small vein, and could therefore be mistaken as part of the vein.

Nowadays, susceptibility weighted imaging (SWI) is increasingly used for the detection of microbleeds.[18,33] In SWI the magnitude and phase images of the T2*-weighted scan are combined to create enhanced contrast between tissues with different susceptibilities.[34] However, SWI depends strongly on the voxel aspect ratio, with an optimal voxel aspect ratio of 1:1:4, while we used more isotropic voxels (isotropic voxels at 1.5T and an aspect ratio of 1:1.3:1.7 at 7T).[35] The additional value of SWI will be minimal for scans with (near) isotropic voxels, and we therefore chose T2*-weighted imaging instead of SWI for the detection of microbleeds in our study.

A limitation of the study is the relatively low observer reliability at 1.5T. The study by Gregoire et al describing the MARS shows a very good observer reliability by using MARS at 1.5T.[31] There are several possible explanations for this difference. First, Gregoire et al excluded patients with one definite microbleed from the analysis, which substantially improved their interobserver reliability, whereas we did not exclude patients with only one microbleed. Besides that, in the study of Gregoire et al a slice thickness of 5 mm with a gap of 1.5 mm was used, which is a large difference with our 0.8 mm slices. The use of thin slices results in many more slices and also more small microbleeds will become visible. Those small microbleeds are easily missed by the observers, especially when they have to evaluate many slices, inducing differences between the scores of observers. Furthermore, Gregoire et al did not score microbleeds smaller than 2 mm, whereas we did not use a minimum diameter in our study. In other studies at 1.5T observer reliabilities vary from fair to very good,[3,7,36] probably this is also due to differences in scan parameters and definition of microbleeds.

Another limitation of this study is that the scan parameters of the 1.5T T2*-weighted sequence were different from the 7T dual echo sequence. This makes it difficult to evaluate the net effect of the increased field strength. However, when going to higher field strength, it is not feasible to maintain the same scan parameters. Therefore we tried to optimize both scans as much as possible for the corresponding field strength within a reasonable scan time. The echo time is the parameter that most affects sensitivity in T2*-weighted MRI.[10] The echo time at 1.5T is 35 ms, whereas it is only 15 ms for the second echo image at 7T. A longer echo time gives more time for dephasing, resulting in an increase in diameter of microbleeds and also an increase in the number of microbleeds detected.[19] However, within the dual echo sequence at 7T, a balance had to be found between an echo time, which gives enough dephasing and a short repetition time, which is necessary for good background suppression in the first echo image. Therefore the echo time could not be equally long in the 7T sequence as in the 1.5T sequence. The use of a longer echo time at 7T could result in the detection of more microbleeds. However, as other structures with a high susceptibility, such as veins or iron-deposition in the basal ganglia will also become larger, this may lead to more overlap of microbleeds by these brain structures. Therefore, we think it is important to use two echo times to combine the benefits of a short and a long echo time.

Although interest in cerebral microbleeds has greatly increased, their relevance in clinical practice remains unclear.[37] It is possible that the current studies, which are now mainly done at 1.5T, only detect the tip of the iceberg of all microbleeds present in the brain. Scanning at higher field strengths, such as 7T, might be necessary to improve the detection of microbleeds and the reliability of this detection. As microbleeds can be detected in more patients and also the lesion load can be determined more accurately, this could result in more detailed and consistent information about the clinical significance of microbleeds. Furthermore, microbleeds are regarded as markers of vascular pathology and it can be interesting to study changes in patients with cerebral amyloid angiopathy, hypertensive vasculopathy or Alzheimer's disease.[10] The improved detection of microbleeds at 7T may be useful for follow-up studies with small changes in microbleed load over time. Furthermore, good detection methods for microbleeds are needed for future studies to determine whether microbleeds should affect clinical decision making, to identify their relation with other signs of cerebral small vessel disease, and to describe their independent contribution to cognitive and neurological dysfunction.[10]

In conclusion, we found that presence and number of detected microbleeds is higher and also the reliability of the detection of microbleeds improves with a 3D dual echo T2*-weighted sequence at 7T compared to a 3D T2*-weighted sequence at 1.5T.

Chapter 05 Cerebral microbleeds on MRI: comparison between 1.5 and 7 Tesla

References

1 Cordonnier C, van der Flier WM, Sluimer JD, Leys D, Barkhof F, Scheltens P. Prevalence and severity of microbleeds in a memory clinic setting. *Neurology* 2006;66:1356-1360.

2 Dichgans M, Holtmannspotter M, Herzog J, Peters N, Bergmann M, Yousry TA. Cerebral microbleeds in CADASIL: a gradient-echo magnetic resonance imaging and autopsy study. *Stroke* 2002;33:67-71.

3 Jeerakathil T, Wolf PA, Beiser A, Hald JK, Au R, Kase CS, Massaro JM, DeCarli C. Cerebral microbleeds: prevalence and associations with cardiovascular risk factors in the Framingham Study. *Stroke* 2004;35:1831-1835.

4 Kikuta K, Takagi Y, Nozaki K, Hanakawa T, Okada T, Mikuni N, Miki Y, Fushmi Y, Yamamoto A, Yamada K, Fukuyama H, Hashimoto N. Asymptomatic microbleeds in moyamoya disease: T2*-weighted gradient-echo magnetic resonance imaging study. *J Neurosurg* 2005;102:470-475.

5 Koennecke HC. Cerebral microbleeds on MRI: prevalence, associations, and potential clinical implications. *Neurology* 2006;66:165-171.

6 Mori N, Miki Y, Kikuta K, Fushimi Y, Okada T, Urayama S, Sawamoto N, Fukuyama H, Hashimoto N, Togashi K. Microbleeds in moyamoya disease: susceptibility-weighted imaging versus T2*-weighted imaging at 3 Tesla. *Invest Radiol* 2008;43:574-579.

7 Vernooij MW, Van der Lugt A, Ikram MA, Wielopolski PA, Niessen WJ, Hofman A, Krestin GP, Breteler MM. Prevalence and risk factors of cerebral microbleeds: the Rotterdam Scan Study. *Neurology* 2008;70:1208-1214.

8 Wardlaw JM, Lewis SC, Keir SL, Dennis MS, Shenkin S. Cerebral microbleeds are associated with lacunar stroke defined clinically and radiologically, independently of white matter lesions. *Stroke* 2006;37:2633-2636.

9 Fazekas F, Kleinert R, Roob G, Kleinert G, Kapeller P, Schmidt R, Hartung HP. Histopathologic analysis of foci of signal loss on gradient-echo T2*-weighted MR images in patients with spontaneous intracerebral hemorrhage: evidence of microangiopathy-related microbleeds. *AJNR Am J Neuroradiol* 1999;20:637-642.

10 Greenberg SM, Vernooij MW, Cordonnier C, Viswanathan A, Al-Shahi SR, Warach S, Launer LJ, Van Buchem MA, Breteler MM. Cerebral microbleeds: a guide to detection and interpretation. *Lancet Neurol* 2009;8:165-174.

11 Fiehler J, Albers GW, Boulanger JM, Derex L, Gass A, Hjort N, Kim JS, Liebeskind DS, Neumann-Haefelin T, Pedraza S, Rother J, Rothwell P, Rovira A, Schellinger PD, Trenkler J. Bleeding risk analysis in stroke imaging before thromboLysis (BRASIL): pooled analysis of T2*-weighted magnetic resonance imaging data from 570 patients. *Stroke* 2007;38:2738-2744.

12 Gregoire SM, Jager HR, Yousry TA, Kallis C, Brown MM, Werring DJ. Brain microbleeds as a potential risk factor for antiplatelet-related intracerebral haemorrhage: hospital-based, case-control study. *J Neurol Neurosurg Psychiatry* 2010;81:679-684.

13 Soo YO, Yang SR, Lam WW, Wong A, Fan YH, Leung HH, Chan AY, Leung C, Leung TW, Wong LK. Risk vs benefit of anti-thrombotic therapy in ischaemic stroke patients with cerebral microbleeds. *J Neurol* 2008;255:1679-1686.

14 Vernooij MW, Van der Lugt A, Breteler MM. Risk of thrombolysis-related hemorrhage associated with microbleed presence. *Stroke* 2008;39:e115.

15 Vernooij MW, Heeringa J, de Jong GJ, Van der Lugt A, Breteler MM. Cerebral microbleed preceding symptomatic intracerebral hemorrhage in a stroke-free person. *Neurology* 2009;72:763-765.

16 Henneman WJ, Sluimer JD, Cordonnier C, Baak MM, Scheltens P, Barkhof F, van der Flier WM. MRI biomarkers of vascular damage and atrophy predicting mortality in a memory clinic population. *Stroke* 2009;40:492-498.

17 Werring DJ, Frazer DW, Coward LJ, Losseff NA, Watt H, Cipolotti L, Brown MM, Jager HR. Cognitive dysfunction in patients with cerebral microbleeds on T2*-weighted gradient-echo MRI. *Brain* 2004;127:2265-2275.

18 Nandigam RN, Viswanathan A, Delgado P, Skehan ME, Smith EE, Rosand J, Greenberg SM, Dickerson BC. MR imaging detection of cerebral microbleeds: effect of susceptibility-weighted imaging, section thickness, and field strength. *AJNR Am J Neuroradiol* 2009;30:338-343.

19 Vernooij MW, Ikram MA, Wielopolski PA, Krestin GP, Breteler MM, Van der Lugt A. Cerebral microbleeds: accelerated 3D T2*-weighted GRE MR imaging versus conventional 2D T2*-weighted GRE MR imaging for detection. *Radiology* 2008;248:272-277.

20 Roob G, Schmidt R, Kapeller P, Lechner A, Hartung HP, Fazekas F. MRI evidence of past cerebral microbleeds in a healthy elderly population. *Neurology* 1999;52:991-994.

21 Tatsumi S, Ayaki T, Shinohara M, Yamamoto T. Type of gradient recalled-echo sequence results in size and number change of cerebral microbleeds. *AJNR Am J Neuroradiol* 2008;29:e13.

22 Reichenbach JR, Venkatesan R, Yablonskiy DA, Thompson MR, Lai S, Haacke EM. Theory and application of static field inhomogeneity effects in gradient-echo imaging. *J Magn Reson Imaging* 1997;7:266-279.

23 Stehling C, Wersching H, Kloska SP, Kirchhof P, Ring J, Nassenstein I, Allkemper T, Knecht S, Bachmann R, Heindel W. Detection of asymptomatic cerebral microbleeds: a comparative study at 1.5 and 3.0 T. *Acad Radiol* 2008;15:895-900.

24 Haacke EM, Mittal S, Wu Z, Neelavalli J, Cheng YC. Susceptibility-weighted imaging: technical aspects and clinical applications, part 1. *AJNR Am J Neuroradiol* 2009;30:19-30.

25 Conijn MM, Geerlings MI, Luijten PR, Zwanenburg JJ, Visser F, Biessels GJ, Hendrikse J. Visualization of cerebral microbleeds with dual-echo T2*-weighted magnetic resonance imaging at 7.0 T. *J Magn Reson Imaging* 2010;32:52-59.

26 Simons PC, Algra A, van de Laak MF, Grobbee DE, van der Graaf Y. Second manifestations of ARTerial disease (SMART) study: rationale and design. *Eur J Epidemiol* 1999;15:773-781.

27 Du YP, Jin Z. Simultaneous acquisition of MR angiography and venography (MRAV). *Magn Reson Med* 2008;59:954-958.

28 Hendrikse J, Zwanenburg JJ, Visser F, Takahara T, Luijten P. Noninvasive depiction of the lenticulostriate arteries with time-of-flight MR angiography at 7.0 T. *Cerebrovasc Dis* 2008;26:624-629.

29 Liu G, Sobering G, Duyn J, Moonen CT. A functional MRI technique combining principles of echo-shifting with a train of observations (PRESTO). *Magn Reson Med* 1993;30:764-768.

30 Tsuboyama T, Imaoka I, Shimono T, Nakatsuka T, Ashikaga R, Okuaki T, Koyama N, Murakami T. T2* sensitized high-resolution magnetic resonance venography using 3D-PRESTO technique. *Magn Reson Med Sci* 2008;7:73-77.

31 Gregoire SM, Chaudhary UJ, Brown MM, Yousry TA, Kallis C, Jager HR, Werring DJ. The Microbleed Anatomical Rating Scale (MARS): reliability of a tool to map brain microbleeds. *Neurology* 2009;73:1759-1766.

32 Landis JR, Koch GG. The measurement of observer agreement for categorical data. *Biometrics* 1977;33:159-174.

33 Kirsch W, McAuley G, Holshouser B, Petersen F, Ayaz M, Vinters HV, Dickson C, Haacke EM, Britt IW, Larsen J, Kim I, Mueller C, Schrag M, Kido D. Serial Susceptibility Weighted MRI Measures Brain Iron and Microbleeds in Dementia. *J Alzheimers Dis* 2009.

34 Bradley WG, Jr. MR appearance of hemorrhage in the brain. *Radiology* 1993;189:15-26.

35 Xu Y, Haacke EM. The role of voxel aspect ratio in determining apparent vascular phase behavior in susceptibility weighted imaging. *Magn Reson Imaging* 2006;24:155-160.

36 Cordonnier C, Potter GM, Jackson CA, Doubal F, Keir S, Sudlow CL, Wardlaw JM, Al-Shahi SR. improving interrater agreement about brain microbleeds: development of the Brain Observer MicroBleed Scale (BOMBS). *Stroke* 2009;40:94-99.

37 Cordonnier C. Brain microbleeds. *Pract Neurol* 2010;10:94-100.

CHAPTER 06

Iron deposition in basal ganglia at 7T: determinants and relation with cerebral small vessel disease

Mandy M.A. Conijn
Jeroen Hendrikse
Daniël Polders
Hendrik de Leeuw
Raoul P. Kloppenborg
Willem P.Th.M. Mali
Peter R. Luijten
Mirjam I. Geerlings

Abstract

Background and Purpose

Determinants of iron deposition in the brain are largely unknown. We assessed whether age, sex, vascular risk factors, lacunar infarcts, white matter lesions (WML) and microbleeds on MRI were associated with a decrease in T2* of the basal ganglia at 7 Tesla.

Methods

Dual echo T2*-weighted scans at 7T with anatomical scans at 1.5T were available in 49 patients from the Second Manifestations of ARTerial disease (SMART) study. Visual scoring of lacunar infarcts and volumetric assessment of WML were performed on 1.5T scans. The dual echo T2*-weighted scans at 7T were used to score the microbleeds and to measure T2*-values of the putamen, globus pallidus and caudate nucleus.

Results

Older age was significantly associated with lower T2* of the putamen and caudate nucleus, while men had lower T2* of the globus pallidus. Vascular risk factors were not associated with T2*. Lacunar infarcts, but not WML or microbleeds, were associated with significantly lower T2* of the caudate nucleus after adjusting for age and sex. Phase images confirmed iron deposition in the basal ganglia.

Conclusion

Older age, male sex and presence of lacunar infarcts were associated with increased iron deposition in one or more basal ganglia measured with T2* at 7T.

Chapter 06 Iron deposition in basal ganglia at 7T: determinants and relation with cerebral small vessel disease

Introduction

Iron is important for metabolic processes of the brain, as it is an essential cofactor for many proteins that are involved in normal function of neuronal tissue.[1,2] With normal aging, progressive iron deposition in the brain occurs, with most of it located in the basal ganglia.[3,4] Excessive iron accumulation is associated with neurodegenerative conditions, such as Alzheimer's disease, Parkinson's disease, and Lewy Body dementia.[5,6] In addition to age differences, gender differences in brain iron levels have also been found. In one study, women were found to have lower iron levels than men.[6] Outside the brain, iron is thought to play a role in the pathogenesis of atherosclerosis. The iron hypothesis states that stored tissue iron may be an important determinant for the development of atherosclerosis. Iron uptake in macrophages is an early and important event in atherosclerosis and iron accumulation in atherosclerotic lesions is associated with unstable plaques.[7,8] Therefore, atherosclerotic risk factors may be associated with iron deposition in the brain, but this has not been investigated previously.

Although the exact mechanism of iron deposition is not completely elucidated,[9] iron must cross the blood-brain barrier (BBB) to enter the brain. As iron accumulates mainly in the basal ganglia, the changes in the BBB could be expected in the perforating arteries supplying the basal ganglia area. Increased permeability of the perforating arteries is also seen in cerebral small vessel disease.[10-12] Indicators of cerebral small vessel disease are lacunar infarcts and white matter lesions (WML). In addition, microbleeds are thought to be caused by leakage of red blood cells from small blood vessels in the brain.[13] As lacunar infarcts, WML and microbleeds all involve increased permeability of cerebral small vessels, it is possible that this increased permeability could lead to increased iron deposition in the basal ganglia as a secondary consequence.[1] However, it is not known whether lacunar infarcts, WML or microbleeds are associated with increased iron deposition in the brain.

MRI has made it possible to study brain iron depositions non-invasively in living subjects.[14] The presence of paramagnetic iron will decrease the transverse relaxation time (T2*), and the relaxation is proportional to the concentration of paramagnetic ions.[15] This makes T2* measurements suitable to quantify brain iron accumulation.[5] The use of ultra-high field strengths, such as 7 Tesla, result in a dramatic increase in susceptibility contrast, sensitivity and resolution.[16] This could be very useful to detect subtle changes in iron concentration.

The purpose of this study was first to investigate associations between age, sex, atherosclerotic risk factors and iron deposition measured with T2* measurements at 7 Tesla, and second to investigate whether the presence of lacunar infarcts, WML or microbleeds was associated with increased iron deposition in the basal ganglia.

Materials and Methods

Participants and design

Patients from the Second Manifestations of ARTerial disease (SMART) study,[17] without contraindications for 7T MRI, were consecutively included between July 2008 and February 2010. The rationale and design of the SMART study, including inclusion criteria, have been described in detail elsewhere.[17] In short, all eligible patients, newly referred to the University Medical Center Utrecht with symptomatic vascular disease or vascular risk factors, are screened for additional risk factors and severity of vascular disease. During a 1-day visit to our medical center, blood and urine sampling was performed, as well as a physical examination and ultrasonography of the carotid arteries. Risk factors, medical history, and functioning were assessed with questionnaires that the patients completed before their visit to the medical center. For the purpose of this study, a 1.5T MRI of the brain was made to assess brain infarcts, white matter lesions and brain atrophy,[18,19] and a 7T MRI scan was made to study microbleeds and brain iron. The SMART study and the brain imaging were approved by the medical ethics committee of our hospital. Written informed consent was given by all patients. For this study, T2*-weighted images were available for 56 patients. Seven patients were excluded due to motion-artefacts in the scans, leaving 49 patients for the analysis (table 1). Of these 49 patients, 18 were included with cerebrovascular disease, 9 with peripheral artery disease, 3 with coronary artery disease, 16 with vascular risk factors (diabetes mellitus n=13, hypertension n=1, hyperlipidemia n=2), and 3 with other manifestations of vascular disease.

Table 1 **Baseline characteristics of study sample**

	Study sample (n = 49)
Male gender	35 (71%)
Age (years)	59 ± 10
Systolic blood pressure (mm Hg)	136 ± 16
Diastolic blood pressure (mm Hg)	78 ± 11
Hypertension	35 (71%)
Diabetes mellitus	19 (39%)
Smoking, current	13 (27%)
Brain infarcts present	17 (35%)
Lacunar infarcts present	12 (25%)
White matter lesion volume relative to total intracranial volume (mL)	1.3 (0.4-11.1)
Microbleeds present	19 (39%)
Number of microbleeds	0 (0-13)

Age and blood pressure are expressed as mean with standard deviations; white matter lesion volume is expressed as median with 10th and 90th percentile; number of microbleeds is expressed as median with range, one patient with up to 100 microbleeds was excluded from the analysis on the number of microbleeds.

Magnetic Resonance Imaging 1.5 Tesla

The MR protocol on the 1.5 Tesla whole-body system (Gyroscan ACS-NT, Philips Medical Systems, Best, the Netherlands) consisted of transversal T1-weighted (TR/TE: 235/2 ms), T2-weighted (TR/TE: 2200/11 ms and 2200/100 ms), fluid-attenuating inverse recovery (FLAIR) (TR/TE/inversion time (TI): 6000/100/2000 ms) and inversion recovery (IR) (TR/TE/TI: 2900/22/410 ms) sequences. Field of view was 230x230 mm, matrix size 180x256, slice thickness 4.0 mm, no gap, 38 slices.

Magnetic Resonance Imaging 7 Tesla

The 7 Tesla scan was performed on a 7 Tesla whole-body system (Philips Healthcare, Cleveland, OH, USA), using a volume transmit and 16-channel receive head coil (Nova Medical, Wilmington, MA, USA), on the same day as the 1.5T scan. A 3D dual echo T2*-weighted scan (TR 20 ms, TE 2.5/15 ms, matrix size 508x399, resolution 0.35x0.4x0.6 mm^3, 167 slices, with flow compensation and acceleration factor 2.5) was made, and a multislice T2-weighted scan (TR/TE: 5193/60 ms, field of view 230x171, matrix size 460x242, slice thickness 4.0 mm, gap 1 mm, 24 slices).

Calculation of T2 in basal ganglia*

The dual echo T2*-weighted sequence at 7 Tesla was used to estimate the T2* of the basal ganglia. Regions of interest (ROIs) were drawn by one investigator (MC) in two consecutive slices of the T2-weighted scan where the basal ganglia were largest in diameter and could be clearly distinguished from surrounding tissue. The ROIs included the putamen, globus pallidus and caudate nucleus in both hemispheres. The ROIs were registered to the T2* using the transformation matrix that was obtained from the registration of the T2 to the T2*-weighed images using a 7 degrees-of-freedom registration algorithm with a correlation ratio cost function, implemented in Java Image Science Toolkit (JIST).[21] Because perivascular spaces filled with CSF can give very high T2*-values, which influences the mean T2* of the basal ganglia, we evaluated T2*-values of five patients without prominent perivascular spaces in the basal ganglia to determine the normal variation. In all five patients the mean T2* plus three times the standard deviation (SD) was below 40 ms. To filter out T2* from CSF, voxels with a T2* above 40 ms were left out of the analysis. Also, voxels that showed a fitted T2*-value of 0 or lower due to noise were left out. The T2*-values of the remaining voxels were averaged within each ROI in the left and right hemisphere together for each individual.

Brain segmentation and white matter lesions

For brain segmentation we used the T1-weighted, IR and FLAIR sequence from the 1.5T scan.[18,19,22] The segmentation program distinguishes cortical gray matter, white matter, CSF, and lesions. Results of the segmentation analysis were visually checked for the presence of infarcts and adapted if necessary to make a distinction between WML and infarct volumes (see below). Total brain volume was calculated by summing the volumes of gray and white matter and, if present, the volumes of WML and infarcts. All volumes cranial to the foramen magnum were included. Total intracranial volume (ICV) was calculated by summing the total brain volume and the volume of the CSF. Volumes of WML were normalized for ICV by dividing WML volume by ICV and multiplying this value by the mean ICV of the study population (1420.8 mL).

Brain infarcts

The whole brain was visually searched for infarcts by a trained investigator and a neuroradiologist on the 1.5T scan. Raters were blinded to the history and diagnosis of the patient. Discrepancies in rating were re-evaluated in a consensus meeting. Infarcts were defined as focal hyperintensities on T2-weighted images of at least 3 mm in diameter. Hyperintensities located in the white matter also had to be hypointense on T1-weighted and FLAIR images in order to distinguish them from WML. Dilated perivascular spaces were distinguished from infarcts on the basis of their location, form, and the absence of gliosis. We defined lacunar infarcts as infarcts sized 3 to 15 mm in diameter in plane and located in the subcortical white matter, thalamus or basal ganglia. Other brain infarcts included cortical infarcts, large subcortical infarcts, and infratentorial infarcts, and these were categorized as non-lacunar infarcts in the analyses.

Microbleeds

Microbleeds were independently scored on the dual echo T2*-weighted scan at 7T by two experienced neuroradiologists, blinded to all clinical information, and evaluated in a consensus meeting to obtain a final score. After consensus was reached on the first 50% of scans, the remaining scans were scored by one of the neuroradiologists. The rating of the microbleeds was based on the Microbleed Anatomical Rating Scale (MARS)[23] and scored as 'definite' microbleeds if they appeared as small, rounded or circular, well-defined hypointense lesions within brain parenchyma with clear margins ranging from 2 to 10 mm in size on GRE T2*-weighted images. We slightly adjusted this definition by excluding the size-criterion because due to the blooming effect, microbleeds appear larger on GRE T2*-weighted scan than the actual size of the microbleeds. The blooming effect depends among others on the field strength and the echo time, and will therefore differ with different imaging protocols. Symmetrical areas of calcification in the basal ganglia, choroid plexus and pineal gland were excluded, as were signal voids caused by sulcal vessels and low-signal lesions thought to be signal voids due to adjacent bone.[24]

Phase imaging

We used phase images to distinguish whether differences in T2* between patients were due to iron deposition in the basal ganglia or other factors that influence T2* such as calcifications. Of the phase images of the second echo, the derivative was calculated, showing the change in phase and thus magnetic field.[25] The phase derivative images of three random patients with different T2*-values of the basal ganglia were analyzed to assess differences in contrast on the phase derivative image. The variability in phase was quantitatively assessed with use of the phase derivative values in the area of the basal ganglia. A wider distribution of the phase derivative values corresponds to stronger changes in the phase and hence larger field disturbing properties of the enclosed object, indicating a higher concentration of paramagnetic iron.

Vascular risk factors

During the patient's visit to the medical center, an overnight fasting venous blood sample was taken to determine glucose levels. Blood pressure was measured twice with a sphygmomanometer and the average of the two measures was calculated. Hypertension was defined as mean systolic blood pressure ≥160 mm Hg or mean diastolic blood pressure ≥95 mm Hg or self reported use of antihypertensive drugs. Diabetes mellitus was defined as a history of diabetes mellitus, glucose ≥7.0 mmol/L or self reported use of oral antidiabetic drugs or insulin. Smoking habits were assessed with questionnaires and categorized as never/former or current. Patients who had quit smoking during the past year were assigned to the category current.

Statistical Analysis

First, linear regression was used to estimate the associations of age, sex, systolic blood pressure, diastolic blood pressure, hypertension, diabetes mellitus and smoking habits with the T2* of the basal ganglia. Second, associations of lacunar infarcts (present vs. absent), white matter lesions (per mL increase, and upper quartile vs. lower three quartiles), and microbleeds (present vs. absent, and number of microbleeds) with the T2* was estimated using linear regression analyses and ANCOVA. In model 1 no adjustments were made and in model 2 associations were adjusted for age and sex. In one patient up to 100 microbleeds were seen on the 7T scan. This was considerably more than in all other patients (range 1-13). To prevent that the results of analysis on the number of microbleeds depended highly on the scan of this single patient with many microbleeds, this patient was considered as an outlier and excluded from this analysis.

Results

In the whole study sample (n=49), the mean T2* at 7T of the putamen was 15.8 ms (SD 2.8), the mean T2* of the globus pallidus was 12.7 ms (SD 1.9), and the mean T2* of the caudate nucleus was 20.7 ms (SD 3.4). The Pearson correlation coefficients between age and T2* of the putamen, globus pallidus, and caudate nucleus were -0.41 (p=0.004), -0.16 (p=0.261) and -0.34 (p=0.019) respectively (figure 1).

Figure 1 Scatterplot of T2* of putamen, globus pallidus and caudate nucleus with age

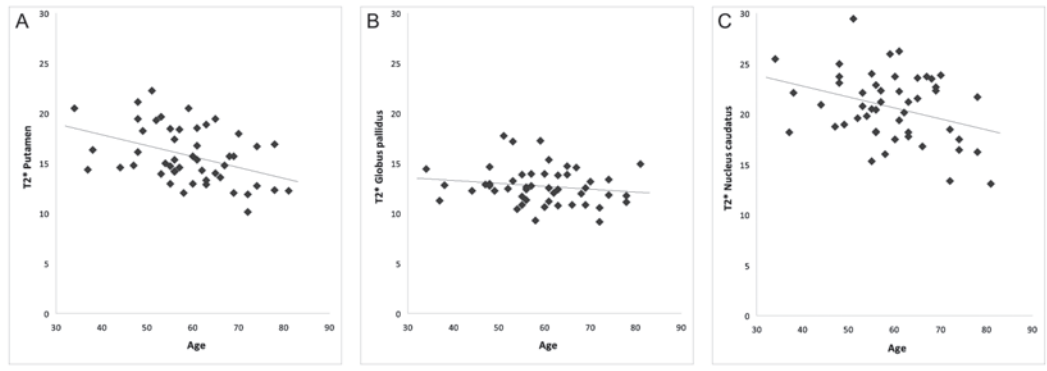

Significant correlation between T2 of the putamen and caudate nucleus and age shown in* [**A**] *and* [**C**]. *No significant correlation was found for the globus pallidus and age, as shown in* [**B**].

Risk factors

Linear regression analysis showed that older age was significantly associated with a lower T2* of the putamen (B=-0.11, 95% CI -0.18 to -0.04, p=0.004), and of the caudate nucleus (B=-0.11, 95 CI -0.20 to -0.02, p=0.02), also after adjusting for sex (table 2). There was no significant association between the T2* of the globus pallidus and age (table 2). Male sex was associated with a significantly lower T2* of the globus pallidus compared to female sex (B=-1.24, 95% CI -2.38 to -0.10, p=0.03), which remained significant after adjusting for age. No significant association was found between male sex and T2* for the putamen and caudate nucleus (table 2). Systolic or diastolic blood pressure, hypertension, diabetes and smoking were not significantly associated with the T2* of any of the basal ganglia (table 2).

Table 2 **Results of linear regression for the association between clinical variables and T2*-values of the basal ganglia**

	Putamen B (95% CI)	*p*-value	Globus pallidus B (95% CI)	*p*-value	Caudate nucleus B (95% CI)	*p*-value
Age (per year increase)						
Model 1	-0.11 (-0.18 to -0.04)	*0.004*	-0.03 (-0.08 to 0.02)	*0.261*	-0.11 (-0.20 to -0.02)	*0.019*
Model 2	-0.11 (-0.18 to -0.03)	*0.005*	-0.02 (-0.07 to 0.03)	*0.349*	-0.11 (-0.20 to -0.02)	*0.023*
Men vs. women						
Model 1	-0.99 (-2.78 to 0.81)	*0.273*	-1.24 (-2.38 to -0.10)	*0.033*	-0.71 (-2.88 to 1.47)	*0.517*
Model 2	-0.72 (-2.40 to 0.95)	*0.389*	-1.18 (-2.33 to -0.04)	*0.044*	-0.44 (-2.53 to 1.65)	*0.673*
Systolic blood pressure (per mm Hg increase)						
Model 1	0.00 (-0.05 to 0.05)	*0.966*	-0.01 (-0.04 to 0.03)	*0.677*	-0.03 (-0.09 to 0.03)	*0.099*
Model 2	0.02 (-0.03 to 0.07)	*0.331*	0.00 (-0.03 to 0.04)	*0.813*	-0.03 (-0.09 to 0.03)	*0.301*
Diastolic blood pressure (per mm Hg increase)						
Model 1	0.00 (-0.07 to 0.08)	*0.914*	-0.01 (-0.06 to 0.04)	*0.728*	-0.04 (-0.13 to 0.05)	*0.400*
Model 2	0.02 (-0.06 to 0.09)	*0.630*	0.01 (-0.05 to 0.06)	*0.824*	-0.03 (-0.12 to 0.06)	*0.490*
Hypertension (yes vs. no)						
Model 1	-0.52 (-2.33 to 1.29)	*0.564*	-0.72 (-1.90 to 0.46)	*0.224*	-0.32 (-2.51 to 1.85)	*0.764*
Model 2	-0.37 (-2.05 to 1.32)	*0.664*	-0.69 (-1.83 to 0.45)	*0.229*	-0.17 (-2.27 to 1.93)	*0.871*
Diabetes (yes vs. no)						
Model 1	-0.21 (-1.89 to 1.48)	*0.807*	0.62 (-0.48 to 1.71)	*0.262*	-0.87 (-2.88 to 1.14)	*0.387*
Model 2	-0.12 (-1.69 to 1.44)	*0.876*	0.67 (-0.38 to 1.73)	*0.203*	-0.80 (-2.73 to 1.13)	*0.410*
Smoking (current vs. never/former)						
Model 1	-0.01 (-1.87 to 1.85)	*0.993*	0.35 (-0.87 to 1.57)	*0.193*	-0.13 (-2.36 to 2.10)	*0.905*
Model 2	-0.54 (-2.29 to 1.22)	*0.541*	0.21 (-0.99 to 1.41)	*0.211*	-0.66 (-2.84 to 1.52)	*0.548*

***Model 1**: no adjustments, **Model 2**: adjusted for age and sex*

Lacunar infarcts

The T2* of the putamen, globus pallidus and caudate nucleus was lower in patients with lacunar infarcts compared to patients without lacunar infarcts, although this difference was not statistically significant for the putamen and globus pallidus. After adjustment for age and sex the difference in T2* attenuated but the T2* of the caudate nucleus remained significantly lower in patients with lacunar infarcts (table 3).

White matter lesions

Increase in WML volume per mL showed no significant association with T2* of the putamen (B=-0.07, 95% CI -0.23 to 0.09, p=0.38), globus pallidus (B=-0.03, 95% CI -0.14 to 0.07, p=0.54) or caudate nucleus (B=-0.17, 95% CI -0.35 to 0.02, p=0.08). When we compared patients with severe WML load (upper quartile) with the rest of the sample (lower three quartiles) the T2* of the caudate nucleus was significantly lower in patients with severe WML and the T2* of the putamen was borderline significantly lower in patients with severe WML (table 3). However, after adjustment for age and sex these differences decreased and were no longer significant. The T2* of the globus pallidus was not associated with severe WML, with or without adjustment for age and sex (table 3).

Table 3 **Mean difference in T2* of the putamen, globus pallidus and caudate nucleus related to lacunar infarcts, white matter lesions and microbleeds.**

	T2* Putamen mean (95% CI)	*p*-value	T2* Globus pallidus mean (95% CI)	*p*-value	T2* Caudate nucleus mean (95% CI)	*p*-value
Lacunar infarcts (present vs. absent)						
Model 1	-1.5 (-3.4 to 0.4)	*0.111*	-0.9 (-2.2 to 0.3)	*0.136*	-3.2 (-5.3 to -1.1)	*0.003*
Model 2	-0.2 (-2.2 to 1.9)	*0.870*	-0.5 (-1.9 to 0.9	*0.505*	-2.6 (-5.0 to -0.1)	*0.040*
White matter lesions (upper quartile vs. lower three)						
Model 1	-1.7 (-3.5 to 0.1)	*0.060*	-0.4 (-1.6 to 0.8)	*0.524*	-2.4 (-4.5 to -0.2)	*0.030*
Model 2	-0.3 (-2.4 to 1.8)	*0.764*	0.2 (-1.2 to 1.6)	*0.794*	-1.3 (-3.9 to 1.2)	*0.301*
Microbleeds (present vs absent)						
Model 1	-0.6 (-2.3 to 1.1)	*0.466*	-0.2 (-1.4 to 0.9)	*0.656*	-0.2 (-2.3 to 1.8)	*0.829*
Model 2	-0.4 (-2.0 to 1.2)	*0.622*	-0.2 (-1.2 to 0.9)	*0.778*	0.0 (-2.0 to 2.0)	*0.996*

***Model 1**: no adjustments, **Model 2**: adjusted for age and sex*

Microbleeds

No significant differences were found in T2* of the putamen, globus pallidus or caudate nucleus between patients with and without microbleeds (table 3). Also, analysis of the number of microbleeds showed no significant association with T2* of the putamen (B=-0.07, 95% CI -0.44 to 0.30, p=0.71), globus pallidus (B=-0.03, 95% CI -0.29 to 0.22, p=0.79) or caudate nucleus (B=0.04, 95% CI -0.43 to 0.50, p=0.87), adjusted for age and sex.

Phase imaging

Figure 2 shows the phase derivative images of two patients with different T2*-values of the putamen, globus pallidus and caudate nucleus. The images show high contrast in the region of the basal ganglia. The appearance of positive phase derivative (white) and negative phase derivative (black) are consistent with a paramagnetic field disturbance due to the iron.[26] The patient with a lower T2* of the basal ganglia also showed a wider distribution in phase variation (mean 0.45 rad/mm, SD 0.28) compared to the patient with a higher T2* (mean 0.24 rad/mm,

SD 0.195). The difference in T2* between the patients is also visible as a difference in hypointensity of the basal ganglia in the magnitude images of the second echo of the T2*-weighted sequence.

Figure 2 **Phase images and magnitude images of two patients with different T2*-values of the basal ganglia**

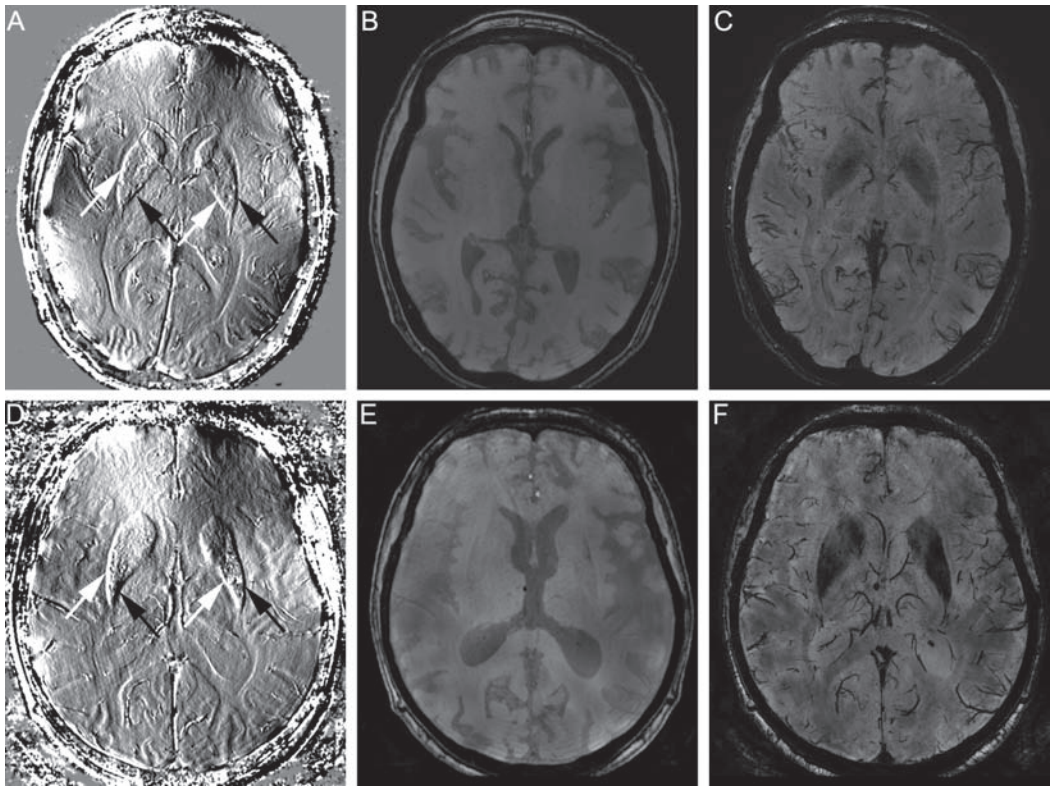

Figure 2 | *The appearance of the phase shifts (positive phase shift white arrow, negative phase shift black arrow) in the basal ganglia shown in* [**A**] *and* [**D**] *are characteristic for iron deposition.* [**B**] *and* [**E**] *show a minimal intensity projection of the magnitude images of the first echo of the T2*-weighted sequence, where the basal ganglia are hardly visible. On the second echo of the T2*-weighted sequence (***C*** *and* ***F****) the basal ganglia are visible as hypointense structures. The basal ganglia of the patient shown in* [**F**] *(mean T2* 12.8 ms, SD 5.2) are more hypointense than the basal ganglia of the patient shown in* [**C**] *(mean T2* 18.5 ms, SD 5.1), indicating more iron deposition in the patient shown in* [**F**].

Secondary analysis

It has been postulated that the mean T2* over the whole brain could vary between subjects. To test whether this variation was present, an additional ROI in the corpus callosum was drawn as a reference to evaluate whether T2*-values of the corpus callosum correlated with the investigated ones. Absence of this correlation (Pearson's correlation coefficient 0.06, p=0.7) suggested that no correction was needed.

Discussion

In 49 patients of the SMART study, we found that at 7 Tesla MRI the T2* of the putamen and caudate nucleus significantly decreased with older age. The T2* of the globus pallidus was significantly lower in men than in women. Atherosclerotic risk factors were not associated with T2* of the basal ganglia. Presence of lacunar infarcts was associated with a significantly lower T2* of the caudate nucleus, also after adjusting for age and sex. However, after adjusting for age and sex the differences in T2* between patients with severe and less severe WML disappeared. Microbleeds were not associated with changes in T2* of the basal ganglia. The phase images showed characteristic phase changes suggestive of iron in the basal ganglia, indicating that the decrease in T2* found in this study was due to iron deposition.

To our knowledge, this is the first study that examined the association of age and sex with iron deposition in the basal ganglia using T2* measurements at 7 Tesla. The advantage of 7 Tesla is the increased sensitivity, signal to noise ratio and especially the increased susceptibility contrast at high field. This makes it suitable for the detection of small differences in susceptibility and thus for small differences in iron deposition. Furthermore, the use of T2*-weighted imaging at 7T also results in accurate detection of microbleeds.[20] Another strength of this study is the use of phase images. Whereas T2* can be influenced by many factors, the phase images confirm that the differences found in T2* between patients are due to iron deposition.

A limitation of our study is the relatively small study sample, which will have resulted in reduced power to find significant associations. Another limitation is that the dual echo T2*-weighted sequence we used for the calculation of the T2*-values was optimized in speed and image quality to depict venous and arterial blood vessels. As a result, the imaging parameters of the first and second echo time differed slightly, most notably a different amount of k-space filling. The first (partial) echo contains less sample points in k-space, and therefore has a relatively lower signal to noise ratio. However, as this echo is acquired at 2.5 ms it already has a higher signal to noise ratio than the second echo. Also, values of the fitted T2* are averaged over the specified ROIs, making them robust to the reduced signal to noise ratio. Therefore the T2* measurement could be used to compare iron deposition in patients with and without lesions within the study population.

Our finding that iron deposition increases with age is consistent with post-mortem data and MRI studies at lower field strengths.[3,4,27] We found that the T2* decreased with older age in the putamen and caudate nucleus, but not in the globus pallidus. Post-mortem and MRI studies have shown that iron deposition in the globus pallidus mainly occurs in the first three decades of life, reaching a plateau after the age of 30, whereas iron deposition in the putamen and caudate nucleus continues at older ages.[3-5] As our study population was above the age of 30, this may explain why we did not find an association between the T2* of the globus pallidus and age.

We found higher T2*-values of the globus pallidus in women, indicating less iron deposition. Although it is unclear what causes the differences in iron deposition between men and women, the one other study reporting sex differences in brain iron levels also showed that women had significantly less iron than men in the caudate nucleus, thalamus, frontal lobe and genu and splenium of the corpus callosum.[6]

None of the vascular risk factors were associated with the T2* of the basal ganglia in our study. Since this is the first study to examine vascular risk factors for iron deposition in the basal ganglia, we cannot compare our findings with existing studies. However, because our study sample was relatively small and the estimates and confidence intervals greatly varied, it is possible that statistical power was too low to find significant associations or that the associations of vascular risk factors with T2* were too small to be detected.

We observed a significantly lower T2* in patients with lacunar infarcts compared to those without lacunar infarcts, which remained after adjusting for age and sex, indicating more iron deposition in patients with lacunar infarcts. It is thought that an impaired blood-brain barrier is part of the pathophysiology of lacunar infarcts and possibly this

could result in increased iron deposition. Regarding the association between iron deposition and lacunar infarcts, brain iron deposition can be a promising new marker for cerebral small vessel disease.

Interestingly, we observed that the association of the T2* with severe WML was explained by age. An explanation for the different associations of lacunar infarcts and WML with the T2* of the basal ganglia may be the location of the lesions. Most lacunar infarcts are located near or in the basal ganglia, whereas WML are located periventricularly or in the deep white matter. This could also explain why we did not find an association between the presence or number of microbleeds and iron deposition in the basal ganglia. In our study the majority of microbleeds were in lobar locations and not located in or near the basal ganglia. Microbleeds may be due to very localized changes of the vessel wall and BBB permeability, and may therefore not influence iron deposition in the basal ganglia.

The mean T2*-values found in our study at 7T, are comparable with those in another study. This study, comparing T2*-values between 1.5T, 3T and 7T, found a T2* of 19.7 ms in the putamen, 11.6 ms in the globus pallidus and 20.3 in the caudate nucleus at 7T,[16] which corresponds closely with the 15.8 ms, 12.7 ms and 20.7 ms we found for the respective basal ganglia.

Previous studies have shown that there is an uneven distribution of iron in the brain, as iron deposition varies with age, disease status and brain region.[1,28] The lower T2*-values found with age, male sex, and lacunar infarcts in our study were also not consistent over the three basal ganglia that were investigated. This implies that mechanisms of iron deposition differ between brain regions,[28] which may explain the different associations between age, sex, lacunar infarcts and the separate basal ganglia.

Both calcium and iron deposits can cause the basal ganglia to appear hypointense on T2*-weighted imaging. It is usually not possible to differentiate between calcium and iron on the magnitude images. However, phase images can be used to differentiate between calcium and iron, through specific appearances of the phase shifts in areas with calcium or iron.[26] The characteristic phase appearance we found in the phase images suggests that the decrease in T2* found in this study was due to iron deposition.

In sum, in this study using T2* measurements at 7 Tesla, older age, male sex and presence of lacunar infarcts were associated with increased iron deposition in one or more basal ganglia. Future studies should determine whether these results can be replicated in larger study samples.

Chapter 06 Iron deposition in basal ganglia at 7T: determinants and relation with cerebral small vessel disease

References

1 Ke Y, Qian ZM. Brain iron metabolism: neurobiology and neurochemistry. *Prog Neurobiol* 2007;83:149-173.
2 Zecca L, Youdim MB, Riederer P, Connor JR, Crichton RR. Iron, brain ageing and neurodegenerative disorders. *Nat Rev Neurosci* 2004;5:863-873.
3 Bartzokis G, Beckson M, Hance DB, Marx P, Foster JA, Marder SR. MR evaluation of age-related increase of brain iron in young adult and older normal males. *Magn Reson Imaging* 1997;15:29-35.
4 Hallgren B, Sourander P. The effect of age on the non-haemin iron in the human brain. *J Neurochem* 1958;3:41-51.
5 Aquino D, Bizzi A, Grisoli M, Garavaglia B, Bruzzone MG, Nardocci N, Savoiardo M, Chiapparini L. Age-related iron deposition in the basal ganglia: quantitative analysis in healthy subjects. *Radiology* 2009;252:165-172.
6 Bartzokis G, Tishler TA, Lu PH, Villablanca P, Altshuler LL, Carter M, Huang D, Edwards N, Mintz J. Brain ferritin iron may influence age- and gender-related risks of neurodegeneration. *Neurobiol Aging* 2007;28:414-423.
7 de Valk B, Marx JJ. Iron, atherosclerosis, and ischemic heart disease. *Arch Intern Med* 1999;159:1542-1548.
8 Yuan XM, Li W. The iron hypothesis of atherosclerosis and its clinical impact. *Ann Med* 2003;35:578-591.
9 Mills E, Dong XP, Wang F, Xu H. Mechanisms of Brain Iron Transport: Insight into Neurodegeneration and CNS Disorders. *Future Med Chem* 2010;2:51.
10 Hassan A, Hunt BJ, O'Sullivan M, Parmar K, Bamford JM, Briley D, Brown MM, Thomas DJ, Markus HS. Markers of endothelial dysfunction in lacunar infarction and ischaemic leukoaraiosis. *Brain* 2003;126:424-432.
11 Wardlaw JM, Sandercock PA, Dennis MS, Starr J. Is breakdown of the blood-brain barrier responsible for lacunar stroke, leukoaraiosis, and dementia? *Stroke* 2003;34:806-812.
12 Wardlaw JM, Doubal F, Armitage P, Chappell F, Carpenter T, Munoz MS, Farrall A, Sudlow C, Dennis M, Dhillon B. Lacunar stroke is associated with diffuse blood-brain barrier dysfunction. *Ann Neurol* 2009;65:194-202.
13 Fazekas F, Kleinert R, Roob G, Kleinert G, Kapeller P, Schmidt R, Hartung HP. Histopathologic analysis of foci of signal loss on gradient-echo T2*-weighted MR images in patients with spontaneous intracerebral hemorrhage: evidence of microangiopathy-related microbleeds. *AJNR Am J Neuroradiol* 1999;20:637-642.
14 Schenck JF, Zimmerman EA. High-field magnetic resonance imaging of brain iron: birth of a biomarker? *NMR Biomed* 2004;17:433-445.
15 Haacke EM, Cheng NY, House MJ, Liu Q, Neelavalli J, Ogg RJ, Khan A, Ayaz M, Kirsch W, Obenaus A. Imaging iron stores in the brain using magnetic resonance imaging. *Magn Reson Imaging* 2005;23:1-25.
16 Yao B, Li TQ, Gelderen P, Shmueli K, de Zwart JA, Duyn JH. Susceptibility contrast in high field MRI of human brain as a function of tissue iron content. *Neuroimage* 2009;44:1259-1266.
17 Simons PC, Algra A, van de Laak MF, Grobbee DE, van der Graaf Y. Second manifestations of ARTerial disease (SMART) study: rationale and design. *Eur J Epidemiol* 1999;15:773-781.
18 Anbeek P, Vincken KL, van Osch MJ, Bisschops RH, van der Grond J. Automatic segmentation of different-sized white matter lesions by voxel probability estimation. *Med Image Anal* 2004;8:205-215.
19 Anbeek P, Vincken KL, van Osch MJ, Bisschops RH, van der Grond J. Probabilistic segmentation of white matter lesions in MR imaging. *Neuroimage* 2004;21:1037-1044.
20 Conijn MM, Geerlings MI, Luijten PR, Zwanenburg JJ, Visser F, Biessels GJ, Hendrikse J. Visualization of cerebral microbleeds with dual-echo T2*-weighted magnetic resonance imaging at 7.0 T. *J Magn Reson Imaging* 2010;32:52-59.

21 Lucas BC, Bogovic JA, Carass A, Bazin PL, Prince JL, Pham DL, Landman BA. The Java Image Science Toolkit (JIST) for rapid prototyping and publishing of neuroimaging software. *Neuroinformatics* 2010;8:5-17.
22 Geerlings MI, Appelman AP, Vincken KL, Algra A, Witkamp TD, Mali WP, van der Graaf Y. Brain volumes and cerebrovascular lesions on MRI in patients with atherosclerotic disease. The SMART-MR study. *Atherosclerosis* 2010;210:130-136.
23 Gregoire SM, Jager HR, Yousry TA, Kallis C, Brown MM, Werring DJ. Brain microbleeds as a potential risk factor for antiplatelet-related intracerebral haemorrhage: hospital-based, case-control study. *J Neurol Neurosurg Psychiatry* 2010;81:679-684.
24 Greenberg SM, Vernooij MW, Cordonnier C, Viswanathan A, Al-Shahi SR, Warach S, Launer LJ, Van Buchem MA, Breteler MM. Cerebral microbleeds: a guide to detection and interpretation. *Lancet Neurol* 2009;8:165-174.
25 Bakker CJ, de Leeuw H, Vincken KL, Vonken EJ, Hendrikse J. Phase gradient mapping as an aid in the analysis of object-induced and system-related phase perturbations in MRI. *Phys Med Biol* 2008;53:N349-N358.
26 Ogg RJ, Langston JW, Haacke EM, Steen RG, Taylor JS. The correlation between phase shifts in gradient-echo MR images and regional brain iron concentration. Magn Reson Imaging 1999;17:1141-1148.
27 Bartzokis G, Mintz J, Sultzer D, Marx P, Herzberg JS, Phelan CK, Marder SR. In vivo MR evaluation of age-related increases in brain iron. *AJNR Am J Neuroradiol* 1994;15:1129-1138.
28 Connor JR, Snyder BS, Arosio P, Loeffler DA, LeWitt P. A quantitative analysis of isoferritins in select regions of aged, parkinsonian, and Alzheimer's diseased brains. *J Neurochem* 1995;65:717-724.

Chapter 06 Iron deposition in basal ganglia at 7T: determinants and relation with cerebral small vessel disease

CHAPTER 07

Microbleeds, lacunar infarcts, white matter lesions and cerebrovascular reactivity - a 7T study

Mandy M.A. Conijn
Johannes M. Hoogduin
Yolanda van der Graaf
Jeroen Hendrikse
Peter R. Luijten
Mirjam I.Geerlings

Abstract

Background and Purpose

The underlying pathology of lacunar infarcts, white matter lesions and also of microbleeds is poorly understood. We assessed whether the presence of lacunar infarcts, white matter lesions or microbleeds on MRI was associated with a decrease in cerebrovascular reactivity in patients with atherosclerotic disease, and assessed whether this association was similar for lacunar infarcts, white matter lesions and microbleeds.

Methods

BOLD-fMRI scan with breath-holding at 7 Tesla and anatomical scans at 1.5 Tesla were available in 49 patients with atherosclerotic disease from the Second Manifestations of ARTerial disease (SMART) study. Microbleeds and lacunar infarcts were scored visually and volumetric assessment of white matter lesions was performed on the 1.5T scan. The percentage of activated voxels and the whole brain signal change were calculated as measures of cerebrovascular reactivity. The mean percentage of activated voxels was 25.1% (SD 6.6) and the mean percentage whole brain signal change was 1.20% (SD 0.51).

Results

Age, gender, and diastolic blood pressure were significantly associated with cerebrovascular reactivity. Cerebrovascular reactivity was lower with increasing age, lower in females compared to males and lower with lower diastolic blood pressure. ANCOVA showed that patients with microbleeds (n=18) had a significantly lower whole brain signal change than patients without microbleeds, with a mean difference of -0.36% (95% CI -0.64 to -0.07), independent of age, sex, systolic and diastolic blood pressure and non-lacunar infarcts. No significant associations were found for presence of lacunar infarcts or white matter lesion volume with whole brain signal change or percentage of activated voxels.

Conclusion

Presence of microbleeds is associated with an impaired cerebrovascular reactivity in patients with atherosclerotic disease, whereas no significant association was found for the presence of lacunar infarcts or white matter lesions in our study.

Introduction

Lacunar infarcts and white matter lesions (WML) are thought to result from changes in small vessels in the brain. Although the underlying pathology is poorly understood,[1-5] studies indicate that the vessel wall is involved in this process.[6,7] There is increasing evidence that endothelial dysfunction plays a role.[8-10] The increased permeability of the blood-brain barrier may lead to entry of serum components into the vessel wall, causing thickening, inflammation and disorganization of the vessel wall.[10] Microbleeds are associated with lacunar infarcts and WML and are also thought to result from changes in small vessels in the brain.[11,12] It has been suggested that microbleeds and lacunar infarcts have a similar vascular pathology.[13] The changes in the small vessels in lacunar infarcts and WML and possibly also in microbleeds may lead to stiffening of the vessel wall, resulting in impairment of the cerebrovascular reactivity (CVR).

CVR reflects the compensatory dilatory capacity of cerebral vasculature to a dilatory stimulus such as carbon dioxide or acetazolamide.[14] FMRI based on blood oxygenation level-dependent contrast (BOLD-fMRI) is a reliable and reproducible method to quantify CVR.[15,16] An advantage of BOLD-fMRI is that it assesses CVR on tissue-level. Previous studies investigating CVR in relation with lacunar infarcts and WML often used transcranial Doppler ultrasonography.[14,17-20] However, transcranial Doppler ultrasonography measures blood flow velocity in the middle cerebral artery, whereas the BOLD-signal depends on reactivity of all vessels in the brain. A pilot study showed a reduction in CVR, measured with BOLD-fMRI at 3 Tesla, between patients with WML and lacunar infarcts and healthy controls.[21] Changes in the acquisition strategies can affect the observed BOLD-signal. An important parameter in the acquisition is field strength. With increasing field strength, the specificity, sensitivity and contrast of the BOLD-response increases.[22] This can be an advantage for the investigation of the relation between lesions thought to be caused by changes in small vessels and CVR. To our knowledge, the association between CVR and microbleeds has not yet been examined, and also BOLD-fMRI at 7 Tesla has not yet been used to assess the association between CVR and lacunar infarcts and WML. We investigated associations of lacunar infarcts, WML and microbleeds with CVR using BOLD-fMRI at 7 Tesla in patients with atherosclerosis.

Methods

Participants

Patients newly referred to our hospital with symptomatic and asymptomatic atherosclerotic disease from the Second Manifestations of ARTerial disease (SMART) study,[23] without contraindications for 7T MRI, were consecutively included for the 7T study between July 2008 and February 2010. Atherosclerotic disease was defined as manifest coronary artery disease, cerebrovascular disease, peripheral arterial disease, abdominal aortic aneurysm, or risk factors for atherosclerosis (e.g. hypertension, diabetes). The objectives and design of the SMART study have been described elsewhere.[23] The SMART study and 7T imaging were approved by the medical ethics committee of our institution. Written informed consent was given by all patients.

For this study, BOLD-fMRI data were available for 58 patients. In 7 scans the BOLD-signal could not be calculated due to motion artefacts and two patients had a carotid artery stenosis >70%; these were excluded, leaving 49 patients for analysis (table 1). The mean age of the study population was 58.9 years (SD 10.0, range 34 to 80). Seventeen of the 49 patients were included in the SMART-study with vascular risk factors (13 diabetes mellitus, 1 hypertension, 1 hyperlipidemia), 14 patients with a stroke, 4 patients with coronary artery disease, 11 patients with peripheral artery disease, and 1 patient with ischemic renal failure.

Table 1 **Baseline characteristics of study sample**

	Study sample (n = 49)	
Male gender*	38	(76%)
Age (years) †	58.9	± 10.0
Systolic blood pressure (mm Hg) †	135.9	± 16.3
Diastolic blood pressure (mm Hg) †	78.5	± 10.5
Hypertension*	33	(67%)
Diabetes*	20	(41%)
Anticoagulant medication use*	1	(2%)
Antihypertensive medication use*	29	(59%)
Brain infarcts present*	13	(27%)
Non-lacunar infarcts present*	7	(14%)
Lacunar infarcts present*	9	(18%)
Number of lacunar infarcts ‡	0	(0-7)
Microbleeds present*	18	(37%)
Number of microbleeds ‡	0	(0-6)
Intracranial volume (mL)**	1439	(1292-1597)
Total brain volume (mL)**	1115	(984-1264)
White matter lesion volume relative to total intracranial volume (mL)		
Total (n=49)**	1.2	(0.4-8.0)
- Upper quartile (n=9)**	8.0	(5.0-28.0)
- Lower three quartiles (n=40)**	1.1	(0.3-3.1)

** number (percentage), † mean ± SD, ‡ median (range), one patient with >20 microbleeds was excluded from the analysis on the number of microbleeds, ** median (10th and 90th percentile)*

Magnetic Resonance Imaging 1.5 Tesla

The MR protocol on the 1.5T whole-body system (Gyroscan ACS-NT, Philips Medical Systems, Best, the Netherlands) consisted of transversal T1-weighted (repetition time (TR)/echo time (TE): 235/2 ms), T2-weighted (TR/TE: 2200/11 ms and 2200/100 ms), fluid-attenuating inverse recovery (FLAIR) (TR/TE/inversion time (TI): 6000/100/2000 ms) and inversion recovery (IR) (TR/TE/TI: 2900/22/410 ms) sequences. Field of view was 230x230 mm, matrix size 180x256, slice thickness 4.0 mm, no gap, 38 slices.

Magnetic Resonance Imaging 7 Tesla

On the same day as the 1.5T scan the 7 Tesla scan was performed on a 7T whole-body system (Philips Healthcare, Cleveland, OH, USA), using a volume transmit and 16-channel receive head coil (Nova Medical, Wilmington, MA, USA). A dual echo T2*-weighted scan (TR 20 ms, TE 2.5/15 ms, matrix size 508x399, resolution 0.35x0.4x0.6 mm^3, with flow compensation and acceleration factor 2.5) was made for visualization of microbleeds.[24]

A BOLD-fMRI scan with breath-holding was made for all patients. The breath-holding paradigm consisted of 5 periods of breath-holding interleaved with 30 s of normal breathing. The first 4 breath-holding periods lasted 21 s, the last one ‘as long as possible’. Data from the respiratory belt of the scanner was logged and used to evaluate task performance and the length of the ‘as long as possible’ condition. Single shot Echo Planar Imaging (EPI) with TR 3 s, TE 20 ms, 96 volumes, 45 slices with no gap, resolution 1.5x1.5x1.5 mm3, SENSE factor 3.5 (resulting in an EPI readout train of 41), was used to measure the BOLD-effect induced by the breath-hold task.

The use of thin slices helps to control the amount of through-slice dephasing due to susceptibility differences between air and tissue. Geometric distortions in the EPI images are limited by the application of SENSE. Multiple linear regression was applied to select activated voxels using a block model. The block was shifted by 5 volumes relative to the task to take into account the delayed BOLD-response to the task. A linear term was included in the model to account for scanner drift. Estimated signal changes were used to create a T-map. From all the voxels in this map, the number of voxels that were activated by the breath-holding task was calculated by applying a threshold of 2 on the T-map. A whole brain mask was created by setting a threshold on the first EPI volume and smoothing and eroding the result. This whole brain mask was used to select the voxels within the brain, excluding the skull. The number of voxels activated due to breath-holding was divided by the total number of voxels within the whole brain mask to obtain the percentage of activated voxels (CVR1).

CVR1 = (n / total) * 100%,

where *n* is the number of activated voxels due to breath-holding, and *total* is the total number of voxels within the whole brain mask. This measure was taken to compare the amount of voxels activated by breath-holding, as a measure for the size of the activated area in the brain. In addition, also the percentage change in signal over the whole brain before and after breath-holding was calculated (CVR2).

CVR2 = average signal change / average baseline signal * 100%,

where *average signal change* is the estimated signal change per voxel averaged over the whole brain mask and *average baseline signal* is the estimated baseline signal per voxel averaged over the whole brain mask. The estimated signal change and baseline signal per voxel were calculated using the block regression model described above. This measure was taken to compare the degree of reactivity between patients.

Microbleeds

Microbleeds were scored at the dual echo T2*-weighted scan at 7T, using both echo images.[24] The microbleeds were scored independently by two experienced neuroradiologists, blinded to all clinical information, and evaluated in a consensus meeting to obtain a final score. Inter-observer reliability for the number of microbleeds was good (ICC=0.61) and intra-observer reliability was very good (ICC=0.94). The remaining scans were therefore scored by one of the neuroradiologists. The rating of the microbleeds was based on the Microbleed Anatomical Rating Scale (MARS)[25] and scored as ‘definite’ microbleeds if they appeared as small, rounded or circular, well-defined hypointense lesions within brain parenchyma with clear margins ranging from 2 to 10 mm in size on GRE T2*-weighted images. We slightly adjusted this definition by excluding the size-criterion. Due to the blooming effect, microbleeds appear larger on GRE T2*-weighted scan than the actual size of the microbleeds. The blooming effect depends among others on the field strength and the echo time, and will therefore differ with different imaging protocols. Symmetrical areas of calcification in the basal ganglia, choroid plexus and pineal gland were excluded, as were signal voids caused by sulcal vessels and low-signal lesions thought to be signal voids due to adjacent bone.[12]

Brain segmentation and white matter lesions

We used the T1-weighted, IR and FLAIR sequence from the 1.5T scan for brain segmentation.[26,27] It distinguishes cortical gray matter, white matter, CSF, and lesions. Results of the segmentation analysis were visually checked for the presence of infarcts and adapted if necessary to make a distinction between WML and infarct volumes. Total brain volume was calculated by summing the volumes of gray and white matter and, if present, the volumes of WML and infarcts. All volumes cranial to the foramen magnum were included. Total intracranial volume (ICV)

was calculated by summing the total brain volume and the volume of the CSF. To correct for differences in head size, volumes of WML were normalized for ICV by dividing the WML volume of each patient by his/her ICV and then multiplying this value by the mean ICV of the study population (1423 mL) to obtain a relative volume of WML.

Brain infarcts

The whole brain was visually searched for infarcts by a trained investigator and a neuroradiologist on the 1.5T scan. Raters were blinded to the history and diagnosis of the patient. Discrepancies in rating were re-evaluated in a consensus meeting. Infarcts were defined as focal hyperintensities on T2-weighted images of at least 3 mm in diameter. Hyperintensities located in the white matter also had to be hypointense on T1-weighted and FLAIR images in order to distinguish them from WML. Dilated perivascular spaces were distinguished from infarcts on the basis of their location, form, and the absence of gliosis. Brain infarcts were categorized as lacunar infarcts and non-lacunar infarcts (cortical infarcts, large subcortical infarcts, infratentorial infarcts). We defined lacunar infarcts as infarcts sized 3 to 15 mm in diameter in plane and located in the subcortical white matter, thalamus or basal ganglia.[28]

Vascular risk factors

During the patient's visit to the medical center, an overnight fasting venous blood sample was taken to determine glucose levels. Blood pressure was measured twice with a sphygmomanometer and the average of the two measures was calculated. Hypertension was defined as mean systolic blood pressure ≥160 mm Hg or mean diastolic blood pressure ≥95 mm Hg or self reported use of antihypertensive drugs. Diabetes mellitus was defined as a history of diabetes mellitus, glucose ≥7.0 mmol/L or self reported use of oral antidiabetic drugs or insulin.

Statistical Analysis

First, linear regression was used to estimate the associations of age (per year increase), sex (man vs. women), systolic blood pressure (per mm Hg increase), diastolic blood pressure (per mm Hg increase), hypertension (yes vs. no), diabetes (yes vs. no), and non-lacunar infarcts (presence vs. absence) with the percentage of activated voxels and the percentage whole brain signal change. The analyses were adjusted for age and sex using multiple linear regression.

Second, the effect of microbleeds, lacunar infarcts and WML on CVR1 and CVR2 were studied using analysis of covariance (ANCOVA). In separate analyses the mean CVR1 and CVR2 were compared between patients with and without microbleeds, between patients with and without lacunar infarcts, and between patients with severe WML load (upper quartile) and patients with less WML (lower three quartiles).

The analyses were adjusted for age and sex in model 1, and additionally adjusted for systolic and diastolic blood pressure and non-lacunar infarcts in model 2; these variables were added as covariates to the ANCOVA model.

Third, to analyze the association between the number of microbleeds as a continuous variable and CVR1/CVR2, and the association between the increase in WML per mL and CVR1/CVR2, multiple linear regression was used, where CVR1 and CVR2 were the dependent variables, respectively, and number of microbleeds and increase in WML were the independent variables, respectively. These analyses were adjusted for age, sex, systolic and diastolic blood pressure and non-lacunar infarcts.

In the analysis of the number of microbleeds one patient with more than 20 microbleeds was excluded, as this was considerably more than in all other patients (range 1-6). To prevent that the results depended highly on the scan of this single patient with many microbleeds, this patient was considered as an outlier and excluded from the analysis on the number of microbleeds.

As a final step, all the above described analyses were additionally adjusted for use of anticoagulant or antihypertensive medication.

Results

Figure 1 shows an example an EPI and the activation pattern as a result of breath-holding of a patient without lacunar infarcts, WML or microbleeds. In the whole study sample (n=49), the mean percentage of activated voxels (CVR1) was 25.1% (SD 6.6) and the mean percentage whole brain signal change (CVR2) was 1.20% (SD 0.51). There was a moderate correlation between CVR1 and CVR2 (Pearson's correlation coefficient 0.60, p<0.001).

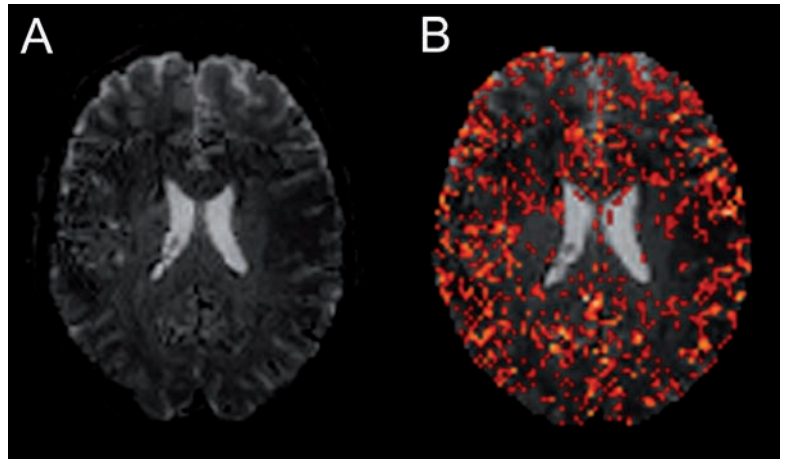

Figure 1 | [**A**] *EPI and* [**B**] *BOLD-fMRI activation after breath-holding of a patient without lacunar infarcts, white matter lesions or microbleeds on the MR scan.*

Older age was significantly associated with a decrease in CVR1, but not CVR2. Female sex and increase in diastolic blood pressure were associated with a significant decrease in CVR2, but not in CVR1. Systolic blood pressure, hypertension, diabetes and non-lacunar infarcts were not significantly associated with CVR1 or CVR2 (table 2).

Table 2 **Association between clinical variables and whole brain signal change and activated voxels**

	Activated voxels		Whole brain signal change	
	B	95% CI	B	95% CI
Age (per year increase)	-0.255	-0.439 to -0.071[b]	-0.007	-0.022 to 0.007
Sex (man vs. women)	-1.895	-6.273 to 2.484	-0.388	-0.732 to -0.043[a]
Systolic blood pressure (per mm Hg increase)	-0.034	-0.153 to 0.084	0.005	-0.004 to 0.014
Diastolic blood pressure (per mm Hg increase)	0.061	-0.118 to 0.241	0.015	0.001 to 0.028[a]
Hypertension (yes vs. no)	-0.797	-4.653 to 3.060	-0.070	-0.373 to 0.233
Diabetes (yes vs. no)	-0.431	-4.122 to 3.260	-0.087	-0.376 to 0.202
Non-lacunar infarcts (present vs. absent)	3.279	-2.237 to 8.795	-0.030	-0.471 to 0.410

B: *regression coefficient.* ***95% CI:*** *95% confidence interval.*
Analysis of age was adjusted for sex, analysis of sex was adjusted for age.
All other analyses were adjusted for age and sex, using multiple linear regression.
a: p < 0.05, b: p < 0.01; all other values: p > 0.05

Microbleeds

CVR1 and CVR2 were lower in patients with microbleeds than in patients without microbleeds. The difference in CVR2 was statistically significant, the difference in CVR1 was not statistically significant (figure 2 and table 3).

A total of 41 microbleeds was scored in 17 patients, the outlier excluded. Of these 41 microbleeds, 38 were lobar microbleeds, 2 were located infratentorial and 1 deep. Linear regression of the number of microbleeds, adjusted for age and sex, showed a negative association with CVR1 (regression coefficient B=-0.538, 95% CI -1.800 to 0.724) and with the CVR2 (B=-0.056, 95% CI -0.453 to 0.042), although these were not statistically significant. Additional adjustment for use of anticoagulant or antihypertensive medication did not change the results (data not shown).

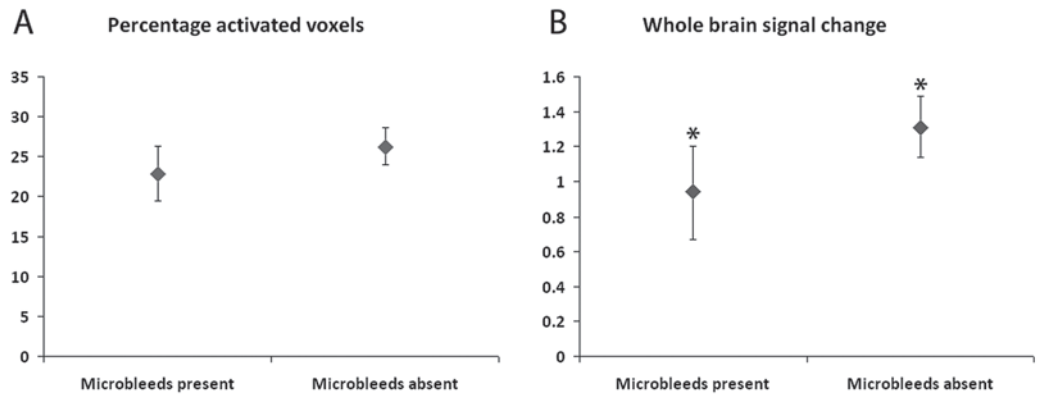

Figure 2 | [**A**] *Shows the percentage of activated voxels (CVR1) with 95% confidence interval in patients with and without microbleeds, adjusted for age, sex, systolic and diastolic blood pressure and non-lacunar infarcts.* [**B**] *Shows the significant difference in percentage whole brain signal change (CVR2) with 95% confidence interval between patients with and without microbleeds, adjusted for age, sex, systolic and diastolic blood pressure and non-lacunar infarcts.* p < 0.05*

Lacunar infarcts and WML

No significant differences in CVR1 or CVR2 were observed between patients with and without lacunar infarcts or between patients with and without severe WML (table 3). Increase in WML volume per mL also showed no significant association with CVR1 (B=0.141, 95% CI -0.234 to 0.516) or with CVR2 (B=0.001, 95% CI -0.028 to 0.031), adjusted for age and sex.

Table 3 **Mean percentages activated voxels (CVR1) and whole brain signal change (CVR2) for patients with and without microbleeds, patients with and without lacunar infarcts and patients in the upper quartile and the lower three quartiles of WML**

	Percentage activated voxels		Whole brain signal change	
	mean (95% CI)	*p*-value	mean (95% CI)	*p*-value
Microbleeds				
Model 1				
Present	23.6 (20.6 to 26.5)		1.00 (0.78 to 1.23)	
Absent	26.1 (23.8 to 28.4)		1.31 (1.14 to 1.49)	
Difference	-2.5 (-6.3 to 1.2)	0.180	-0.32 (-0.60 to -0.03)	0.033
Model 2				
Present	23.6 (20.6 to 26.6)		0.97 (0.75 to 1.19)	
Absent	26.1 (23.8 to 28.4)		1.33 (1.16 to 1.50)	
Difference	-2.5 (-6.3 to 1.3)	0.199	-0.36 (-0.64 to -0.07)	0.014
Lacunar infarcts				
Model 1				
Present	24.3 (19.8 to 28.8)		1.07 (0.71 to 1.42)	
Absent	25.3 (23.3 to 27.3)		1.23 (1.07 to 1.39)	
Difference	-1.0 (-6.1 to 4.0)	0.678	-0.17 (-0.56 to 0.23)	0.401
Model 2				
Present	23.1 (18.5 to 27.6)		1.01 (0.66 to 1.36)	
Absent	25.6 (23.6 to 27.6)		1.24 (1.09 to 1.40)	
Difference	-2.5 (-7.7 to 2.6)	0.325	-0.24 (-0.63 to 0.16)	0.241
White matter lesions				
Model 1				
Upper quartile	26.9 (22.4 to 31.5)		1.26 (0.90 to 1.62)	
Lower three quartiles	24.7 (22.7 to 26.7)		1.19 (1.03 to 1.35)	
Difference	2.2 (-2.9 to 7.4)	0.388	0.08 (-0.33 to 0.49)	0.706
Model 2				
Upper quartile	26.5 (21.8 to 31.2)		1.25 (0.88 to 1.62)	
Lower three quartiles	24.8 (22.8 to 26.8)		1.19 (1.03 to 1.35)	
Difference	1.7 (-3.6 to 7.0)	0.531	0.06 (-0.36 to 0.47)	0.783

95% CI: *95% confidence interval.* ***Model 1:*** *adjusted for age and sex,* ***Model 2:*** *additionally adjusted for systolic blood pressure, diastolic blood pressure and non-lacunar infarcts*

Discussion

In a population of patients with atherosclerotic disease, we found that the cerebrovascular reactivity, measured with BOLD-fMRI at 7 Tesla, was significantly decreased in patients with one or more microbleeds compared to patients without microbleeds, independent of age, sex, systolic and diastolic blood pressure, and non-lacunar infarcts. The presence of lacunar infarcts and greater WML load was not significantly associated with decreased CVR in this study.

To our knowledge, this is the first study assessing CVR by means of BOLD-fMRI at 7 Tesla and its relationship with microbleeds. Previous studies investigating CVR in relation to lacunar infarcts and WML often used transcranial Doppler ultrasonography,[17-20] with some finding decreased CVR in patients with lacunar infarcts,[14,20] and others in subjects with WML,[17,19] whereas another study could not replicate these findings.[18] A major drawback of transcranial Doppler ultrasonography is that it measures blood flow velocity in the middle cerebral artery, and therefore all results are based on reactivity of the middle cerebral artery and its supplying arteries. This makes it difficult to apply the findings to small vessels in the brain. The advantage of BOLD-fMRI is that CVR can be measured at tissue-level, as both small and large vessels contribute to the fMRI signal. BOLD-fMRI at 7 Tesla will provide information about all vessels in the brain, making it an interesting method to investigate the relation between CVR and lacunar infarcts, WML and microbleeds.

With the interpretation of the BOLD-fMRI data, it should be noted that it is a relative measure and gives no absolute values. Several factors can influence the baseline BOLD signal and the change in activation, such as age, sex and blood pressure, as shown in this study. To minimize the effect of these factors on the results of our study, we adjusted for the effects age, sex, blood pressure and presence of non-lacunar infarcts in all analyses. This makes it possible to differentiate between the effect of presence of microbleeds, lacunar infarcts or WML, and the effects of age, sex, blood pressure and non-lacunar infarcts on change in activation.

In this study we used two measures of CVR: the percentage of activated voxels (CVR1) and the whole brain signal change (CVR2). These measures partly depend on each other, as is shown by the moderate correlation between CVR1 and CVR2. However, the two measures can still be used to differentiate between a difference in the activated area in the brain and a difference in the degree of activation. A smaller area of vascular reactivity in the brain can be represented by a significantly lower percentage of activated voxels (CVR1). This can also result in a lower whole brain signal change (CVR2), if the signal change per voxel is also lower or similar. However, if the area of reactivity is smaller but the degree of reactivity is higher, this can lead to a lower CVR1 without a difference in CVR2. If, on the other hand, the area of vascular reactivity is the same between patients but the degree of reactivity is lower, this would be represented by a lower whole brain signal change (CVR2), without a difference in the area of activation (CVR1). Therefore, use of the two measure results in more detailed information about CVR than use of either one of the two measures alone.

Our finding that CVR was reduced in patients with microbleeds may support the hypothesis that changes in the vessel wall in patients with microbleeds lead to stiffening of the vessels and impairment of CVR. The few pathological studies done in patients with microbleeds support the idea that changes in the vessel wall are important in the development of microbleeds. In one pathology study done in patients with cerebral amyloid angiopathy, patients with a high microbleed count showed thicker vessel walls than patients with low microbleed counts.[29] Another study in patients with Alzheimer's disease found presence of ß-amyloid and a relative acellularity of the muscularis layer in the arterioles involving the microbleeds.[30] In vitro studies showed that ß-amyloid is particularly toxic to vascular smooth muscle cells,[31] which may explain the acellularity of the muscularis layer, leading in turn to impaired CVR.

We did not find an association between lacunar infarcts or WML with CVR, whereas previous studies using transcranial Doppler ultrasonography found a decrease in CVR in patients with lacunar infarcts[14,20] and in patients with WML.[17,19] The difference between our results and other studies may be due to the different methods used to assess CVR. Lacunar infarcts and WML might lead to a change in reactivity of the MCA, which is measured with transcranial Doppler ultrasonography. This change in reactivity could be due to concomitant large vessel disease.[18] However, BOLD-fMRI measures CVR over the whole brain, including small vessels.

Another possible explanation why we did not find a relation between lacunar infarcts and CVR, is the relatively small number of patients with lacunar infarcts within our study population. The differences in CVR between patients with and without lacunar infarcts might be too subtle to detect in a small population. However, with transcranial Doppler a difference was found in a group of only ten patients with lacunar infarcts.[20] Therefore, it could be expected that with the more detailed measurement of CVR by means of BOLD-fMRI at 7 Tesla a difference in CVR between patients with and without lacunar infarcts can be detected with a relatively small number of patients. However, studies with larger study populations are needed to replicate the findings of our study.

Assuming enough power to detect changes within our study population, it is interesting that CVR was impaired in patients with microbleeds but not in patients with lacunar infarcts or WML, although previous studies showed associations between these lesions[12] and suggested a similar pathology.[13] However, one hypothesis about the etiology of microbleeds is that microbleeds at different locations are associated with different pathological changes. Infratentorial and deep located microbleeds may be associated with hypertensive vasculopathy, whereas lobar microbleeds may be associated with cerebral amyloid angiopathy.[12] In addition, one study showed that lacunar infarcts and WML were associated with microbleeds in a deep or infratentorial location but not in a lobar location.[32] In our study, of the 41 microbleeds detected 38 were in lobar locations. This could suggest that ß-amyloid in the vessel walls resulted in impaired CVR, and may also explain why no association between CVR and lacunar infarcts or WML was found. Possibly, the pathologic changes underlying lacunar infarcts and WML are different from the changes underlying lobar microbleeds. Also, the use of 7T MRI resulted in a high prevalence of microbleeds in our relatively young study population. The advantages in detection of microbleeds at 7T can be beneficial to investigate their relation with subtle changes in CVR,[24] whereas it is possible that the prevalence of lacunar infarcts or the WML volume in our study population was too low to detect small effects if present.

A limitation of the study is the cross-sectional design. As a result, we cannot discern cause from consequence and do not know if CVR changed after the occurrence of microbleeds or that CVR was already impaired prior to the occurrence of microbleeds. Since changes in the vessel wall are thought to be the underlying cause of microbleeds, we hypothesize that CVR was already impaired prior to the occurrence of microbleeds. Also, our population consisted of patients with vascular risk factors and vascular disease, and we thus do not know to what extent our findings can be generalized to a healthy population.

In conclusion, in patients with atherosclerotic disease the presence of microbleeds, but not lacunar infarcts or WML, was associated with an impaired CVR at 7T MRI. Future studies should determine whether these results hold in larger study samples and also whether the association between microbleeds and CVR can be found in other study populations.

Chapter 07 Microbleeds, lacunar infarcts, white matter lesions and cerebrovascular reactivity - a 7T study

References

1 Futrell N. Lacunar infarction: embolism is the key. *Stroke* 2004;35:1778-1779.
2 Norrving B. Lacunar infarction: embolism is the key: against. *Stroke* 2004;35:1779-1780.
3 O'Sullivan M. Leukoaraiosis. *Pract Neurol* 2008;8:26-38.
4 Pantoni L. Pathophysiology of age-related cerebral white matter changes. *Cerebrovasc Dis* 2002;13:7-10.
5 Wardlaw JM. What causes lacunar stroke? *J Neurol Neurosurg Psychiatry* 2005;76:617-619.
6 Fisher CM. Lacunes: small, deep cerebral infarcts. 1965. *Neurology* 1998;50:841.
7 Lammie GA, Brannan F, Slattery J, Warlow C. Nonhypertensive cerebral small-vessel disease. An autopsy study. *Stroke* 1997;28:2222-2229.
8 Hassan A, Hunt BJ, O'Sullivan M, Parmar K, Bamford JM, Briley D, Brown MM, Thomas DJ, Markus HS. Markers of endothelial dysfunction in lacunar infarction and ischaemic leukoaraiosis. *Brain* 2003;126:424-432.
9 Wardlaw JM, Sandercock PA, Dennis MS, Starr J. Is breakdown of the blood-brain barrier responsible for lacunar stroke, leukoaraiosis, and dementia? *Stroke* 2003;34:806-812.
10 Wardlaw JM, Doubal F, Armitage P, Chappell F, Carpenter T, Munoz MS, Farrall A, Sudlow C, Dennis M, Dhillon B. Lacunar stroke is associated with diffuse blood-brain barrier dysfunction. *Ann Neurol* 2009;65:194-202.
11 Fazekas F, Kleinert R, Roob G, Kleinert G, Kapeller P, Schmidt R, Hartung HP. Histopathologic analysis of foci of signal loss on gradient-echo T2*-weighted MR images in patients with spontaneous intracerebral hemorrhage: evidence of microangiopathy-related microbleeds. *AJNR Am J Neuroradiol* 1999;20:637-642.
12 Greenberg SM, Vernooij MW, Cordonnier C, Viswanathan A, Al-Shahi SR, Warach S, Launer LJ, Van Buchem MA, Breteler MM. Cerebral microbleeds: a guide to detection and interpretation. *Lancet Neurol* 2009;8:165-174.
13 Wardlaw JM, Lewis SC, Keir SL, Dennis MS, Shenkin S. Cerebral microbleeds are associated with lacunar stroke defined clinically and radiologically, independently of white matter lesions. *Stroke* 2006;37:2633-2636.
14 Molina C, Sabin JA, Montaner J, Rovira A, Abilleira S, Codina A. Impaired cerebrovascular reactivity as a risk marker for first-ever lacunar infarction: A case-control study. *Stroke* 1999;30:2296-2301.
15 Goode SD, Krishan S, Alexakis C, Mahajan R, Auer DP. Precision of cerebrovascular reactivity assessment with use of different quantification methods for hypercapnia functional MR imaging. *Am J Neuroradiol* 2009;30:972-977.
16 Kassner A, Winter JD, Poublanc J, Mikulis DJ, Crawley AP. Blood-oxygen level dependent MRI measures of cerebrovascular reactivity using a controlled respiratory challenge: reproducibility and gender differences. *J Magn Reson Imaging* 2010;31:298-304.
17 Bakker SL, De Leeuw FE, De Groot JC, Hofman A, Koudstaal PJ, Breteler MM. Cerebral vasomotor reactivity and cerebral white matter lesions in the elderly. *Neurology* 1999;52:578-583.
18 Birns J, Jarosz J, Markus HS, Kalra L. Cerebrovascular reactivity and dynamic autoregulation in ischaemic subcortical white matter disease. *J Neurol Neurosurg Psychiatry* 2009;80:1093-1098.
19 Fu JH, Lu CZ, Hong Z, Dong Q, Ding D, Wong KS. Relationship between cerebral vasomotor reactivity and white matter lesions in elderly subjects without large artery occlusive disease. *J Neuroimaging* 2006;16:120-125.
20 Immink RV, van Montfrans GA, Stam J, Karemaker JM, Diamant M, van Lieshout JJ. Dynamic cerebral autoregulation in acute lacunar and middle cerebral artery territory ischemic stroke. *Stroke* 2005;36:2595-2600.
21 Hund-Georgiadis M, Zysset S, Naganawa S, Norris DG, von Cramon DY. Determination of cerebrovascular reactivity by means of FMRI signal changes in cerebral microangiopathy: a correlation with morphological abnormalities. *Cerebrovasc Dis* 2003;16:158-165.
22 Yacoub E, Shmuel A, Pfeuffer J, Van De Moortele PF, Adriany G, Andersen P, Vaughan JT, Merkle H, Ugurbil K, Hu X. Imaging brain function in humans at 7 Tesla. *Magn Reson Med* 2001;45:588-594.
23 Simons PC, Algra A, van de Laak MF, Grobbee DE, van der Graaf Y. Second manifestations of ARTerial disease (SMART) study: rationale and design. *Eur J Epidemiol* 1999;15:773-781.
24 Conijn MM, Geerlings MI, Luijten PR, Zwanenburg JJ, Visser F, Biessels GJ, Hendrikse J. Visualization of cerebral microbleeds with dual-echo T2*-weighted magnetic resonance imaging at 7.0 T. *J Magn Reson Imaging* 2010;32:52-59.
25 Gregoire SM, Chaudhary UJ, Brown MM, Yousry TA, Kallis C, Jager HR, Werring DJ. The Microbleed Anatomical Rating Scale (MARS): reliability of a tool to map brain microbleeds. *Neurology* 2009;73:1759-1766.
26 Anbeek P, Vincken KL, van Osch MJ, Bisschops RH, van der Grond J. Automatic segmentation of different-sized white matter lesions by voxel probability estimation. *Med Image Anal* 2004;8:205-215.
27 Anbeek P, Vincken KL, van Osch MJ, Bisschops RH, van der Grond J. Probabilistic segmentation of white matter lesions in MR imaging. *Neuroimage* 2004;21:1037-1044.
28 Appelman AP, Vincken KL, van der GY, Vlek AL, Witkamp TD, Mali WP, Geerlings MI. White matter lesions and lacunar infarcts are independently and differently associated with brain atrophy: the SMART-MR study. *Cerebrovasc Dis* 2010;29:28-35.
29 Greenberg SM, Nandigam RN, Delgado P, Betensky RA, Rosand J, Viswanathan A, Frosch MP, Smith EE. Microbleeds versus macrobleeds: evidence for distinct entities. *Stroke* 2009;40:2382-2386.
30 Schrag M, McAuley G, Pomakian J, Jiffry A, Tung S, Mueller C, Vinters HV, Haacke EM, Holshouser B, Kido D, Kirsch WM. Correlation of hypointensities in susceptibility-weighted images to tissue histology in dementia patients with cerebral amyloid angiopathy: a postmortem MRI study. *Acta Neuropathol* 2009.
31 Davis J, Cribbs DH, Cotman CW, Van Nostrand WE. Pathogenic amyloid beta-protein induces apoptosis in cultured human cerebrovascular smooth muscle cells. *Amyloid* 1999;6:157-164.
32 Vernooij MW, Van der Lugt A, Ikram MA, Wielopolski PA, Niessen WJ, Hofman A, Krestin GP, Breteler MM. Prevalence and risk factors of cerebral microbleeds: the Rotterdam Scan Study. *Neurology* 2008;70:1208-1214.

CHAPTER 08

General discussion

Chapter 08 General discussion

General discussion

The studies described in this thesis explored several potential imaging biomarkers of early stages of cerebral small vessel disease with 7 Tesla MRI. In this chapter we will consider the imaging biomarkers and discuss the implications of 7 Tesla MRI for clinical research.

Potential imaging biomarkers of cerebral small vessel disease

Cerebral small vessel disease is hypothesized to be caused by changes in the small, perforating arteries in the brain,[1-3] and these perforating arteries are a logical first target to explore as an imaging biomarker of cerebral small vessel disease. Previous studies have shown that perforating arteries from the anterior and medial cerebral artery can be visualized with 7 Tesla MRI.[5,6] In chapter 3 we investigated the perforating arteries from the posterior communicating artery, the anterior choroidal artery and the P1-segment of the posterior cerebral artery at 7T. With this study we visualized the perforating arteries originating from the posterior communicating artery, the anterior choroidal artery and the P1-segment of the posterior cerebral artery for the first time in vivo without the use of contrast agents. These perforating arteries are important for the blood supply to the deep brain structures; the location where lacunar infarcts, white matter lesions and microbleeds are most often found. The presence of a (large) posterior communicating artery has been shown to be protective against ischemic lesions of the brain.[6-8] The presence of large perforating arteries from the posterior communicating artery may explain this protective effect, and could also play a protective role in cerebral small vessel disease. The visualization of perforating arteries in patients with cerebral small vessel disease compared to controls can give valuable information on the extent to which these arteries are involved in cerebral small vessel disease. Absence of perforating arteries, a decreased number, or small perforating arteries may indicate the existence of cerebral small vessel disease and thus an increased risk of lacunar infarcts, white matter lesions or microbleeds.

Endothelial dysfunction is thought to play a role in the pathophysiology of cerebral small vessel disease.[9-12] As microbleeds are caused by leakage of red blood cells from small blood vessels in the brain,[10] the presence of very small microbleeds could be one of the earliest manifestations of cerebral small vessel disease. To be able to detect very small microbleeds, a very sensitive detection method is needed. Among others, field strength and echo time are important parameters for the visualization of microbleeds.[13,14] In chapter 4 we showed that the use of a dual echo T2*-weighted sequence at 7T combines the advantages of a short and a long echo time for the visualization of microbleeds. The short echo time is beneficial to distinguish microbleeds from other structures with a high susceptibility, and with the long echo time a larger number of microbleeds can be detected. When we compared the dual echo T2*-weighted imaging at 7T with high resolution 3D T2*-weighted imaging at 1.5T, we found that the dual echo T2*-weighted imaging at 7T resulted in better and more reliable detection of microbleeds (Chapter 5). The prevalence of microbleeds in our study population was very high (50%) on 7T, whereas on 1.5T the prevalence was 21%, which is comparable to estimates from other studies at 1.5T.[15] Also the number of microbleeds detected was higher at 7T. This indicates that more microbleeds can be detected with dual echo T2*-weighted imaging at 7T. As such, it could be a very useful early marker of cerebral small vessel disease. Future studies investigating microbleeds should use a sensitive detection method at high field strength, as the differences in prevalence between 1.5T and 7T are large. The majority of existing knowledge of microbleeds results from 1.5T studies, and the findings of our study suggest that the conclusions from 1.5T research are probably based on an underestimation of the prevalence and number of microbleeds. The question is whether these conclusions of 1.5T studies hold when the studies are repeated at higher field strengths.

As cerebral small vessel disease and iron deposition in the brain are both associated with endothelial dysfunction,[9-12,16] we investigated brain iron deposition as a possible early marker of cerebral small vessel disease (Chapter 6). We found that lacunar infarcts, but not white matter lesions or microbleeds, were associated with significantly more iron deposition in the caudate nucleus. The differences in association between lacunar infarcts, white

matter lesions and microbleeds might be due to the location of the lesions. As lacunar infarcts are mainly located in or near the basal ganglia, this may follow alterations in the perforating arteries supplying the basal ganglia. White matter lesions and microbleeds are located primarily in the brain parenchyma and may result from changes in perforating arteries supplying the periventricular and deep white matter. As the differences in iron deposition are not consistent between lacunar infarcts, white matter lesions and microbleeds, brain iron is probably not very useful as an early imaging biomarker. Furthermore, our study was a cross-sectional study and therefore we do not know if iron deposition occurs before the occurrence of lacunar infarcts, or that they occur simultaneously. However, although iron deposition is probably not very useful as an early marker, the relation between iron deposition and cerebral small vessel disease can provide more insight into the pathophysiology of cerebral small vessel disease. Therefore, longitudinal studies are needed to further investigate this relation.

Besides increased permeability of the vessel wall, also the vascular reactivity may be altered due to changes in the vessel wall in patients with cerebral small vessel disease. In chapter 7 we investigated the relation between lacunar infarcts, white matter lesions, microbleeds and cerebrovascular reactivity. A decreased vascular reactivity in the brain was only found in patients with microbleeds, but not in patients with lacunar infarcts or white matter lesions. Again the inconsistency of the relation with cerebrovascular reactivity with lacunar infarcts, white matter lesions and microbleeds makes vascular reactivity less suitable as an imaging biomarker for cerebral small vessel disease. However, it does give interesting information about possible differences in pathophysiology of microbleeds, lacunar infarcts and white matter lesions. A possible explanation for the difference is that lobar microbleeds are associated with cerebral amyloid angiopathy, and not with lacunar infarcts or white matter lesions.[15,17] In our study most microbleeds were located in lobar locations, and therefore we hypothesized that ß-amyloid in the vessel walls in patients with lobar microbleeds resulted in impaired cerebrovascular reactivity. Possibly, the pathologic changes underlying lacunar infarcts and white matter lesions are different from the changes underlying lobar microbleeds.

In conclusion, perforating arteries and microbleeds can be promising early biomarkers of cerebral small vessel disease. Iron deposition and cerebrovascular reactivity show less potential as early biomarkers, but can provide more insight in the pathophysiology of cerebral small vessel disease.

7 Tesla MRI: implications for clinical research

The use of 7 Tesla MRI reveals potential early imaging biomarkers for cerebral small vessel disease. Although ultra-high field strength MRI brings many benefits for clinical research, in this case for the imaging of cerebral small vessel disease, it also brings new challenges. Technically, imaging at 7 Tesla suffers from field inhomogeneities caused by differences in magnetic susceptibility between air and brain tissue, introducing image distortions or even loss of signal at some points.[18] Another challenge is the non-uniformity in the radiofrequency fields, resulting in uneven distribution of contrast and signal-to-noise ratio. Also the absorption of radiofrequency energy, which can cause heating of the tissues, is unevenly distributed and increased at 7T. This imposes strict limits are set for the radiofrequency power used at 7T which may reduce the degrees of freedom to tune MR pulse sequences for optimal signal/contrast to noise per unit of time. To meet these technical challenges, continuous development of various technical innovations takes place.

The technical challenges are a complicating factor for clinical research, as the quality of the MRI sequences used in the MR protocol is not constant. For example, the field inhomogeneities depend on several factors, such as the shape of the head of the patient, causing variation in quality of the scans between patients. The same sequences can result in different quality of scans between patients, due to extraneous factors. However, also the technical innovations to improve these difficulties bring challenges for clinical research. When sequences within the scan protocol can be improved by implementation of new or improved features, the question is whether to keep the scan protocol the same or to implement the new features. Not implementing will keep the scan technique as

constant as possible over the study, whereas implementing the new features will result in better scans, but with less comparability in scan quality between patients scanned before and after the implementation. As 7T MRI is a quickly developing field of imaging, new developments will be achieved during a clinical study and keeping the original scan protocol constant can result in outdated scans when the study is finished. Therefore, a trade-off needs to be found between implementing features that significantly improve the quality of the scans and keeping the scans technically as equal as possible between patients. The continuous technical developments make the 7T at this moment less suitable for large longitudinal studies, as for longitudinal studies more optimized sequences with constant quality over time are needed.

Another difficulty in clinical research at 7T are the exclusion criteria. For MRI at lower field strengths, elaborate research has been done on the safety of implants, materials, and medical devices. However, for 7T safety testing has not been performed yet. Therefore, at this moment mainly all implants, materials and medical devices count as exclusion criteria for clinical studies. Especially in the studies with atherosclerotic patients, but also in clinical studies including older patients, many patients will be excluded because of implants or operations, such as stents, carotid artery bypass operations, tooth- or joint-prostheses. Safety testing at 7T has recently started and will probably show results in the near future; however, up till then it will be more difficult and time-consuming to perform large clinical studies at 7T compared to lower field strengths, as many patients will be excluded due to the strict safety regulations.

Experience with adverse effects of the ultra-high magnetic field on patients is limited. For the 7T studies described in this thesis, patients underwent both a 1.5T and a 7T scan on the same day. At the end of the 7T scan, the patients were asked to fill in a questionnaire about their experiences. Most patients experienced no large difference between the 1.5T and 7T scan. Of the patients that did experience a difference, almost half described more noise during the 7T scan, whereas the other half experienced less noise during the 7T scan and found it even more comfortable compared to the 1.5T scan. Very few patients reported adverse events; only a few reported dizziness or described a feeling of getting into the scanner around a curve in stead of a straight line. These adverse affects were all temporary and none of them prevented the patients from fulfilling the complete scan. Also for other studies it has been described that 7T was well tolerated by the majority of the subjects.[19] Therefore, adverse effects of the ultra-high magnetic field appear to be no limitation for clinical research at 7T.

Overall it can be stated that the use of 7 Tesla MRI results in many benefits for new or improved scans. As is usually the case with new technical developments, also 7T shows some challenges that should be taken into account when using it for clinical research. As 7T shows to be hardly any more aggravating for patients than 1.5T MRI, it appears to be very suitable to use for innovative clinical research.

Future directions

This thesis is the first in the Netherlands that is based on clinical studies at 7 Tesla MRI. The results look promising, as we found potential early biomarkers for cerebral small vessel disease that can be very well visualized at 7T. However, before conclusions can be drawn, more and larger studies are needed to investigate this further.
7 Tesla MRI shows many benefits for the detailed imaging of brain structures and brain function and is very well tolerated by patients. As the availability of 7 Tesla systems increases, the use of 7T for clinical research will also increase. This will improve our knowledge of neurologic and neurodegenerative diseases. However, at this moment the 7T MRI is still an experimental system and there are some hurdles that need to be taken before it can be used in clinical practice.

Chapter 08 General discussion

References

1 Fisher CM. The arterial lesions underlying lacunes. *Acta Neuropathol* 1968;12:1-15.
2 Fisher CM. Lacunes: small, deep cerebral infarcts. 1965. *Neurology* 1998;50:841.
3 Lammie GA, Brannan F, Slattery J, Warlow C. Nonhypertensive cerebral small-vessel disease. An autopsy study. *Stroke* 1997;28:2222-2229.
4 Hendrikse J, Zwanenburg JJ, Visser F, Takahara T, Luijten P. Noninvasive depiction of the lenticulostriate arteries with time-of-flight MR angiography at 7.0 T. *Cerebrovasc Dis* 2008;26:624-629.
5 Kang CK, Park CW, Han JY, Kim SH, Park CA, Kim KN, Hong SM, Kim YB, Lee KH, Cho ZH. Imaging and analysis of lenticulostriate arteries using 7.0-Tesla magnetic resonance angiography. *Magn Reson Med* 2009;61:136-144.
6 Chuang YM, Liu CY, Pan PJ, Lin CP. Posterior communicating artery hypoplasia as a risk factor for acute ischemic stroke in the absence of carotid artery occlusion. *J Clin Neurosci* 2008;15:1376-1381.
7 Jongen JC, Franke CL, Ramos LM, Wilmink JT, van Gijn. Direction of flow in posterior communicating artery on magnetic resonance angiography in patients with occipital lobe infarcts. *Stroke* 2004;35:104-108
8 Schomer DF, Marks MP, Steinberg GK, Johnstone IM, Boothroyd DB, Ross MR, Pelc NJ, Enzmann DR. The anatomy of the posterior communicating artery as a risk factor for ischemic cerebral infarction. *N Engl J Med* 1994;330:1565-1570.
9 Hassan A, Hunt BJ, O'Sullivan M, Parmar K, Bamford JM, Briley D, Brown MM, Thomas DJ, Markus HS. Markers of endothelial dysfunction in lacunar infarction and ischaemic leukoaraiosis. *Brain* 2003;126:424-432.
10 Wardlaw JM, Sandercock PA, Dennis MS, Starr J. Is breakdown of the blood-brain barrier responsible for lacunar stroke, leukoaraiosis, and dementia? *Stroke* 2003;34:806-812.
11 Wardlaw JM, Doubal F, Armitage P, Chappell F, Carpenter T, Munoz MS, Farrall A, Sudlow C, Dennis M, Dhillon B. Lacunar stroke is associated with diffuse blood-brain barrier dysfunction. *Ann Neurol* 2009;65:194-202.
12 Stevenson SF, Doubal FN, Shuler K, Wardlaw JM. A systematic review of dynamic cerebral and peripheral endothelial function in lacunar stroke versus controls. *Stroke* 2010;41:e434-e442.
13 Haacke EM, Mittal S, Wu Z, Neelavalli J, Cheng YC. Susceptibility-weighted imaging: technical aspects and clinical applications, part 1. *AJNR Am J Neuroradiol* 2009;30:19-30.
14 Mittal S, Wu Z, Neelavalli J, Haacke EM. Susceptibility-weighted imaging: technical aspects and clinical applications, part 2. *AJNR Am J Neuroradiol* 2009;30:232-252.
15 Vernooij MW, van der Lugt A, Ikram MA, Wielopolski PA, Niessen WJ, Hofman A, Krestin GP, Breteler MM. Prevalence and risk factors of cerebral microbleeds: the Rotterdam Scan Study. *Neurology* 2008;70:1208-1214.
16 Ke Y, Qian ZM. Brain iron metabolism: neurobiology and neurochemistry. *Prog Neurobiol* 2007;83:149-173.
17 Greenberg SM, Vernooij MW, Cordonnier C, Viswanathan A, Al-Shahi SR, Warach S, Launer LJ, Van Buchem MA, Breteler MM. Cerebral microbleeds: a guide to detection and interpretation. *Lancet Neurol* 2009;8:165-174.
18 Zwanenburg JJ. Magnetic Resonance Imaging bij ultra-hoge veldsterkte (7 Tesla). *Nederlands Tijdschrift voor Natuurkunde* 2008:194-198.
19 Theysohn JM, Maderwald S, Kraff O, Moenninghoff C, Ladd ME, Ladd SC. Subjective acceptance of 7 Tesla MRI for human imaging. *MAGMA* 2008;21:63-72.

CHAPTER 09

Summary
Nederlandse samenvatting

Summary

Cerebral small vessel disease is a term often used to refer to lacunar infarcts and white matter lesions; ischemic lesions that are thought to be caused by changes in the small vessels of the brain. Recently, microhemorrhages or microbleeds are increasingly recognized as another manifestation of cerebral small vessel disease. These lesions are commonly found on MRI scans in the general elderly population and thought to be associated with an increased risk of stroke, cognitive impairment and death. The small, perforating arteries in the brain are hard to visualize in vivo. As a result, lacunar infarcts, white matter lesions and microbleeds are adopted as marker of cerebral small vessel disease, and cerebral small vessel disease has become a synonym of brain parenchyma lesions. With the introduction of 7 Tesla MRI for clinical research, there are new opportunities to visualize the small, perforating arteries in the brain and to identify earlier stages of cerebral small vessel disease. The main aim of this thesis was to explore imaging biomarkers of early stages of cerebral small vessel disease with 7 Tesla MRI.

Cerebral small vessel disease and prognosis in atherosclerotic patients

Lacunar infarcts and white matter lesions increase the risk of stroke, cognitive decline and dementia in the general population. Patients with atherosclerosis have a high risk of vascular events. It is not known whether the presence of lacunar infarcts or white matter lesions imposes an additional risk of death or vascular events on top of preexistent vascular disease. The clinical relevance of lacunar infarcts and white matter lesions in patients with atherosclerosis is important, as atherosclerosis is still an increasing problem in the world and white matter lesions and silent infarcts are common in patients with atherosclerosis. We found that the presence of one or more lacunar infarcts on MRI, whether they were symptomatic or asymptomatic, increased the risk of vascular as well as non-vascular death, independent of age, sex, vascular risk factors, non-lacunar infarcts and white matter lesions (*chapter 2*). White matter lesions increased the risk of vascular death and the risk of ischemic stroke, independent of the same factors and independent of the presence of lacunar infarcts. These results show the importance of lacunar infarcts and white matter lesions for the prognosis of patients with atherosclerosis.

Cerebral small vessel disease and imaging biomarkers at 7 Tesla MRI

As cerebral small vessel disease is hypothesized to be caused by changes in the small perforating arteries in the brain, these perforating arteries are a logical first target to explore as an imaging biomarker of cerebral small vessel disease. Previous studies have shown that perforating arteries from the anterior and medial cerebral artery can be visualized with 7 Tesla MRI. In *chapter 3* we showed the capacity of time-of-flight MR angiography at 7T to show the perforating arteries originating from the posterior communicating artery and from the P1-segment of posterior cerebral artery, without the use of contrast agents. The results show that the presence of a perforating artery from the posterior communicating artery is associated with the diameter of the posterior communicating artery. The non-invasive assessment of perforating arteries in future studies may increase our understanding of infarcts in the deep brain structures supplied by these arteries.

Endothelial dysfunction is thought to play a role in the pathophysiology of cerebral small vessel disease. Microbleeds are caused by leakage of red blood cells from small blood vessels in the brain. The presence of very small microbleeds could be one of the earliest manifestations of cerebral small vessel disease. Microbleeds are paramagnetic and therefore induce a susceptibility effect on the MRI scan. Echo time and field strength are two factors that influence the susceptibility effect and therefore also influence the visualization of microbleeds. In *chapter 4* we investigated the use of a dual echo T2*-weighted sequence at 7T for the visualization of microbleeds. At 7T it is possible to visualize microbleeds already at a short echo time. The use of a short echo time is beneficial to distinguish microbleeds from other structures with a high susceptibility. The use of a long echo time results in detection of a larger number of microbleeds. With a dual echo sequence the advantages of a short and a long

Chapter 09 Summary

echo time can be combined. In current studies investigating microbleeds, 3D T2*-weighted imaging at 1.5T is most often used for the detection of microbleeds. Comparing the dual echo T2*-weighted imaging at 7T with high resolution 3D T2*-weighted imaging at 1.5T, we found that the dual echo T2*-weighted imaging at 7T resulted in detection of microbleeds in more patients and also detection of a higher number of microbleeds. Furthermore, the detection of microbleeds was more reliable at 7T (*chapter 5*).

Iron is important for metabolic processes of the brain and with normal aging, progressive iron deposition in the brain occurs. Outside the brain, iron is thought to play a role in the pathogenesis of atherosclerosis. It is stated that stored tissue iron may be an important determinant for the development of atherosclerosis. As lacunar infarcts, white matter lesions and microbleeds all involve increased permeability of cerebral small vessels, it is possible that this increased permeability could lead to increased iron deposition in the basal ganglia as a secondary consequence. As the use of ultra-high field strengths, such as 7 Tesla, results in a dramatic increase in susceptibility effect, sensitivity and resolution, this can be very useful to detect subtle change in iron concentration. With 7 Tesla MRI we investigated the determinants of brain iron deposition in the brain and iron deposition as a possible early marker of cerebral small vessel disease (*chapter 6*). T2*-values of the putamen, globus pallidus and caudate nucleus were used as a measure of iron deposition in the basal ganglia. The phase images showed characteristic phase changes suggestive of iron in the basal ganglia, indicating that the decrease in T2* found in this study was due to iron deposition. Older age and male sex were associated with increased iron deposition in one or more basal ganglia. Lacunar infarcts, but not white matter lesions or microbleeds, were associated with significantly more iron deposition, independent of age and sex.

The increased permeability of the perforating arteries may lead to entry of serum components into the vessel wall, causing thickening, inflammation and disorganization of the vessel wall. These changes of the vessel wall may alter the vascular reactivity in patients with cerebral small vessel disease. Cerebrovascular reactivity can be measured with blood oxygenation level-dependent functional MRI (BOLD-fMRI). With increasing field strength, the sensitivity, specificity and contrast of the BOLD-response increases. In *chapter 7* we investigated the relation between lacunar infarcts, white matter lesions, microbleeds and cerebrovascular reactivity, measured with BOLD-fMRI at 7 Tesla MRI. A decreased vascular reactivity in the brain was found in patients with microbleeds independent of age, sex, systolic and diastolic blood pressure and non-lacunar infarcts. In patients with lacunar infarcts or white matter lesions no significant association with cerebrovascular reactivity was found. Our finding that cerebrovascular reactivity was reduced in patients with microbleeds may support the hypothesis that changes in the vessel wall in patients with microbleeds lead to stiffening of the vessels and impairment of the cerebrovascular reactivity.

Imaging cerebral small vessel disease at 7 Tesla MRI

The findings of this thesis show that the use of 7 Tesla MRI reveals several potential early biomarkers for cerebral small vessel disease. The 7 Tesla MRI is still an experimental system, with some challenges that should be taken into account when using it for clinical research, such as field inhomogeneities, contra-indications for scanning and quickly improving scan-techniques. Patients tolerate 7 Tesla MRI very well and most patients even experience no large differences between 1.5T and 7T. Overall it can be stated that the use of 7 Tesla MRI results in many benefits for new or improved scans and appears to be very suitable to use for innovative clinical research in general. The use of 7 Tesla MRI can be important for better understanding and early detection of cerebral small vessel disease.

CHAPTER 09

Summary
Nederlandse samenvatting

Chapter 09 Nederlandse samenvatting

Samenvatting

De Engelse term ‘cerebral small vessel disease’, wordt vaak gebruikt om te verwijzen naar lacunaire infarcten en witte stof afwijkingen die zichtbaar zijn op MRI. Dit zijn ischemische lesies waarvan gedacht wordt dat ze veroorzaakt worden door veranderingen in de kleine vaten in de hersenen. Sinds kort worden ook microbloedingen steeds meer gezien als een manifestatie van cerebral small vessel disease. Lacunaire infarcten, witte stof afwijkingen en microbloedingen worden vaak gevonden op MRI scans van ouderen en ze zijn geassocieerd met een verhoogd risico op beroerte, cognitieve achteruitgang en overlijden. De kleine, perforerende vaten in de hersenen zijn echter lastig te visualiseren in vivo. Daarom worden lacunaire infarcten, witte stof afwijkingen en microbloedingen gebruikt als marker van cerebral small vessel disease, en is cerebral small vessel disease een synoniem geworden van deze lesies. De introductie van 7 Tesla MRI voor klinisch wetenschappelijk onderzoek biedt nieuwe kansen om de kleine, perforerende vaten in de hersenen te visualiseren en eerdere stadia van cerebral small vessel disease te identificeren. Het voornaamste doel van dit proefschrift was om ‘imaging biomarkers’ van vroege stadia van cerebral small vessel disease te onderzoeken met behulp van 7 Tesla MRI.

Cerebral small vessel disease en prognose in patiënten met atherosclerose

Lacunaire infarcten en witte stof afwijkingen verhogen de kans op beroertes, cognitieve achteruitgang en dementie in de algemene bevolking. Patiënten met atherosclerose hebben een verhoogd risico op vasculaire events. Het is niet bekend of de aanwezigheid van lacunaire infarcten of witte stof afwijkingen een additioneel risico op overlijden of vasculaire events geeft bovenop de pre-existente vasculaire ziekte. De klinische relevantie van lacunaire infarcten en witte stof afwijkingen in patiënten met atherosclerose is belangrijk, aangezien atherosclerose nog steeds een groeiend probleem is in de wereld, en witte stof afwijkingen en stille infarcten vaak voorkomen bij patiënten met atherosclerose. We vonden dat de aanwezigheid van een of meerdere lacunaire infarcten op MRI, symptomatisch of asymptomatisch, het risico op vasculaire en non-vasculaire dood verhoogt, onafhankelijk van leeftijd, geslacht, vasculaire risicofactoren, niet-lacunaire infarcten en witte stof afwijkingen (*hoofdstuk 2*). Witte stof afwijkingen verhogen het risico op vasculaire dood en het risico op een ischemisch herseninfact, onafhankelijk van dezelfde factoren en onafhankelijk van de aanwezigheid van lacunaire infarcten. Deze bevindingen illustreren het belang van lacunaire infarcten en witte stof afwijkingen voor de prognose van patiënten met atherosclerose.

Cerebral small vessel disease en imaging biomarkers op 7 Tesla MRI

Aangezien verondersteld wordt dat cerebral small vessel disease wordt veroorzaakt door veranderingen in kleine, perforerende arteriën in de hersenen, zijn deze perforerende arteriën een logische eerste stap in het onderzoek naar imaging biomarkers van cerebral small vessel disease. Eerdere studies hebben laten zien dat perforerende arteriën van de arteria cerebri anterior en arteria cerebri media gevisualiseerd kunnen worden met 7 Tesla MRI. In *hoofdstuk 3* laten we zien dat het mogelijk is om met time-of-flight angiografie op 7T de perforerende arteriën van de arteria communicans posterior en van het P1-segment van de arteria cerebri posterior te visualiseren, zonder het gebruik van contrast middelen. De resultaten laten zien dat de aanwezigheid van perforerende arteriën van de arteria communicans posterior geassocieerd is met een grotere diameter van de arteria communicans posterior. Het op een non-invasieve manier in beeld brengen van perforerende arteriën kan in toekomstige studies gebruikt worden om de kennis over infarcten in de diepe hersenstructuren die door deze arteriën gevoed worden te vergroten.

Gedacht wordt dat endotheel dysfunctie een rol speelt in de pathofysiologie van cerebral small vessel disease. Microbloedingen worden veroorzaakt door lekkage van rode bloed cellen uit de kleine vaten in de hersenen. De aanwezigheid van hele kleine microbloedingen zou een van de eerste manifestaties van cerebral small vessel disease kunnen zijn. Microbloedingen zijn paramagnetisch en induceren daardoor een susceptibiliteits-effect op de MRI scan. Echo tijd en veldsterkte zijn twee factoren die het susceptibiliteits-effect beïnvloeden en daarmee ook de visualisatie van microbloedingen beïnvloeden. In *hoofdstuk 4* onderzoeken we het gebruik van een dual echo T2*-gewogen sequentie op 7T voor de visualisatie van microbloedingen. Op 7T is het mogelijk om met een korte echotijd al microbloedingen te visualiseren. De korte echo tijd draagt bij aan het onderscheiden van microbloedingen van andere structuren met een hoge susceptibiliteit. Met het gebruik van een lange echo tijd kan een groter aantal microbloedingen gedetecteerd worden. De dual echo sequentie combineert de voordelen van een korte en een lange echotijd in een scan. In de huidige studies naar microbleeds wordt over het algemeen een 3D T2*-gewogen sequentie op 1.5T gebruikt voor de detectie van microbleeds. Vergeleken met een hoge resolutie 3D T2*-gewogen sequentie op 1.5T, wordt met de dual echo T2*-gewogen sequentie op 7T in meer patiënten microbloedingen gevonden en wordt er ook een groter aantal microbloedingen gevonden. Daarnaast is de betrouwbaarheid van de detectie van microbloedingen hoger op 7T (*hoofdstuk 5*).

IJzer is belangrijk voor metabole processen in de hersenen en met het ouder worden treedt progressieve ijzerdepositie in de hersenen op. Buiten de hersenen wordt gedacht dat ijzer een rol speelt in de pathogenese van atherosclerose. Er wordt aangenomen dat ijzer een belangrijke determinant is voor het ontwikkelen van atherosclerose. Aangezien lacunaire infarcten, witte stof afwijkingen en microbloedingen geassocieerd zijn met een verhoogde permeabiliteit van de perforerende vaten in de hersenen, is het mogelijk dat deze verhoogde permeabiliteit tevens een toegenomen ijzer depositie in de basale kernen tot gevolg heeft. Aangezien het gebruik van ultra-hoge veldsterktes, zoals 7 Tesla MRI, leidt tot een enorme verhoging van susceptibiliteits-effect, sensitiviteit en resolutie, kan dit goed bruikbaar zijn om subtiele verschillen in ijzerconcentratie te detecteren. Met 7 Tesla MRI hebben we de determinanten van ijzer depositie in de hersenen en ijzer depositie als vroege imaging marker van cerebral small vessel disease onderzocht (*hoofdstuk 6*). T2*-waarden van het putamen, de globus pallidus en de nucleus caudatus werden gebruikt als een maat voor ijzer depositie in de basale kernen. Op de fase-beelden waren fase-verschillen zichtbaar die karakteristiek zijn voor ijzer in de basale kernen, wat erop wijst dat de verschillen in T2* die in deze studie gevonden zijn, veroorzaakt worden door ijzerdepositie. Hogere leeftijd en mannelijk geslacht waren geassocieerd met verhoogde ijzer depositie in een of meer van de basale kernen. Lacunaire infarcten, maar niet witte stof afwijkingen of microbloedingen, waren eveneens geassocieerd met significant meer ijzer depositie.

De toegenomen permeabiliteit van perforerende arteriën kan ertoe leiden dat er serum componenten in de vaatwand komen, wat verdikking, inflammatie en disorganisatie van de vaatwand veroorzaakt. Deze veranderingen in de vaatwand kunnen zorgen voor een veranderde vasculaire reactiviteit in patiënten met cerebral small vessel disease. Cerebrovasculaire reactiviteit kan gemeten worden met BOLD-fMRI (functionele MRI op basis van het zuurstof gehalte in het bloed). Met toenemende veldsterkte, nemen de sensitiviteit, specificiteit en het contrast van de BOLD-respons toe. In *hoofdstuk 7* hebben we de relatie tussen lacunaire infarcten, witte stof afwijkingen, microbloedingen en cerebrovasculaire reactiviteit onderzocht met 7 Tesla MRI. Een verminderde vasculaire reactiviteit werd gevonden in patiënten met microbloedingen, onafhankelijk van leeftijd, geslacht, systolische en diastolische bloeddruk, en niet-lacunaire infarcten. In patiënten met lacunaire infarcten of witte stof afwijkingen werd geen significante associatie met cerebrovasculaire reactiviteit gevonden. De bevinding dat de cerebrovasculaire reactiviteit verminderd is in patiënten met microbloedingen, ondersteunt de hypothese dat veranderingen in de vaatwand bij patiënten met microbloedingen leidt tot stijfheid van de vaten en afgenomen vasculaire reactiviteit.

Cerebral small vessel disease op 7 Tesla MRI

De bevindingen van dit proefschrift laten zien dat met het gebruik van 7 Tesla MRI verschillende mogelijke vroege biomarkers voor cerebral small vessel disease in beeld gebracht kunnen worden. De 7 Tesla MRI is nog een experimenteel systeem, dat uitdagingen met zich meebrengt voor klinisch wetenschappelijk onderzoek, zoals inhomogeniteiten in het veld, contra-indicaties voor scannen en snel verbeterende scan-technieken. Patiënten verdragen 7 Tesla MRI erg goed en de meeste patiënten ervaren zelfs weinig verschil tussen de 1.5T en 7T. In het algemeen kan gezegd worden dat 7 Tesla MRI resulteert in vele voordelen voor nieuwe of verbeterde scans en dat het erg bruikbaar is voor innovatief klinisch onderzoek. Gebruik van 7 Tesla MRI kan een belangrijke bijdrage leveren aan beter begrip en vroege detectie van cerebral small vessel disease.

CHAPTER 10

Dankwoord
Curriculum Vitae
Appendix

Chapter 10 Dankwoord

Dankwoord

Promoveren doe je niet alleen. Naast de deskundige begeleiding van mijn promotoren en co-promotoren heb ik veel hulp en steun gehad van collega's, familie en vrienden. Daarom wil ik van deze gelegenheid gebruik maken om mijn waardering uit te spreken voor de mensen die een bijzondere bijdrage hebben geleverd aan mijn promotie.

Professor P.R. Luijten, beste Peter, ik heb veel bewondering voor de manier waarop je de snel groeiende 7 Tesla groep in slechts drie dagen in de week weet te managen. Ondanks je drukke agenda staat je deur altijd open om van alles te bespreken, dat vond ik erg fijn. Bedankt voor je input en steun tijdens mijn promotie!

Professor W.P.Th.M. Mali, beste professor, we hebben niet heel vaak contact gehad tijdens mijn promotie, maar als we overleg hadden was dat voor mij altijd heel motiverend. Uw ideeën en praktische tips zijn erg waardevol geweest voor mijn onderzoek.

Dr. M.I. Geerlings, beste Mirjam, als niet-Julius promovendus was ons contact misschien wat anders dan met je andere promovendi, maar daar hebben we in de loop van de tijd een goed evenwicht in weten te vinden. Ik heb veel bewondering voor hoe veel tijd en energie je elke keer weer in het onderzoek en in iedere paper stopt, er is geen detail wat je ontgaat. Je steun is gedurende mijn hele promotie, maar met name tijdens de afronding van mijn promotie, erg belangrijk voor me geweest.

Dr. J. Hendrikse, beste Jeroen, ongelofelijk hoeveel ideeën voor nieuwe onderzoeken jij altijd hebt! Niemand heeft me tijdens mijn promotie meer weten te motiveren dan jij. Je hebt de bijzondere eigenschap om meer nadruk te leggen op de dingen die goed gaan dan op de dingen die anders moeten, wat ik als erg prettig heb ervaren. Bedankt voor je positiviteit!

Professor Y. van der Graaf, beste Yolanda, bedankt voor de begeleiding in de periode dat Mirjam er niet was. De SMART-studie is een grote, maar toch overzichtelijke studie, waardoor het prettig is om met SMART-patiënten te werken. Ik heb bewondering voor de manier waarop je dat allemaal coördineert.

Dr. G.J. Biessels, beste Geert-Jan, die piepkleine, moeilijk te scoren microbleeds zijn intrigerend, zeker nu we zo goed kunnen zien op de 7 Tesla MRI. Het was leuk om daar met zijn allen over na te denken en de verschillende studies te combineren. Bedankt voor je bijdrage aan het onderzoek naar de microbleeds.

De beoordelingscommissie bestaande uit professor Y. van der Graaf, professor M.A. Viergever, professor L.P.E. Regli, professor L. Kappelle en dr. G.J. Biessels, bedankt voor het lezen en het beoordelen van het manuscript.

Beste co-auteurs, jullie bijdrage heeft het onderzoek en de artikelen vele stappen vooruit gebracht. Bedankt voor alle goede ideeën en feed-back!

Dr. J.J.M. Zwanenburg, beste Jaco, er is niemand die me met zoveel uiteenlopende dingen heeft geholpen als jij. Van het aansluiten van mijn computer op mijn eerste dag in Utrecht tot het scannen van patiënten en uitleggen van moeilijke MRI-sequenties, op alle fronten heb je veel voor mijn onderzoek betekend. Je bent iemand die altijd voor iedereen klaar staat dat maakt je tot een fijn persoon en een prettige collega. Bedankt voor alles!

Beste Fredy, zonder jou was het niet gelukt om zoveel mooie scans te maken op de 7 Tesla MRI. Het is ongelofelijk hoeveel jij van MRI weet en met die kennis veel onderzoeken op de 7T draaiende houdt. Het grootste deel wat ik nu van MRI weet heb ik van jou geleerd. Bedankt voor al je uitleg en hulp!

Professor T. Takahara, dear Taro, it was nice to have you as my roommate. You've learned me a lot about radiology and MRI, but also about Japan, Japanese people and the great taste of sushi. Thank you for your interest in my research and the scoring of the numerous microbleeds. I really enjoyed the time we spend together en hope to see you again in the future!

Dr. J.M. Hoogduin, beste Hans, je hebt me ingewijd in de geheimen van fMRI, een van de interessante mogelijkheden van MRI. Bedankt voor je hulp bij het scannen en het uitwerken van die eindeloze hoeveelheid data die de fMRI scans opleveren.

Beste Daniel, als echte JIST-expert heb je een mooie tool gemaakt voor de kwantificatie van T2* van de basale kernen en alle scans daarmee geanalyseerd, wat mooie resultaten heeft opgeleverd. Naast de nuttige dingen, ook bedankt voor de gezellige gesprekken over koffie, eten en de andere goede kanten van het leven!

Beste Sylvia, jij bent een belangrijke spil binnen de 7 Tesla groep. Ik vind het knap hoe je het voor elkaar krijgt om alle organisatorische zaken zo goed te regelen. Ook voor mijn onderzoek heeft jouw organisatorische talent veel goeds gedaan, bedankt!

Alle andere 7T collega's: Vincent, Jeroen, Catalina, Wouter, Wiebe, Mies, Bertine, Dennis, Hugo, Natalia, Bart, Mariska en Irene. De groep is ondertussen zo groot geworden dat ik niet iedereen persoonlijk kan bedanken en daarom wil ik hierbij tegen iedereen zeggen: bedankt voor jullie bijdrage, steun en vooral voor de gezellige tijd! De 7T groep is een goed geoliede machine en het was fijn om hier drie jaar deel van uit te mogen maken. Zelfs de fysische grapjes ben ik gaan waarderen en begin ik nu al een beetje te missen!

Beste Theo Witkamp, het scoren van de soms ontelbare microbleeds op 1.5T en 7T is een hele klus, waarvan ik heel blij ben dat u dat heeft willen doen. Bedankt voor uw inzet en de prettige samenwerking!

Dr. ir. K.L. Vincken, beste Koen, het is fantastisch om te zien wat er allemaal geautomatiseerd kan worden als je goed met computers om kan gaan. De segmentaties zijn een belangrijk onderdeel van de SMART-studie en leveren veel informatie op. Segmentatie van 7T data is nog wel een uitdaging, maar ik twijfel er niet aan dat ook dat binnenkort zal lukken.

Beste Raoul, we hebben een gezamenlijke interesse in small vessel disease en jouw ideeën en gezichtspunten vanuit de neurologie hebben een belangrijke bijdrage geleverd aan mijn onderzoek. Bedankt voor de samenwerking! Ik ben erg benieuwd naar de resultaten van jouw onderzoek!

Beste SMART-medewerkers, Harry, Loes, Lies, Hetty, Ursula en Desiré, zonder jullie zou de SMART-studie niet kunnen bestaan. Het is knap hoe jullie deze omvangrijke studie met allerlei sub-studies kunnen overzien en in goede banen leiden. Loes, jou wil ik in het bijzonder bedanken voor al het organisatorische werk rondom het scannen van de SMART-patiënten op de 7 Tesla MRI. Het is fijn om te weten dat als jij iets regelt, het zeker goed gebeurt!

Beste Greet, Niels, Gerrit, Saskia en Laura, bedankt voor al jullie hulp bij het maken van de MRI's. De 7 Tesla MRI doet niet altijd wat je verwacht, maar weten jullie altijd weer goed mee om te gaan en het tot een goed einde te brengen. Bedankt voor jullie inzet en creativiteit!

Beste collega-onderzoekers van de radiologie, bedankt voor de gezelligheid! De vele traktaties, gezellig praatjes en etentjes maken het onderzoek doen erg leuk!

Beste radiologen en collega-assistenten van het VUmc, het valt niet altijd mee om het begin van de opleiding te combineren met het afronden van een proefschrift. Bedankt voor jullie begrip en interesse!

Beste André, bedankt voor het ontwerp en de lay-out van mijn proefschrift. Het was prettig om met je samen te werken en ik ben erg blij met het resultaat!

Lieve Anne en Anja, fijn dat jullie mijn paranimfen willen zijn! Met jullie beiden heb ik veel hoogtepunten, maar ook zo nu en dan de frustraties van het promoveren kunnen delen. Lieve Anne, onze promoties hebben voor een groot deel parallel gelopen. Het werken aan de SMART-studie en de master Epidemiology, het was super om dit samen met jou te kunnen doen. Met als hoogtepunt Rome, met lekkere pizza's, goede wijn en vooral veel gezelligheid! Lieve Anja, erg gezellig dat jij deel uit maakt van de 7 Tesla groep en mijn roommate bent op de ISMRM-reizen! Het was fijn om met jou de 7T dingen te kunnen bespreken, je hebt altijd een interessante kijk op dingen. Stockholm was super, Montreal wordt vast minstens zo goed!

Lieve Shelley en Marloes, goede vriendinnen zijn erg belangrijk in drukke periodes. Ik haal veel energie uit de momenten dat we elkaar zien, tijdens het sporten of een weekendje weg. Fijn dat jullie zo dichtbij wonen, dat we elkaar vaak kunnen zien en belangrijke momenten kunnen delen!

Lieve Mireille en Sammy, ondanks dat we elkaar niet zo vaak zien blijft ons contact heel bijzonder. Het is leuk om te merken dat we over veel dingen hetzelfde denken. Ik ben trots op wat jullie tot nu toe bereikt hebben. Als we allemaal weer in een wat rustigere periode zitten moeten we snel weer afspreken!

Lieve Hans, Bep, Barbara en Wouter, vanaf het begin heb ik me welkom gevoeld bij jullie. Bedankt voor alle gezelligheid!

Lieve Eveline en Casper, Linda en Bas, wat ben ik blij dat jullie er zijn! Als we samen zijn is het altijd super gezellig, het is leuk dat we zoveel gezamenlijke interesses hebben. Bedankt voor jullie steun en begrip de afgelopen tijd, bedankt dat ik altijd op jullie kan rekenen!

Lieve pap en mam, zonder alles wat jullie me geleerd hebben was me dit niet gelukt. Het geeft me een goed gevoel om te weten dat jullie altijd achter me staan en er altijd voor me zijn. Bedankt voor de onvoorwaardelijke steun en liefde. Ik kan me geen fijnere ouders voorstellen dan jullie!

Lieve Jasper, zonder dat je daarin een keuze had heb je meegedeeld in de hoogte- en dieptepunten van mijn promotie. Ik heb veel bewondering voor je geduld, je verfrissende kijk op gebeurtenissen en de manier waarop je me altijd weer weet op te vrolijken. Jij maakt mijn leven geweldig en ik kijk nu al uit naar alles wat we in de toekomst samen gaan beleven!

CHAPTER 10

Dankwoord
Curriculum Vitae
Appendix

Chapter 10 Curriculum Vitae

Curriculum Vitae

Mandy Martine Ariane Conijn was born on June 16th, 1983, in Lisse, the Netherlands. After graduating from secondary school at the Fioretti College in Lisse in 2001, she started her medical training at the University of Leiden. During her study her interest in radiology was raised and she performed an elective internship at the department of radiology at the Leiden University Medical Center (LUMC). Her research internship at the department of neurology at the LUMC made her enthusiastic about scientific research. At the end of 2007 she obtained her medical degree.

In January 2008 she got the opportunity to start the first clinical research project on the clinical 7 Tesla MRI system at the University Medical Center Utrecht. This resulted in her PhD thesis on the imaging of cerebral small vessel disease at 7 Tesla MRI under supervision of prof. dr. P.R. Luijten, prof. dr. W.P.Th.M. Mali, dr. M.I. Geerlings and dr. J. Hendrikse. During her PhD period she obtained a Master degree in Clinical Epidemiology at the University of Utrecht. In November 2010 she started her radiology residency at the VU Medical Center in Amsterdam (prof. dr. C. van Kuijk).

CHAPTER 10

Dankwoord
Curriculum Vitae
Appendix

Chapter 10 Appendix

List of used abbreviations

95% CI	95% confidence interval
AChA	Anterior choroidal artery
ANCOVA	Analysis of covariance
B	Regression coefficient
BBB	Blood-brain barrier
BMI	Body mass index
BOLD-fMRI	Blood oxygenation level-dependent functional MRI
CSF	Cerebrospinal fluid
CVR	Cerebrovascular reactivity
EPI	Echo Planar Imaging
FOV	Field of view
FLAIR	Fluid-attenuating inversion recovery
FWHM	Full width at half maximum/minimum (Chapter 3/Chapter 4)
GRE	Gradient-recalled echo
HR	Hazard ratio
iaDSA	intra-arterial digital subtraction angiography
ICC	Intraclass correlation coefficient
ICV	Intracranial volume
IR	Inversion recovery
JIST	Java Image Science Toolkit
MARS	Microbleed Anatomical Rating Scale
minIP	Minimum intensity projection
MIP	Maximum intensity projection
MRI	Magnetic Resonance Imaging
P1	P1-segment of the posterior cerebral artery
PCoA	Posterior communicating artery
PRESTO	Principles of echo shifting with a train of observations
ROI	Region of interest
SD	Standard deviation
SENSE	Sensitivity encoding
SMART study	Second Manifestations of ARTerial disease study
SMART-MR	Second Manifestations of ARTerial disease-Magnetic Resonance
SNR	Signal to noise ratio
SWI	Susceptibility weighted imaging
TE	Echo time
TE1	First echo time
TE2	Second echo time
TI	Inversion time
TIA	Transient ischemic attack
TOF	Time-of-flight
TONE	Tilt-optimised non-saturated excitation
TR	Repetition time
WML	White matter lesions